Nano Today (2014) 9, 271—304

Available online at www.sciencedirect.com

ScienceDirect

journal homepage: www.elsevier.com/locate/nanotoday

Metal-assisted chemical etching of silicon and nanotechnology applications

Hee Han[a], Zhipeng Huang[b,*], Woo Lee[a,c,**]

[a] Korea Research Institute of Standards and Science (KRISS), Yuseong, 305-340 Daejeon, Republic of Korea
[b] China-Australia Joint Research Center for Functional Molecular Materials, Scientific Research Academy, Jiangsu University, Zhenjiang 212013, PR China
[c] Department of Nano Science, University of Science and Technology (UST), Yuseong, 305-333 Daejeon, Republic of Korea

Received 11 November 2013; received in revised form 31 March 2014; accepted 21 April 2014
Available online 24 May 2014

KEYWORDS
Metal-assisted chemical etching;
Silicon nanowires;
Nanotechnology

Abstract Silicon nanostructures exhibit promising application potentials in many fields in comparison with their bulk counterpart or other semiconductor nanostructures. Therefore, the exploiting of controllable fabrication methods of silicon nanostructures, and the exploring of further applications of silicon nanostructures gain extensive attentions. In this review, recent advances in metal-assisted chemical etching of silicon, a low-cost and versatile method enabling fine control over morphology feature of silicon nanostructures, are summarized. The overview concerning the applications of silicon nanostructures in the field of energy conversion and storage, and sensors are also presented.

Introduction

Silicon (Si) has been the most widely used semiconductor for decades, playing important role in the field of electronics, energy conversion, energy storage, and so on. Because of morphological and energetic feature, Si nanostructures exhibit superior performance in many applications in comparison with their bulk counterpart. As a result, researchers are stimulated to exploit methods for the controllable fabrication of Si nanostructures, and explore the application of Si nanostructures.

Various methods have been developed to fabricate Si nanostructures in top-down or bottom-up scheme. Among them, metal-assisted chemical etching (MACE) [1—6] is particularly intriguing and promising, because of its simplicity, good cost-efficiency, and versatility. Various Si nanostructures, for example, Si nanowires (SiNWs), porous SiNWs, Si nanopores, have been successfully fabricated by this facile method, with their morphological features well controlled. A mass of articles have been published in this

* Corresponding author.
** Corresponding author at: Korea Research Institute of Standards and Science (KRISS), Yuseong, 305-340 Daejeon, Republic of Korea. Tel.: +82 42 868 5397; fax: +82 42 868 5032.
E-mail addresses: woolee@kriss.re.kr (W. Lee), zphuang@ujs.edu.cn (Z. Huang).

http://dx.doi.org/10.1016/j.nantod.2014.04.013

field, including our review article published in 2011 [7]. In our previous review article, possible mechanism, influence of various factors on etching, and the fabrications of ordered Si structures by MACE were summarized. At the end of article, we listed some open questions that cannot be explained or have not yet been investigated in details at that time. Copious amounts of articles have been published in recent three years, introducing new phenomena in MACE. This is beneficial for further understanding of MACE process, and broadening the application versatility of Si nanostructures fabricated by MACE. Tremendous effort has been devoted to realization of various Si nanostructure-based devices such as energy storage, harvesting, optoelectronics, and sensors. Recent reports on the potential applications of Si nanostructures have exhibited promising view. For example, solar energy conversion efficiency is found to be increased when SiNWs with high aspect ratio are employed. Compared to bulk silicon, SiNW is known to possess significantly reduced thermal conductivity, and thus has been regarded as an excellent thermoelectric material. SiNWs are also promising as an anode material of Li-ion battery due to its excellent accommodation ability of large volume expansion during Li-ion insertion process. High surface to volume ratio and unique charge transport property of SiNWs can offer high sensitivity, selectivity and stability when used as sensor. Number of reports on novel strategies for improving operating performances of various devices based on such SiNWs is still increasing. In particular, SiNWs synthesized by MACE provide distinct advantage in terms of fabrication of advanced devices at a low cost. Therefore, deeper understanding on the MACE of Si may help advanced realization of Si nanostructure-based high performance devices. Here we will summarize the recent advances in MACE of Si, emphasizing new findings that have not yet been introduced in previous review article. First, we will discuss new findings concerning etching process, then new morphologies developed by MACE, new MACE techniques for controllable fabrication of Si structures, and finally the applications of Si nanostructures in the field of energy conversion, storage, and sensors.

Brief model of MACE

In a well accepted model describing MACE process, the oxidant is preferred to be reduced at the surface of metal catalyst, and holes (h^+) are injected from metal catalyst to Si or electrons (e^-) are transferred from Si to metal catalyst. Si underneath metal catalyst has the maximum hole concentration, therefore the oxidation and dissolution of Si occur preferentially underneath metal catalyst. The detailed morphology of etched structure correlates with various processes during MACE, for example, the mass transfer, the movement of metal-catalyst, hydrogen production, heat production, the dissolution and re-deposition of metal-catalyst, the diffusion of reagent or by products in etchant, and the diffusion of excess holes (h^+) in silicon.

Mass transfer during MACE

Sufficient experimental evidences have been reported to support a solid mass transfer model [8,9]. In the scenario, the oxidation of Si surface proceeds at the interface between metal and Si substrate; through HF can diffuse through the channels between Si and metal catalyst to bulk Si to facilitate the oxidative dissolution of Si, and reactants and byproducts diffuse as well through the channels (Fig. 1a). Two sets of etching experiments were carried out for comparison. Metal (Ag) stripes, including those with different lateral sizes while the same thickness and those with identical lateral size but different thicknesses were deposited onto Si substrates, and subsequently the samples were etched in an aqueous etchant comprised of HF and H_2O_2. The experiments showed that the etching rate decreases with the lateral size of Ag stripes, indicating the correlation between the etching rates of Si and the lateral sizes of Ag stripes. In addition, Ag stripes with different

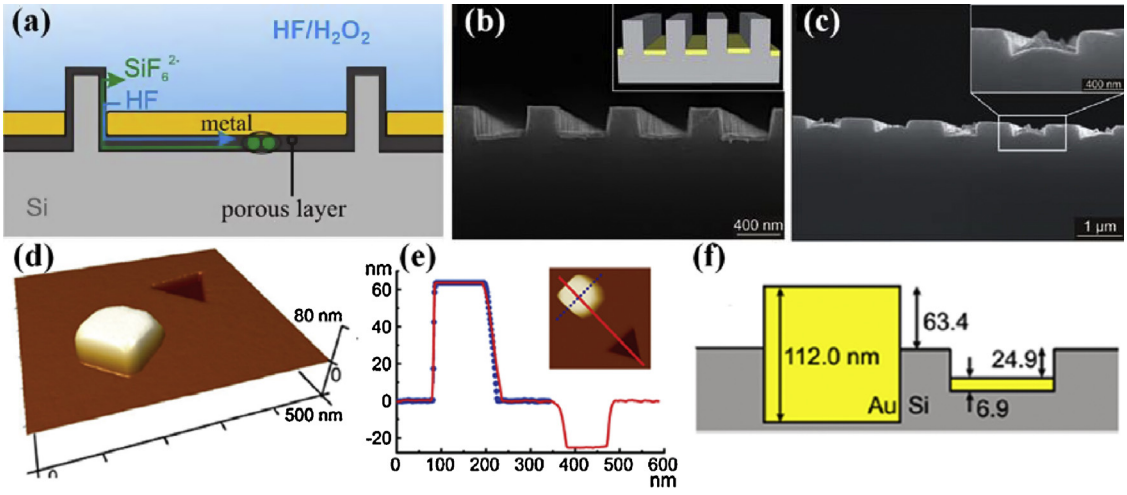

Fig. 1 (a) Model of mass transfer during MACE. SEM images of etched Si loaded with stripes of 40 nm thickness and (b) 390 nm width or (c) 710 nm width [8]. Copyright 2012, The American Chemical Society. (d) AFM image and (e) line profile of etched Si loaded with 112 nm thick Au nanocube and 6.9 nm thick nanoprism. (f) Scheme showing the etching depth of Au nanocube and nanoprism [9]. Copyright 2013, The American Chemical Society.

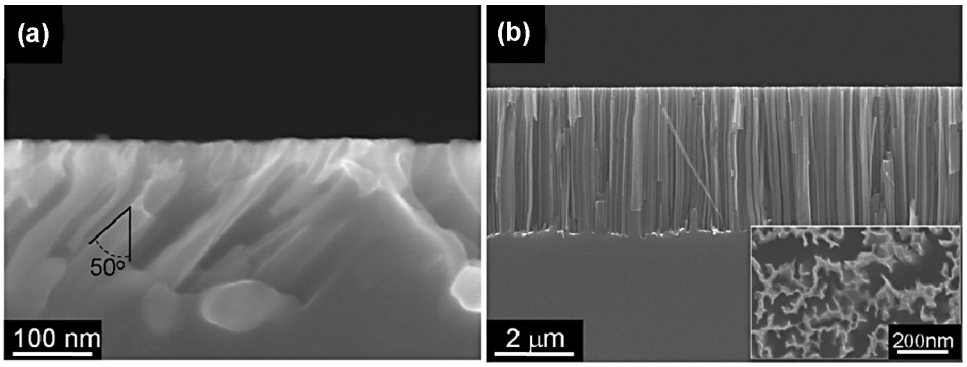

Fig. 2 (1 1 1) Si wafer etching along (a) ⟨1 0 0⟩ directions, and (b) [1 1 1] direction. Reproduced with permission from Ref. [14]. Copyright 2010, The American Chemical Society.

thicknesses but the same width result in the same rate of etching [8]. In other experiments, a 112-nm-thick Au nanocube exhibited a larger etching rate, compared to 6.9-nm-thick Au nanoprism (Fig. 1d and e) [9]. These results exclude the model that reagents might diffuse through metal catalyst, because the later model predicts that etching rate will decrease with the thickness of catalyst and etching rate is independent to the lateral size of metal catalyst. In more details, Geyer et al. proposed that reagents diffuse through porous layer in Si just underneath the metal catalyst [8]. On the other hand, based on no apparent formation of porous layer beneath the etched trenches, Liu et al. claimed that the porous layer is not necessary and the reagent/products can diffuse along Si/metal interface [9]. In practice, only shallow trenches are obtained in the etching of silicon with a large continuous metal catalyst film, because above mentioned model of mass transfer suggests that the diffusion of reactants to the central part of continuous catalyst metal film with a large lateral dimension is difficult due to the long diffusion distance. In contrast, when gold stripes with nanoporous morphology is used in MACE, a large number of pores in the stripes enables the fast mass transfer through these pores. Therefore, the reactants have sufficient chance to reach the edge and center part of the stripes, resulting in the formation of deep vertical etched trench with uniform depth [10].

Etching directions

So far, the reported etching directions include ⟨1 0 0⟩/(1 0 0) [1], where the former index indicates etching direction and the later index indicates the orientation of Si wafer, ⟨1 1 0⟩/(1 0 0) [11], ⟨1 1 1⟩/(1 0 0) [11,12], ⟨1 1 2⟩/(1 0 0) [12], ⟨1 1 3⟩/(1 0 0) [12], ⟨1 0 0⟩/(1 1 0) [13], ⟨1 1 0⟩/(1 1 0) [13], ⟨1 0 0⟩/(1 1 1) [14], ⟨1 1 0⟩/(1 1 1) [15], ⟨1 1 1⟩/(1 1 1) [14,15], ⟨1 1 3⟩/(1 1 1) [16], ⟨2 1 0⟩/(1 1 1) [15], ⟨2 1 1⟩/(1 1 1) [15], ⟨3 1 0⟩/(1 1 1) [15], ⟨3 1 1⟩/(1 1 1) [15], ⟨3 2 0⟩/(1 1 1) [15], ⟨4 1 0⟩/(1 1 1) [15], ⟨5 2 1⟩/(1 1 1) [15], and so on. ⟨1 0 0⟩ directions are found to be the preferential etching direction of Si in MACE in some articles [17]. There are also lots of experiments, showing the non-⟨1 0 0⟩ etching in non-(1 0 0) wafer [13—16]. It is worth noting that even (1 0 0)-oriented Si wafer can be etched along non-⟨1 0 0⟩ directions [11,12]. The influence of experimental conditions on the etching direction has been explained in terms of the different back bond strengths of surface Si atoms or the number density of surface Si atoms required to be removed on different planes.

Various factors have been found to affect etching direction, or induce the variation of etching direction. The molarity ratio of HF to oxidant (e.g., H_2O_2 and $Fe(NO_3)_3$) affects the etching direction of Si wafers [11,14]. In aqueous etchant with a high [HF]/[oxidant] ratio Si(1 1 1) wafer is etched along ⟨1 0 0⟩ directions (Fig. 2a), and the etching proceeds along vertical [111] direction when the [HF]/[oxidant] ratio is sufficiently low (Fig. 2b) [14]. The back bond strength and the surface oxidation state of Si contribute commonly to the etching direction. When the relative concentration of oxidant is low, surface termination of Si wafer is Si—H, and would vary to Si—OH and further SiO_2 with increasing relative oxidant concentration. The presence of Si—OH or SiO_2 on the surface of Si at etching front weakens the effect of back bond strength, enabling non-⟨1 0 0⟩ directions etching.

The etching of Si(1 0 0) substrate exhibits a opposite relation between the etching direction and the [HF]/[H_2O_2] ratio [11], in comparison with that of Si(1 1 1) substrate. In MACE of Si(1 0 0) wafer, a low [HF]/[H_2O_2] ratio results in etching along ⟨1 0 0⟩ directions, because Si atoms to be removed are the least on (1 0 0) plane, while increasing [HF]/[H_2O_2] allows etching along other directions containing more surface Si atoms (e.g., ⟨1 1 0⟩ and ⟨1 1 1⟩) [11]. The addition of co-solvent (e.g., methanol, ethanol, 2-propanol, and acetonitrile) into the etchant during two-step MACE of p-type Si(1 0 0) wafer ($\rho = 10—30\,\Omega\,cm$) induces etching along the directions deviating from ⟨1 0 0⟩ [18]. Kim et al. demonstrated frabrication of extended arrays of tilted SiNWs on a 4-in. Si(1 0 0) wafer by using an etchant system comprised of HF:H_2O_2:H_2O:2-propanol (2:1:4:3) [18]. The authors attributed the observed etching behavior to the local variations of the relative molar concentration of HF to H_2O_2 at the etching front; In etchants containing co-solvent, H_2O_2 is assumed to be more severely shielded from reaction sites due to its higher surface tension, compared to HF. Consequently, a local high [HF]/[H_2O_2] ration can be established near the etching front, allowing etching along non-⟨1 0 0⟩ directions. This is in line with the earlier report by Kim et al. who explained the formation of zigzag SiNWs during MACE of Si(1 0 0) wafer in terms of the relation between the local [HF]/[H_2O_2] concentration at the etching front and the etching direction [12].

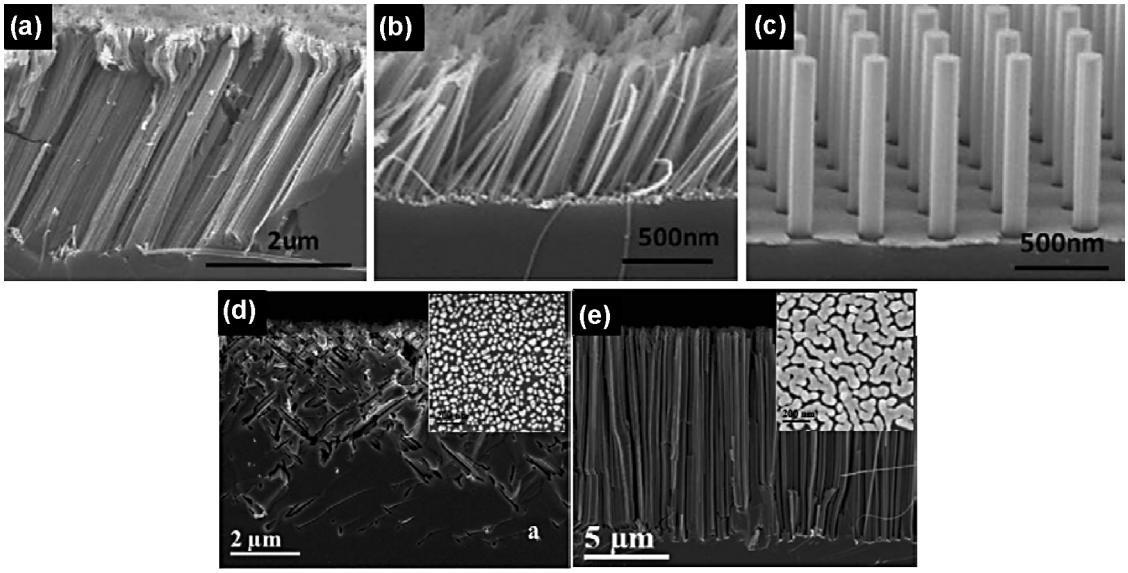

Fig. 3 Si structures resulting from MACE of (1 1 0) Si wafer using (a) isolated Au particles, Au meshes film with (b) small hole and (c) large spacing as catalyst [19]. Copyright 2010, Wiley-VCH Verlag GmbH & Co. KGaA, Weinheim. Si structures resulting from MACE of Si(1 1 1) wafer with (d) 5 s deposited Ag, and (e) 120 s deposited Ag. The insets of (d) and (e) show the morphology of deposited Ag [20]. Copyright 2012, The Electrochemical Society.

The etched structure in MACE can be viewed as the movement track of catalyst, and therefore the etching direction of Si is also modulated by the movement direction of catalyst. Isolated particles have 6 degrees of freedom (DoF) in MACE, whereas the DoF of catalyst might be constraint if the lateral dimension of metal catalyst is sufficiently large, enabling etching proceeds along the non-preferential directions defined by the crystal structure of Si (e.g., ⟨1 0 0⟩ directions). One example is the etching of Si(1 1 0) loaded with isolated Ag particles or Ag mesh film. Si(1 1 0) wafer loaded with isolated Ag particles was etched along ⟨1 0 0⟩ directions, while vertical [110] SiNWs can be obtained by using a Ag mesh film with sufficiently large lateral size as catalyst [13].

Holes spacing in metal meshes film was also found to influence the etching direction of non-(1 0 0) oriented Si substrates [19]. Au catalysts with three typical morphologies were deposited onto Si substrate, including isolated Au islands, Au mesh film with small holes spacing, and Au mesh film with relatively large holes spacing. Isolated particles and mesh with small hole spacing result in etching along preferential ⟨1 0 0⟩ directions (Fig. 3a and b), which can be ascribed to unconstrained movement of Au along both the vertical and lateral direction. If catalyst meshes possess relatively large hole spacing, etching is forced to proceed along the Si surface normal as a result of restricted horizontal movement of Au meshes film (Fig. 3c).

Electroless plating can construct inter-connected or isolated Ag particles, enabling convenient control over etching direction of Si [20]. For Si(1 0 0) surface with small clusters' size and low coverage, the etching proceeds both in vertical and horizontal ⟨1 0 0⟩ directions. With increasing the density and coverage (70%) of Ag nanoparticles, catalyst metals sink all together along the vertical [1 0 0] direction. In the case of Si(1 1 1) surface loaded with isolated Ag nanoparticles, metal particles sink in all equivalent ⟨1 0 0⟩ directions following an irregular path (Fig. 3d). When Ag nanoparticles begin to coalesce, domains of SiNWs, all aligned along ⟨1 0 0⟩ directions, are formed. When Si substrate is covered with inter-connected network of Ag particles and Ag particles' in-plane extension is larger than their average thickness, the etching direction is normal to the Si surface (Fig. 3e), since under these conditions their lateral movements are suppressed and etching direction is restricted, due to suppressed lateral movements. These observations may explain the conflicting experimental observations that Si(1 1 1) substrates exhibit different etching directions under similar etchant conditions [14,21]. Because the morphology of deposited Ag is determined not only by $AgNO_3$ and HF molarity, but also temperature, deposition time, illumination, the doping level of Si, the pre-treatment of Si wafer (e.g., with surface SiO_2 removed or not), and so on, the actual connectivity of Ag might be different in experiments of different research groups.

In the case of isolated metal catalyst, the catalyst can rotate during MACE besides the linear motion along certain directions, enabling the fabrication of novel three dimensional (3D) Si structures [22]. Ag catalysts with different morphologies exhibit different DoF of movement during MACE, and thus result in different morphologies of etched structures; Ag nanorods result in cycloid or strange channels (Fig. 4a), Ag nanodonuts result in spiral in the shaped template (Fig. 4b), and nanolines in strait, sliding, and cycloid-like etched features (Fig. 4c). The variation from nanolines to more complex shapes such as dog-bones, squares, and grids induces remarkable change in etching directions. Meanwhile, surface roughness of catalyst plays an important role in determining etching directions. For example, Ag nanorods deposited by focused ion beam (FIB) resulted in cycloid or strange channels, while Si loaded with Ag nanowires synthesized by polyol reduction [23] or Au nanorods fabricated by scanning probe block-copolymer

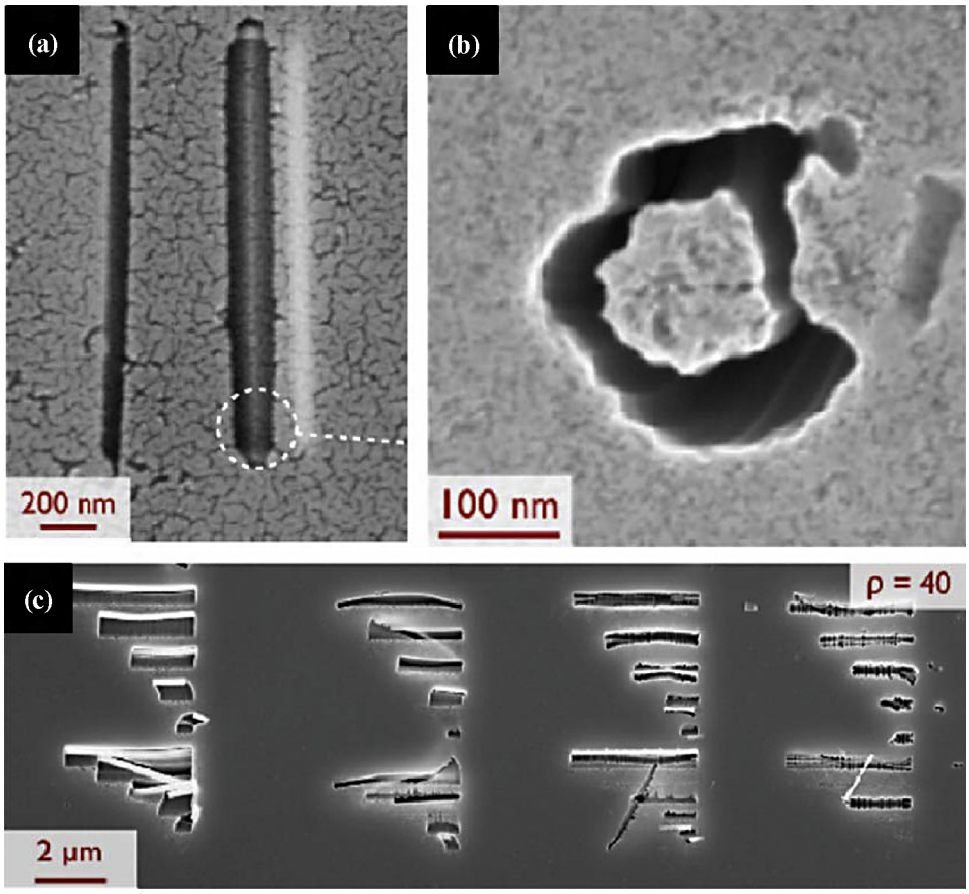

Fig. 4 Typical etched morphology of Si loaded with (a) Ag nanorod, (b) Ag nanodonut, and (c) Ag nanoline [22]. Copyright 2009, The American Chemical Society.

lithography [9] was etched into vertical straight pores. A systematic investigation on the rotation of catalyst in MACE was carried out using star-shape catalyst as prototype [24—26]. The arm shape, arm length, number of arms, center core diameter and catalyst thickness would influence the rotation of star-shape catalyst during MACE, resulting in spiraling structures in Si substrate.

Two factors might correlate with the shape-dependent movement direction of catalyst. Firstly, the area of catalyst in intimate contact with Si depends heavily on catalyst shape. Because Si in conformal contact with catalyst is holes (h^+) rich regions, and will be etched faster than other regions, the shape of the dissolved Si is dependent on the catalyst shape. On the other hand, electric field-induced electrophoresis across metal catalyst is believed to be responsible for catalyst movement [27]. As the shape of catalyst changes, the electric field, the net force and thus the movement of catalyst are considered to be changed.

Besides the composition of etchant solution and the morphology of metal catalyst, the etching direction of Si can be influenced by other factors. For example, it is stated that sufficiently high temperature is necessary to allow the etching of Si(1 1 1) substrate proceed along ⟨1 0 0⟩ directions [16], or induce the deviation of etching direction from ⟨1 1 1⟩ [28]. Hydrogen bubbles generated during MACE have been believed to stimulate the variation of etching direction [16]. The morphologies of Si etched with or without etchant stirring are different, being straight SiNWs under unstirred etchant conditions and zigzag SiNWs under stirred ones [15]. This difference was attributed to stirring-promoted H_2 evaporation, which drives the switches of etching direction among various crystallographic directions. If ferromagnetic Fe is embedded in Au catalyst, the movement of metal catalyst and etching direction can be guided by an external magnetic field, enabling facile control over the etching direction to any desired directions, regardless of the crystallographic orientations of the starting Si substrate [29].

Porosification

Although it was reported a decade ago that heavily doped p-type Si (0.01—0.03 Ω cm) loaded with Au particles can be etched into porous pillars [30], fabrication of porous Si and its formation mechanism gain increasing attentions since the report of Hochbaum et al. [31] So far, porous SiNWs have been fabricated from heavily doped [31—33] or lightly doped Si wafer [34,35], including p-type [31,33] and n-type [32], in one step etching ($HF/AgNO_3$ [32], $HF/AgNO_3/H_2O_2$ [34]) or two step etching (metal plating followed by etching in HF/H_2O_2) [31,33]. It is widely accepted that dopants serve as nucleation sites for pore formation during the etching of Si, and that the formation of porous SiNWs in heavily doped Si correlates with the high dopant concentration [31—33]. On

the other hand, several major mechanisms have also been proposed to explain the formation of porous SiNWs during MACE of heavily doped Si.

Hochbaum et al. stated that the etching of Si in MACE is likely to follow an electrochemical mechanism, similar to that of conventional electrochemical syntheses of porous Si [31]. The main difference between MACE and electrochemical previous porous Si syntheses is that the current flux inducing porosification in MACE is provided by continuous Ag^+ reduction from solution, while that in electrochemical porous Si syntheses is driven by an applied bias through back electrical contacts. Increasing the doping level of p-type Si results in a decrease of energy barrier at Si/electrolyte interface, because the redox potential of Ag^+/Ag^0 lies below the valence band of Si. Under the same cell potential, a lower barrier affords a larger charge flow, thus increases roughness or porosity of etched Si nanostructures [31]. In addition, because of the insulating character of porous Si, the transport of electronic holes (h^+) through porous layer is not possible. Instead, the transport of electronic holes (h^+) proceeds primarily by means of the Ag^+/Ag^0 redox pair circulating in electrolyte and diffusing through etched pores in Si [36].

In the mechanism proposed by Qu et al., the dissolution and re-deposition of Ag contribute to the formation of porous SiNWs [32,37]. In a typical etch process, a localized Ag^+ ion cloud be created in the close proximity of Ag particles because of the oxidation of Ag particles by H_2O_2. These Ag^+ ions can quickly react with Si near Ag/Si interface and thus be recovered into the original Ag particles. In this case, etching is localized around Ag particles and Ag particles are trapped in nanopits created by themselves, leading to continuous etching in vertical direction and the formation of vertical SiNWs. If H_2O_2 concentration is sufficiently high, Ag^+ ions cannot be 100% recovered into the original Ag nanoparticles, and some of them may shed into the solution. When the amount of out-diffusing Ag^+ ions reach a certain threshold, these Ag^+ ions may start to nucleate on the sidewall of previously formed Si structure near certain weak defective sites (e.g., around dopants), forming new silver particles for new etch pathway and resulting in the porosification of Si. In this way, the increase of H_2O_2 concentration increases the amount of out-diffusing Ag^+ ions, and the increase of doping concentration increases the amount of weak defective points in Si lattice. Both are important factors for the introduction of additional etching pathway besides vertical etching. This mechanism is in accordance with the experimental observation that porosity increases with H_2O_2 concentration during the etching of heavily doped n-type Si substrates [32].

To et al. took into consideration small band bending in heavily doped n-type Si, in comparison with lightly doped one, and random etching induced by small Ag nuclei deposited on Si [33]. In their scheme, electrons in conduction band of Si have to tunnel through space charge region near Si/electrolyte interface and relax to surface states (SS) aligned with E_{Ag^+}, and then resonantly migrate to E_{Ag^+}, resulting in the formation of Ag nuclei or Ag dendrites [33]. Dimension and sinking performance of Ag particles substantially control the morphology of as-etched structures, and Ag^+ ions diffusing to Ag particles have crucial impact on the morphological evolution of Ag particles. The heavy dopants in n-type Si would deteriorate Ag^+ ions diffusion, because adequate negatively charged surface states (SS^-) accumulating at Si/electrolyte interface remarkably consume Ag^+ ions, slowing Ag^+ ions diffusion from bulk etchant to the etching front. High concentration of SS^- is ascribed to abundant neutral surface states stemming from heavy doping, and abundant electrons tunneling through the space charge region near Si/electrolyte interface, which originate from small barrier height in space charge region. In this case, the limited Ag^+ ions diffusion supports only a portion of Ag nuclei growing up to large Ag particles to scratch bulk Si into SiNWs. The rest non-grown nuclei sink randomly in a short period of time, creating mesopores with randomly distributed short tracks. Random scratching is driven by local perturbation of non-grown nuclei. In the case of lightly doped Si, the SS^- is diminished because the deduction of doping level increases the barrier height and broadens the space charge region, which inhibits electron tunneling from conduction band to neutral surface states. In this case, a steep [Ag^+] gradient can be established to promote ions diffusion, facilitating Ag nuclei grow and sink to produce solid SiNWs without pores.

On the other hand, there are other mechanisms proposed to explain the porosification of Si. Based on the experimental observation that no metal particles are detected within the pores in SiNWs or at the bottom of porous layer in the case of etching heavily doped p-type Si loaded with Ag or Au particles in HF/H_2O_2 etchant, Chiappini et al. suggested that the porosification of Si is catalyzed by the metal ions in solution without formation of secondary Ag nanoparticles, [38]. It is worth noting, however, that there are different experimental observations. Mikhael et al. found that when the heavily doped Si loaded with Au was etched in HF/H_2O_2 etchant, Au can be detected on the side wall of porous Si, whereas in porous layer underneath SiNWs no Au can be detected [39]. Geyer et al. reported that in HF solution containing sufficient low Ag^+ molarity (e.g., 0.18 μM) Si can be etched into porous Si but no Ag particle can be found, while with [Ag^+] increased to 18 μM Ag clusters are formed simultaneously with the formation of porous Si [36].

Typical morphologies of heavily doped Si etched by MACE methods are porous SiNWs on solid Si layer, or porous SiNWs on porous Si layer. These different morphologies were ascribed to the two competing processes occurring simultaneously, i.e., the porosification of Si and the vertical etching induced by primary large metal catalyst [33,38]. If the porosification of Si is faster than the vertical catalyst etching, Si will evolve into porous SiNWs on porous layer; else porous Si on solid Si can be obtained. The rate of Si porosification will increase with the doping level of Si and the concentration of H_2O_2 [38].

Lightly doped Si can also be etched into porous SiNWs. By introducing H_2O_2 into $HF/AgNO_3$ aqueous etchant, lightly doped p-type Si (7—13 Ω cm) can be etched into porous SiNWs [34]. Scanning transmission electron microscopy (STEM) observation shows that more Ag particles can be formed on the side wall of pre-existing SiNWs upon increasing H_2O_2 concentration, suggesting that the porosification of SiNWs could be attributed to the dissolution of Ag particles by H_2O_2 at the etching front, the re-deposition of small Ag particles on the side wall of SiNWs, and the lateral etching of SiNWs catalyzed by these small Ag particles. On the other hand, lightly doped p-type Si (6.0—10.5 Ω cm) loaded with

Au mesh can evolve into arrays of SiNWs with solid core and porous shell [40,41]. Instead of adding H_2O_2, the introducing of ethylene glycol (EG) into HF/$AgNO_3$ aqueous etchant can also etch lightly doped Si into solid SiNWs, solid SiNWs with porous shell, and porous SiNWs, depending on the volume ratio of EG in etchant [35]. The porosification of SiNWs was also attributed to the deposition of tiny Ag nuclei on the sidewall of SiNWs, and the following lateral etching catalyzed by these tiny nuclei. Because the viscosity of etchant increases with the volume ratio of EG, the diffusivity of reactive ions (Ag^+, F^-) from bulk solution to the etching front is considerably decreased. Consequently the reactive ions are inefficient to etch Si near Ag/Si interface, and etching pores initiated from the primary Ag particles are passivated because of the lack of F^- for the dissolution of Si. Meanwhile, the sidewalls of SiNWs formed by MACE have many defects, which are energetically favorable for the nucleation of tiny Ag particles, and provide a shorter diffusion path for ion transport. Therefore, the formation of tiny Ag particles on the sidewall of SiNWs is preferred for the porosification of Si.

Etching of amorphous silicon

Douani et al. investigated the etching behavior of amorphous Si thin film (α-Si:H, and α-$Si_{1-x}C_x$:H) deposited by low-power plasma enhanced chemical vapor deposition (PECVD) on glass (Fig. 5) [42]. The α-Si substrates were etched at room temperature in HF/$AgNO_3$ aqueous etchant with different $AgNO_3$ concentrations. The doping type and the concentration of carbon in α-Si film turned out to affect heavily the etching feature of α-Si. The etching of phosphorus doped α-Si is relatively slow, resulting in shallow pits on the surface of α-Si film. In contrast, boron doped α-Si is etched very fast, and α-Si deposited on glass is completely etched at the very beginning of etching. The typical morphology of un-doped α-Si film in HF/$AgNO_3$ aqueous etchant is similar to that of crystalline Si. Interestingly, the etching proceeds along the direction normal to the film surface, resulting in SiNWs vertically aligned on glass, whereas the etching of carbon-containing α-Si results in curved SiNWs, of which orientation deviates from the surface normal. The etching rate of α-Si decreases with increasing carbon concentration in α-Si, and α-Si with carbon concentration larger than 7% cannot be etched into SiNWs via MACE. In addition, the diameter of SiNWs and the density of SiNWs decrease with increasing carbon concentration. The influence of carbon concentration in α-Si film on the etching rate and the feature of resulting SiNWs are attributed to the less preferential dissolution of Si—C bond in etchant than that of Si—Si bond, and/or the less favorable holes injection into α-$Si_{1-x}C_x$.

New etching systems

So far, the primary catalysts for MACE are Ag, Au, and Pt because of their stability in HF and H_2O_2 solution along with their catalytic ability for the reduction of H_2O_2. Apart from their high cost, one of the main drawbacks of these noble metal catalysts in MACE is their diffusivity in Si, which is detrimental to the performance of CMOS (Complementary Metal Oxide Semiconductor) devises. Tungsten (W) deposited by sputtering can be used as catalyst in MACE [43]. The morphology of etched Si correlates with H_2O_2 concentration in etchants. The solution with low H_2O_2 concentration provides high feature resolution with holes that conform to the size and shape of the catalyst particles, while etchant with much higher H_2O_2 concentration creates large holes, which are between 50 and 800 nm in diameter and surrounded by a region about 1000 nm wide. The etching rate of Si loaded with W is lower than those with traditional MACE catalysts, which is ascribed to the lower catalytic capabilities of W for H_2O_2 reduction.

Nickel (Ni) is also employed as catalyst in MACE to fabricate Si structures with low reflectivity [44]. In a typical experiment, planar Si (Fig. 6a and b) or pyramid-textured Si (p-type, 100, 2 Ω cm) (Fig. 6c and d) was deposited with Ni nanoparticles by magnetron sputtering method, and then etched in a mixed solution of H_2O_2 (4 mL), HF (8 mL) and deionized water (40 mL) for 5 min at room temperature. The etching behavior of Si wafer loaded with isolated Ni particles (ca. 10—20 diameter) is different from that loaded with noble metals. Instead of well-defined nanopores or nanowires, rhombic nanostructures with 50—100 nm size on the surface of planar and pyramidal Si surface can be found. On the other hand, 5 min etching results in ca. 120 nm etching depth, indicating a much slower etching rate in the case of Ni metal, compared to Ag, Au, or Pt.

In MACE, FIB has also been used to deposit catalyst on the surface of Si wafer with fine control over the catalyst morphology. However, gallium ions (Ga^+) implanted during FIB process participate in the dissolution of Si in MACE [45]. In MACE experiments with Pt catalyst deposited by FIB, the feature fidelity turned out to be rather poor, although the resulting etched structure follows the profile of catalyst. Secondary etching occurred extensively around metal catalyst. In addition, the Si areas exposed to Ga^+ ions produced gas bubbles and turned black, indicating that MACE occurs in these areas. Systematic investigations revealed further that etch depth induced by Ga^+ depends heavily on the accelerating voltage used along with etching time for low doses, and the width of peripheral etching region depends primarily on dose, while the slope of the peripheral region depends on both accelerating voltage and dose, and the etching rate is shown to increase at high doses.

Ti metal was introduced to HF/H_2O_2 aqueous etchant to etch Ag-loaded Si (n-type, 100, 0.01 Ω cm) [46]. The etching rate of Ag-loaded Si decreases with increasing Ti concentration. This decrease was attributed to the lowering of H_2O_2 concentration in etchant, because TiF_6^{2+} produced by the reaction of Ti and HF can complex with H_2O_2 to form $[TiF_6(H_2O_2)]^{2+}$. The decrease of etching rate can reduce the prominent defect (P_b^0) at Si/SiO_2 interface, and decrease the concentration of dangling bonds at the interface of Si/SiO_2.

AgO (insoluble) [47] and Ag_2O (soluble) [48] have been utilized instead of $AgNO_3$ in one-step MACE. The major phenomena during MACE are similar to those occurring in HF/$AgNO_3$ etchant, being SiNWs covered with Ag dendrites (Fig. 7a and b). The activation energy of Si etching in HF/AgO and HF/Ag_2O were extracted from the relations between etching rates of Si and temperature, being 0.20 eV in HF/AgO etchant [47] and 0.15 eV in HF/Ag_2O etchant [48]. These two values are both smaller than that in HF/$AgNO_3$

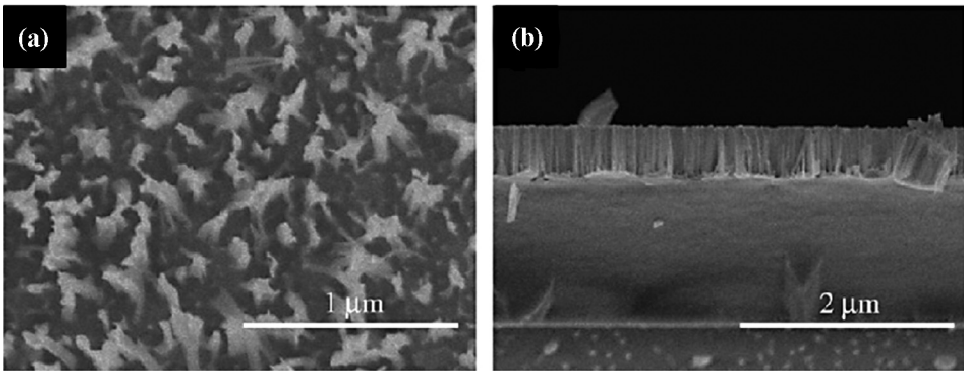

Fig. 5 (a) Plan view and (b) cross-sectional view SEM images of MACE of α-Si:H [42]. Copyright 2011, Elsevier Ltd.

(0.36 eV), suggesting that the formation processes of SiNWs in HF/AgO and HF/Ag_2O are more diffusion-limited than that in HF/$AgNO_3$ solution. The dependences of SiNWs length on the concentration are different for the etching in HF/AgO and HF/Ag_2O. In HF/AgO etchant, the length of SiNWs firstly increases with the concentration of AgO under the same HF concentration and etching time (Fig. 7c). But further increase of AgO concentration will not change the length of SiNWs. In HF/Ag_2O etchant, the length of SiNWs also increases with Ag_2O concentration, whereas the SiNWs length decreases with further increasing Ag_2O concentration, and no SiNWs but rough surface is formed for [Ag_2O] > 0.1 M (Fig. 7d).

In MACE, HF is the most commonly used etchant for the dissolution of Si or SiO. Besides HF, other fluoride-based etchants have been tried, including buffered oxide etchant [49], NH_3·2HF [50,51], $NaBF_4$ [52], and so on. In these experiments, the mechanism responsible for Si etching is similar to that using HF as etchant. In the case of two-step MACE using NH_3·2HF, it is necessary to lower pH to obtain SiNWs, and the length of SiNWs increases with decreasing pH [50]. In case that $NaBF_4$ acts as an etchant, Si rods with tapered shape, rather than SiNWs, can be obtained. The detailed morphologies of tapered rods are determined by the doping level of Si wafer, with higher doping level resulting in shorter length [52].

The MACE process is influenced by various factors. The volume of etchant (HF/H_2O_2) in two steps etching influences the morphology of the final Si structures [53]. In etchant with smaller volume, pores are created, whereas larger volume yields nanostructures composed of SiNWs and pores. In addition, the length of the resulting Si nanostructures increases with etchant volume. This result correlates with the different capabilities of reactant replenishing from the

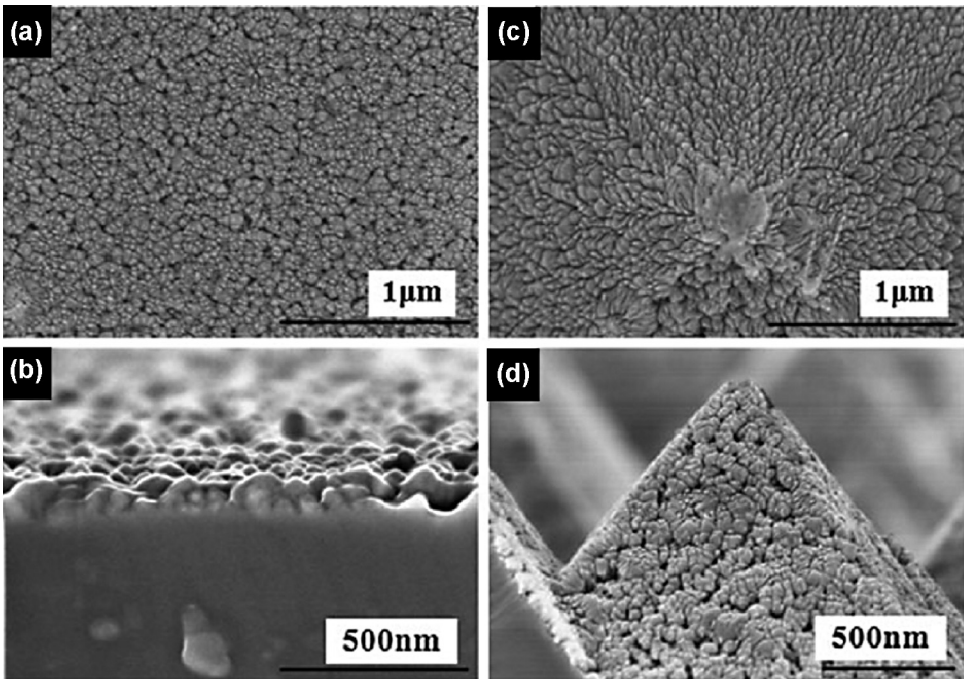

Fig. 6 (a) Plan-view and (b) cross-sectional view SEM images of planar Si using Ni nanoparticles as catalyst, (c) plan-view and (d) cross-sectional view SEM images of pyramid-textured Si using Ni nanoparticles as catalyst. Reproduced with permission from Ref. [44]. Copyright 2013, Springer.

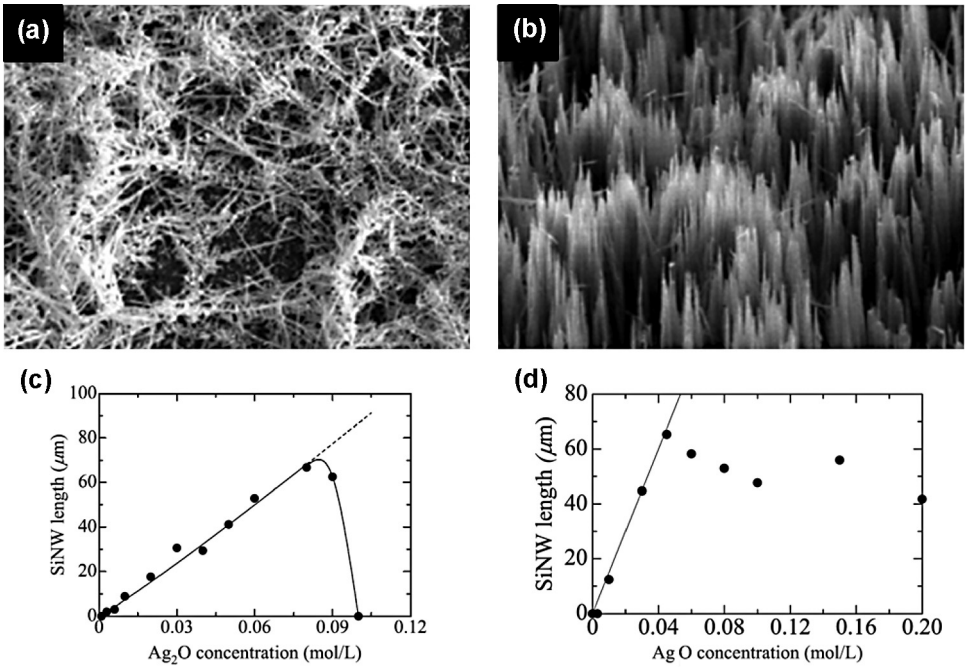

Fig. 7 Typical SEM images of Si etched in HF/Ag_2O aqueous etchant (a) before and (b) after removal of surface Ag dendrites. The relation of SiNWs length and the concentration of (c) Ag_2O and (d) AgO. Panels a—c were reproduced with permission from Ref. [48]. Copyright 2012, Elsevier Ltd. Panel d was reproduced with permission from Ref. [47]. Copyright 2011, The Electrochemical Society.

bulk etchant. A larger etchant volume might afford more efficient reactant replenishing.

It has been well documented that, in etchant with high molarity ratio of H_2O_2 to HF, excess holes (h^+) can readily diffuse from catalyst inducing pits away from catalyst. Besides decreasing H_2O_2 molarity, one way to vary the injection rate of holes (h^+) is to change the supply of H^+ ions at catalyst/liquid interface by adding NaCl to etchant [54,55]. Na^+ ions dissociating from NaCl are attracted to negatively charged catalyst, reducing the number of H^+ ions at catalyst surface. Because H^+ ions are necessary for the reduction of H_2O_2 ($H_2O_2 + 2H^+ \rightarrow 2H_2O + 2h^+$) and also for the generation of holes (h^+), the decrease of H^+ ions on catalyst surface can reduce the number of holes (h^+) injected into Si. Another way to suppress excess holes (h^+) is to apply extra electric field, which directs excess holes (h^+) to the back of Si wafer and reduces excess holes (h^+) near etching front [54,55].

Organic solvent affects the morphology of nanostructures resulting from MACE. The etchant with higher ethanol concentration yields SiNWs with larger taper angle [56]. Azerodo et al. proposed that the presence of ethanol reduces holes (h^+) consumption rate near catalyst, so that more holes (h^+) can diffuse to the sidewall of SiNWs, facilitating the etching near the tip of SiNWs [56]. The introduction of EG into etchant changes the morphology of SiNWs from solid to porous [35]. The introduction of co-solvent not only decreases etching rate, but also influences etching direction [18], as discussed in the section 'Etching directions'.

Because the potential of the valence band maximum (PVBM) at the Si/metal interface is more negative than that at the Si/electrolyte interface, holes (h^+) injected from back contact are driven preferentially to Si/metal interface (Fig. 8a). Consequently, Si below metal is electrochemically etched much faster than metal-free Si surface. Therefore, metals, for example, Cu (Fig. 8b) and Ag, can be utilized to catalyze electrochemical etching. Meanwhile, metal-assisted electrochemical etching method enables convenient control over the etching direction of non-(1 0 0) substrates, and facilitates the fabrication of orientation-modulated silicon nanostructures (Fig. 8c) [57].

Engineering of etched Si morphology

Zigzag silicon nanowires

In sealed reaction vessel, Si(1 1 1) substrate (including n-type and p-type) etched with HF/$AgNO_3$ aqueous etchant exhibits temperature-correlated morphology [16]. Below 25 °C, the etching of Si substrate proceeds along one direction (Fig. 9a), resulting in straight SiNWs. On the other hand, zigzag SiNWs can be formed at etching temperature higher than 55 °C (Fig. 9b). Higher Ag^+ concentration or higher etching temperature facilitates the formation of zigzag SiNWs. Three types of zigzag nanowires can be distinguished according to the crystalline orientation of repeatedly alternating segments, being ⟨1 1 1⟩/⟨1 1 3⟩, ⟨1 1 1⟩/⟨1 0 0⟩, as well as ⟨1 0 0⟩/⟨1 0 0⟩. Two possible processes were proposed for the formation of these zigzag structures. A single-particle etching process occurs during the formation of ⟨1 1 1⟩/⟨1 1 3⟩ zigzag nanowires, where the moving direction of individual Ag particle switches between nearby directions (i.e., ⟨1 1 1⟩ and ⟨1 1 3⟩). The switch of etching direction is attributed to

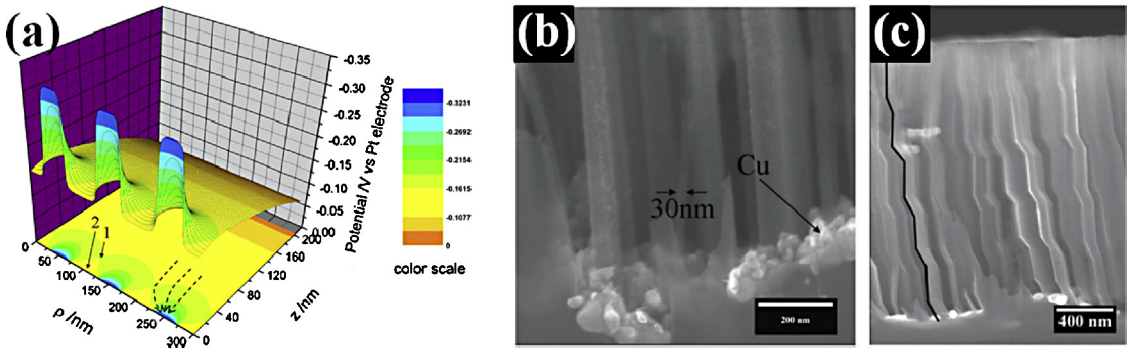

Fig. 8 (a) The computed potential of the valence band maximum (PVBM) of a Si substrate in contact with an array of 50 nm diameter Ag patches distributed from $\rho = -450$ to 450 nm with a 100 nm interval. The contour of PVBM is projected on the ρ—z plane. (b) SiNWs resulted from Cu assisted electrochemical etching of Si. (c) Orientation modulated SiNWs resulted from Ag assisted electrochemical etching of Si using different current density [57]. Copyright 2010, IOP Publishing Ltd.

perturbations at reaction sites possibly induced by hydrogen bubbles. Because both the ⟨1 1 1⟩ and ⟨1 1 3⟩ directions are not the preferred etching direction of Si, the etching direction can easily be switched by perturbations between these two directions, whilst the perturbation is insufficiently large to switch the etching direction from ⟨1 1 1⟩ to ⟨1 0 0⟩ because of the large angle between ⟨1 0 0⟩ and ⟨1 1 1⟩ directions. Another process is multi-particle etching mechanism. If etching is sufficiently activated (e.g., higher temperature or Ag^+ concentration), Ag particles can alternate their moving directions along ⟨1 1 1⟩ and ⟨1 0 0⟩, or different ⟨1 0 0⟩ directions. In this case, merging of moving tracks of different Ag particles results in ⟨1 1 1⟩/⟨1 0 0⟩ or ⟨1 0 0⟩/⟨1 0 0⟩ zigzag nanowires. In addition, it is found that zigzag SiNWs prefer to be formed at region with rough surface, providing a practical approach to fabricate SiNWs with different shapes on selected regions.

Si(1 1 1) substrate loaded with Ag particles can also be etched into zigzag SiNWs in HF/H_2O_2 aqueous solution at room temperature [28]. The catalytic decomposition of H_2O_2 by Ag particles during etching is a strongly exothermic reaction, so that the temperature of etching solution substantially increases. The formation of zigzag SiNWs was attributed to inherent temperature rise during the etching.

Besides temperature and bubbles stimulation, the etching direction can also be modulated by inherent concentration variation near etching front. An example is the etching of Au-mesh-loaded Si(1 0 0) substrate in HF/H_2O_2 aqueous solution (Fig. 9c). In HF/H_2O_2 etchant with low H_2O_2 concentration, Si(1 0 0) substrate is etched along [1 0 0] direction, whereas Si(1 0 0) substrate is etched along non-⟨1 0 0⟩ directions in etchant with high H_2O_2 concentration. This feature is attributed to holes (h^+) injection mechanism. For an etchant solution composed of low relative H_2O_2

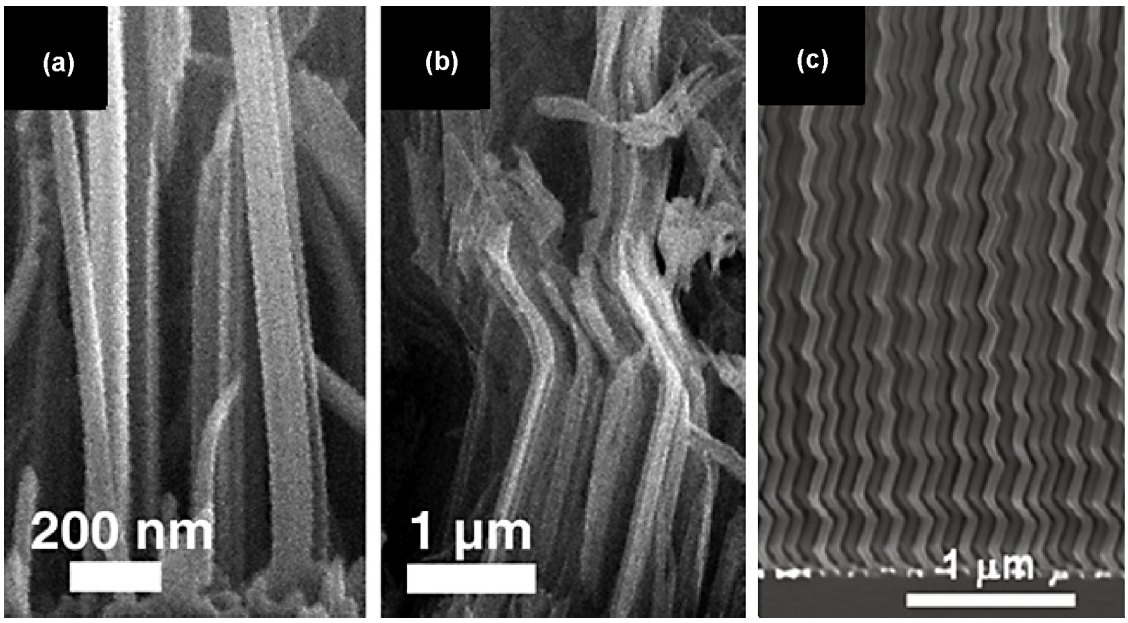

Fig. 9 Cross-sectional SEM images of (1 1 1) Si etched in $HF/AgNO_3$ aqueous etchant at (a) 15 °C and (b) 55 °C [16]. Copyright 2010, The American Chemical Society. (c) Cross-section SEM image of Au-mesh-loaded Si(100) etched in HF/H_2O_2 aqueous etchant, showing vertically aligned zigzag SiNW [12]. Copyright 2011, The American Chemical Society.

concentration, generation of positive holes (h^+) at low temperature will be limited, and thus hole (h^+) injection into Si will be localized at the least compact (1 0 0) plane with the fewest Si back bonds to break, resulting in etching along the [1 0 0] direction. At high temperature the amount of generated hole (h^+) is expected to be increased because of the enhanced catalytic decomposition of H_2O_2 and also the thermally activated hole (h^+) injection. In this case, Si atoms from more compact crystal planes with higher density of Si back bond become liable to be oxidized and etched, resulting in etching along non-⟨1 0 0⟩ directions. During etching, the chemical etching will quickly deplete H_2O_2 near etching front, resulting in a vertical [1 0 0] etching. Meanwhile, the vertical diffusion of H_2O_2 from bulk solution will gradually increase the concentration of H_2O_2 near etching front. If the concentration of H_2O_2 is increased to sufficiently large value, the etching direction can be switch to non-⟨1 0 0⟩ directions. This depletion and influx cycle of H_2O_2 at etching front induces periodic oscillations of etching direction, resulting in zigzag SiNWs [12].

Barcode silicon nanowires

The porosity of Si can be modulated by deliberately changing the concentration of H_2O_2 in etchant. P-type Si wafer (<0.005 Ω cm) etched in 0.1 M H_2O_2 results in 47% porosity and 6.1 nm peak pore size, while the same substrate etched in 0.2 M H_2O_2 results in 66% porosity and 11.4 nm pores [38]. Thus, barcode SiNWs with periodical variation of porosity along the major axis of SiNWs can be fabricated by etching Ag or Au loaded heavily doped Si wafer alternatively in etchant with different H_2O_2 concentrations (Fig. 10) [38]. The porosity transition between adjacent segments occurs within a few nanometers, indicating a prompt response to the change of H_2O_2 concentration. Etchant with low relative HF concentration etches Au-loaded Si into porous structure, whereas that with high relative HF concentration to nonporous one. As a consequence, the depletion of HF at etching front and recovery of HF by diffusion from bulk etchant occurring simultaneously and repeatedly during etching result in formation of alternative solid/porous segments [12].

Porosity modulations of SiNWs can also be achieved by applying periodic pulses of anodic bias during Au mesh-loaded Si(1 0 0) wafer (Fig. 11a–c) [58]. In this method, an applied anodic potential pulse selectively porosifies the area of SiNWs contacting with the Au mesh via potential-driven localized injection of the extra amount of positive holes (h^+) into the valence band of silicon through the gold-silicon interface. Accordingly, pulse duration (τ_{ano}) and period (τ_{int}) determine the lengths of porous and non-porous segment, respectively. On the other hand, the amplitude (U_{ano}) of potential pulse determines the degree of porosification (Fig. 11e). A similar approach for fabrication of porosity modulated SiNWs has also been reported recently with periodic current pulses [59].

Three-dimensional silicon structures

The motion of catalyst can be modulated by employing catalyst with specifically designed morphology, and accordingly 3D Si structures can be fabricated by MACE. If the DoF for the motion of metal catalyst is confined, metal catalyst can rotate about an axis parallel to Si surface (Fig. 12a and b) [60,61]. Such confinement can be achieved via pinning metal catalyst with carbon deposited by electron beam or pinning the arms of square or circular metal pad with polymer. Besides pinned catalyst, starlike metal catalyst enables the control fabrication of 3D spirals in Si substrate, with rotating axis parallel to surface normal (Fig. 12c) [25]. The rotation direction of starlike metal catalyst correlates with its morphology, including arm shape, diameter, arm length, arm number, thickness, and so on.

Porous Si powders and nanowires etched from Si powders

The promising application potential of Si in Li ion battery stimulates the research concerning low-cost and large-scale fabrication of Si nanostructures. MACE of polycrystalline Si (or SiO) powder is candidate approach. In this approach, the process and etching mechanism are similar to that of MACE using single crystalline Si wafers as starting material. In one-step MACE of Si powder in HF/$AgNO_3$ [62,63] or HF/$PtCl_2$ [64] etchant, Si powder with macroporous surface can be obtained. It is worth noting that the shape of Ag aggregates formed on the surface of Si powder is different from dendrite structure formed on the surface of Si wafers. Although the reason is not clearly understood yet, large surface area of Si powder is believed to be a key determining factor [62]. One step etching of Si powder can also be carried out in HF/$FeCl_3$ solution [65]. Because the etching reaction ($Si + Fe^{3+} + 6HF \rightarrow H_2SiF_6 + Fe^{2+} + 4H^+ + 3e^-$) is exothermic, the temperature of etching solution with an initial value of 20 °C can reach 80 °C in 5 min. The specific surface area (SSA) of the resulting porous Si powder is influenced by temperature. The reaction carried out under 20 °C yields Si powders with 60 m^2/g (SSA), and the SSA increases with decreasing temperature, from 125 m^2/g (4 °C), to 403 m^2/g (−15 °C) and further to 480 m^2/g (−25 °C).

Two-step MACE of Si or SiO powder produces porous Si particles [66]. The deposition of Ag on the surface of Si or SiO powder can be achieved either by immersing the powder in HF/$AgNO_3$ aqueous solution (Fig. 13a) [66,67] or by the reduction of $AgNO_3$/ammonia solution with glucose [68]. The second step etching is carried out in HF/H_2O_2 aqueous etchant. The SSA of the resulting porous Si powder is ca. 14 m^2/g [66]. Si powders can be etched into well-defined SiNWs bundles in a modified two-step etching process (Fig. 13b) [69]. In this approach, Si powders were added to stirring HF/$AgNO_3$ aqueous solution for 30 seconds, and H_2O_2 was added directly into the mixture of Si powders and etchant. With increasing reaction time, the morphology of the reaction product evolves from Si powder with surface nanowires, to SiNWs bundles and isolated SiNWs, and the SSA is increased from 12 m^2/g (10 min etching) to 20 m^2/g (60 min etching).

Transferring silicon nanowires

In an initial procedure of SiNWs transfer [70], receiver substrate was first spin-coated with a thin layer (ca. 400 nm)

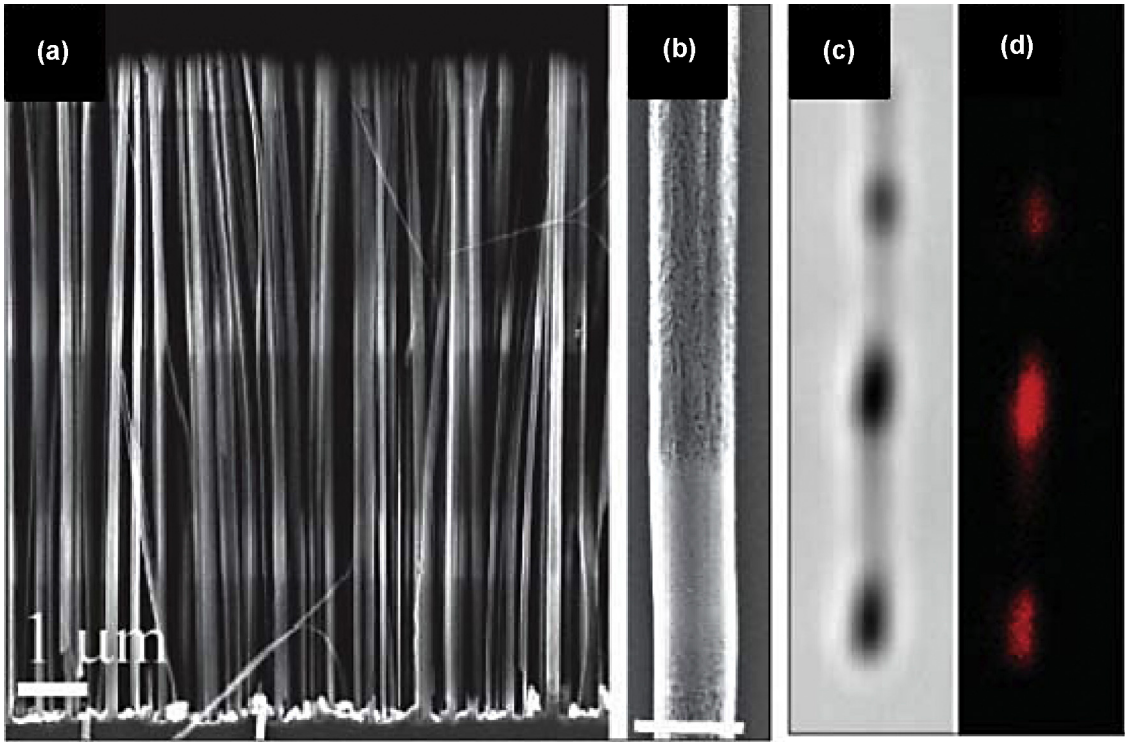

Fig. 10 Cross-sectional SEM images of barcode SiNWs: (a) overview and (b) close-up view. Confocal microscopy images of a single barcode SiNW: (c) bright-field image and (d) fluorescence image. Reproduced with permission from Ref. [38]. Copyright 2010, Wiley-VCH Verlag GmbH & Co. KGaA, Weinheim.

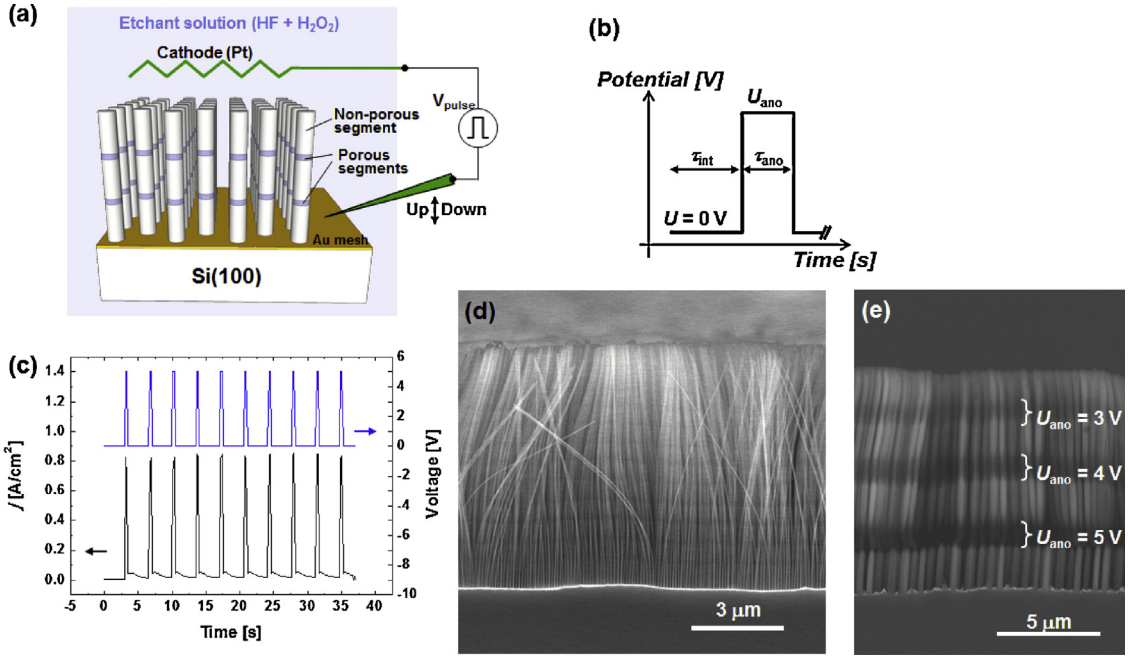

Fig. 11 (a) A schematic showing an electrochemical setup employed for periodic pulsing of anodic potential during MACE of silicon. (b) A typical pulse scheme, where U_{ano} and τ_{ano} denote the amplitude and width of anodic potential pulses, respectively, and τ_{int} denotes the pulse interval. (c and d) A typical current–time (j–t) transient during chemical etching of silicon with U_{ano} = 5 V, τ_{ano} = 0.2 s, and τ_{int} = 3 s, and a representative SEM micrograph of the resulting porosity-patterned [1 0 0] SiNWs, respectively. (e) An SEM image of [1 0 0] SiNWs prepared by pulsing of anodic bias during MACE of Si(1 0 0) wafer, showing the effect of pulse amplitude (U_{ano}) on the degree of porosification. Reproduced with permission from Ref. [58]. Copyright 2011, The Royal Society of Chemistry.

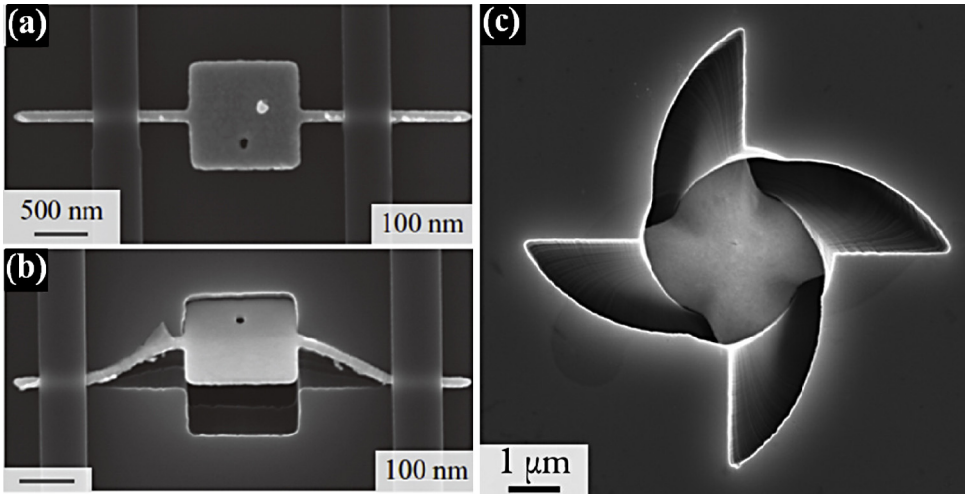

Fig. 12 Out-of-plane rotation of Ti/Au catalyst pinned with polymer during MACE. The arm width is 100 nm and the average arm length is (a) 450 nm and (b) 930 nm [61]. Copyright 2011, Wiley-VCH Verlag GmbH & Co. KGaA, Weinheim. (c) 3D spirals structure in Si resulted from MACE [25]. Copyright 2012, The American Chemical Society.

poly(methyl methacrylate) (PMMA). Afterward, the receiver substrate was heated to 200 °C, well above the glass transition temperature of PMMA (105 °C). Afterward, Si substrate with SiNWs fabricated by MACE was pressed against to the receiver substrate and held for a certain period of time. When the temperature of the whole setup was decreased below the glass transition temperature of PMMA, force was applied to the edge of Si wafer to detach it from the receive substrate. By this approach, vertically aligned SiNWs can be transferred to the receiver substrate. The length of transferred SiNWs is slightly shorter than the length of SiNWs on Si substrate. In a similar approach, ordered SiNWs fabricated by Au meshes film were conformally entrapped by a poly(vinylidene fluroriderandom-hexafluoropropylene) copolymer via successive polymer coatings and the subsequent drying step, and then the polymer composite of SiNWs was mechanically peeled to obtain a freestanding SiNWs/polymer membrane. It is worth noting that Au meshes film is left on the residual Si substrate even after peeling, preserving its original integrity. Such Au meshes film can be reused to catalyze the etching of residual Si substrate into SiNWs. Therefore, MACE-polymer infiltration-peeling procedures can be carried out repeatedly without requirement of Au meshes film re-deposition, and the number of the attainable SiNWs/polymer membrane is only limited by the initial thickness of Si subatrate [71]. In this approach, sufficiently large mechanical force is necessary to detach SiNWs from the silicon substrate. This drawback can be circumvented by selectively weakening the every root of SiNWs.

One method is that Si substrate is etched firstly in HF/H_2O_2 aqueous etchant with low H_2O_2 concentration, and then the Si substrate is etched in HF solution containing high H_2O_2 concentration [72—75]. The increase of H_2O_2 concentration slows down the etching rate along ⟨1 0 0⟩ directions and Si near Ag particles is etched isotropically. The isotropic etching near the root of SiNWs makes this part fragile, and facilitates the transfer process. The etched morphology near the root of SiNWs is influenced by the concentration of H_2O_2 in the step of isotropic etching [73]. By 20 s of isotropic etching with $HF/H_2O_2 = 1/1$ (v/v), many small caves are formed

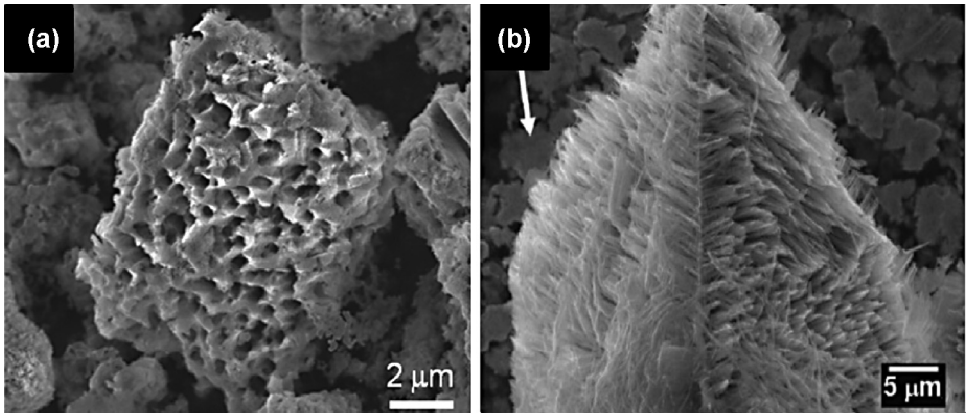

Fig. 13 (a) Macroporous Si powder fabricated by MACE [66]. Copyright 2012, Wiley-VCH Verlag GmbH & Co. KGaA, Weinheim. (b) SiNWs bundles etched from Si powders [69]. The white arrow in (b) indicates silver glue used to bind SiNWs powders to copper plate for SEM observation. Copyright 2011, The American Chemical Society.

at the bottom of SiNWs, making the entire SiNWs thin film about to be detached from bulk Si substrate. The thickness of SiNWs thin film is slightly shorter than the length of SiNWs formed in the first step etching. When the isotropic etching is carried out with $HF/H_2O_2 = 1/0.6$ for 90 s, the isotropic etching is accompanied with the anisotropic etching along [1 0 0] direction. It has been demonstrated that the bulk Si substrate with surface SiNWs transferred to other substrates can be re-utilized to fabricate SiNWs via MACE, and can be used further in second round transfer of SiNWs [74].

The weakening of SiNWs root can also be achieved by combining the delamination of Ag and re-etching (Fig. 14a) [76,77]. In details, SiNWs was firstly fabricated by etching of Ag-loaded Si substrate in HF/H_2O_2 aqueous etchant. Once the length of SiNWs was increased to a desired value, the Si substrate was rinsed, dried, and then soaked in deionized water (75 °C) for about 3 h. Afterward, the Si substrate was promptly dried and immediately etched again in HF/H_2O_2. A horizontal crack was formed at the start of the second etching, whilst the vertical etching proceeds to elongate SiNWs. Soaking of Si substrate in hot water induces delamination of Ag film, and increases Ag/etchant interface in the second step etching. Therefore, the dissolution of Ag into Ag^+ by etchant is speeded up. Ag particles will be re-deposited on the sidewall of SiNWs near Ag film, and these small Ag particles induce the horizontal etching of SiNWs, leading to the formation of crack (Fig. 14b and c). The crack facilitates the breakage of SiNWs from bulk Si substrate in transfer procedures.

Another approach to facilitate the breakage of SiNWs from the bulk Si substrate is to introduce a sacrificial porous Si layer underneath SiNWs by electrochemical etching (Fig. 14d) [59]. One key requirement of the introduction of sacrificial porous Si layer is that the width of space charge region of Si is larger than the diameter of SiNWs, so that SiNWs is depleted during electrochemical etching and porous layer will be formed only underneath SiNWs. Another requirement is that the concentration of HF in electrolyte used in electrochemical etching is sufficiently low, so that Si surface is etched into a continuous porous layer instead of individual marcropore. This method can be applied to SiNWs fabricated by MACE or reactive ion etching (RIE) (Fig. 14e). On the other hand, the alignment and structure of SiNWs are kept intact by the porous layer during the transfer. In addition, Si wafer can be repeatedly used to form vertical SiNWs by etching and transferring SiNWs to different substrates.

SiNWs with tailored shapes

It has been well demonstrated that SiNWs prepared by MACE can efficiently trap incident photons, stimulating further tailoring of SiNWs morphology for more efficient light trapping [78—82]. Si micropillars (SiMPs)/SiNWs composites can be facilely fabricated by one-step MACE process without using any template [80]. The key point is to introduce K^+ into etchant. K^+ will react with the by-product of Si etching (SiF_6^{2-}), resulting in insoluble K_2SiF_6. K_2SiF_6 precipitates load on the surface of Si substrate and protect underneath Si from etching, behaving as mask for the formation of SiMPs during etching. Meanwhile, Si without K_2SiF_6 coverage will be etched into SiNWs with diameters ranging in 30—300 nm.

Si structures with different fraction of Si at different depth can be fabricated by two etching steps [81]. In the first step, Ag particles were plated onto Si substrate using $HF/AgNO_3$ aqueous solution, and then Si substrate was immersed in a diluted HNO_3 (6%) solution. This treatment can partially detach or dissolve pre-deposited Ag particles, and the surface density of Ag particles on Si surface is significantly decreased by two orders of magnitude. The resulting Si substrate with well separated Ag particles was etched in HF/H_2O_2 aqueous solution, leading to widely separated Si nanopores (SiNPs). After the removal of Ag at the bottom of SiNPs by concentrated HNO_3, the Si substrate was subjected to the second step etching to form SiNWs, including the deposition of Ag particles by $HF/AgNO_3$ and the etching of Si in HF/H_2O_2. The combination of SiNPs and SiNWs essentially introduces the gradient reflection index, and shows superior anti-reflection capability in comparison with SiNPs or SiNWs with the same thickness.

Tapered SiNWs further suppress optical reflection over abroad range of wavelength due to a minimized Fresnel reflection originating from a gradual transition of the effective refractive indexes, in comparison with SiNWs [78,79,82]. Tapered SiNWs can be obtained by anisotropic etching of SiNWs formed MACE via KOH immersion. In a basic solution, the etching rate of Si depends heavily upon the bond strengths of surface atoms. Top corner edges of SiNWs have weak bond strength because of a drastic transition of surface atom densities over the short distance of the corner edges. This results in a faster etching rate at the corner edges than at other flat regions, thereby enables the formation of sharp tip and a tapered shape on the top-ends of the SiNWs. This site-specific reactivity of SiNWs is also found in the deposition of Ag onto SiNWs, being that the top corner edges of SiNWs are preferentially deposited with Ag particles in $HF/AgNO_3/H_2O_2$ (and/or HNO_3) [82]. Truncated SiNWs can be fabricated by immersing of SiNWs in $HF/AgNO_3/H_2O_2$ (and/or HNO_3) solution and the following HNO_3 removal of Ag particles. The repeated treatments can tailor the shape of SiNWs, from nanopillars, to nanorod, nanopencil, and nanocones (Fig. 15). Using $NaBF_4$ instead of HF, tapered SiNWs can be fabricated via one-step etching [52].

New techniques for controlled fabrication of Si structures

Ag mirror reaction has been utilized to deposit Ag particles on Si substrate for MACE [83—85]. Ag particles resulted from Ag mirror reaction have wide range of particle sizes, from 100 nm to larger than 1 μm. Their morphology correlates with the orientation of Si wafer, with hexagonal-aspect particles more prevalent on Si(1 1 1). The morphologies of the resulting Si nanostructures depend on etching time. For example, being etched in HF (49%):H_2O_2 (30%):ethanol (v:v:v = 1:1:1) in the time scale of 0—30 min, only rough and irregular structure could be obtained [84], whereas when reaction time was extended to 12 h, well-defined pores with diameters ranging from 1 to 4 μm were formed [83]. The shapes of pores are different on Si substrates with different orientations, being rectangular in Si(1 0 0) and hexagonal in Si(1 1 1) (Fig. 16).

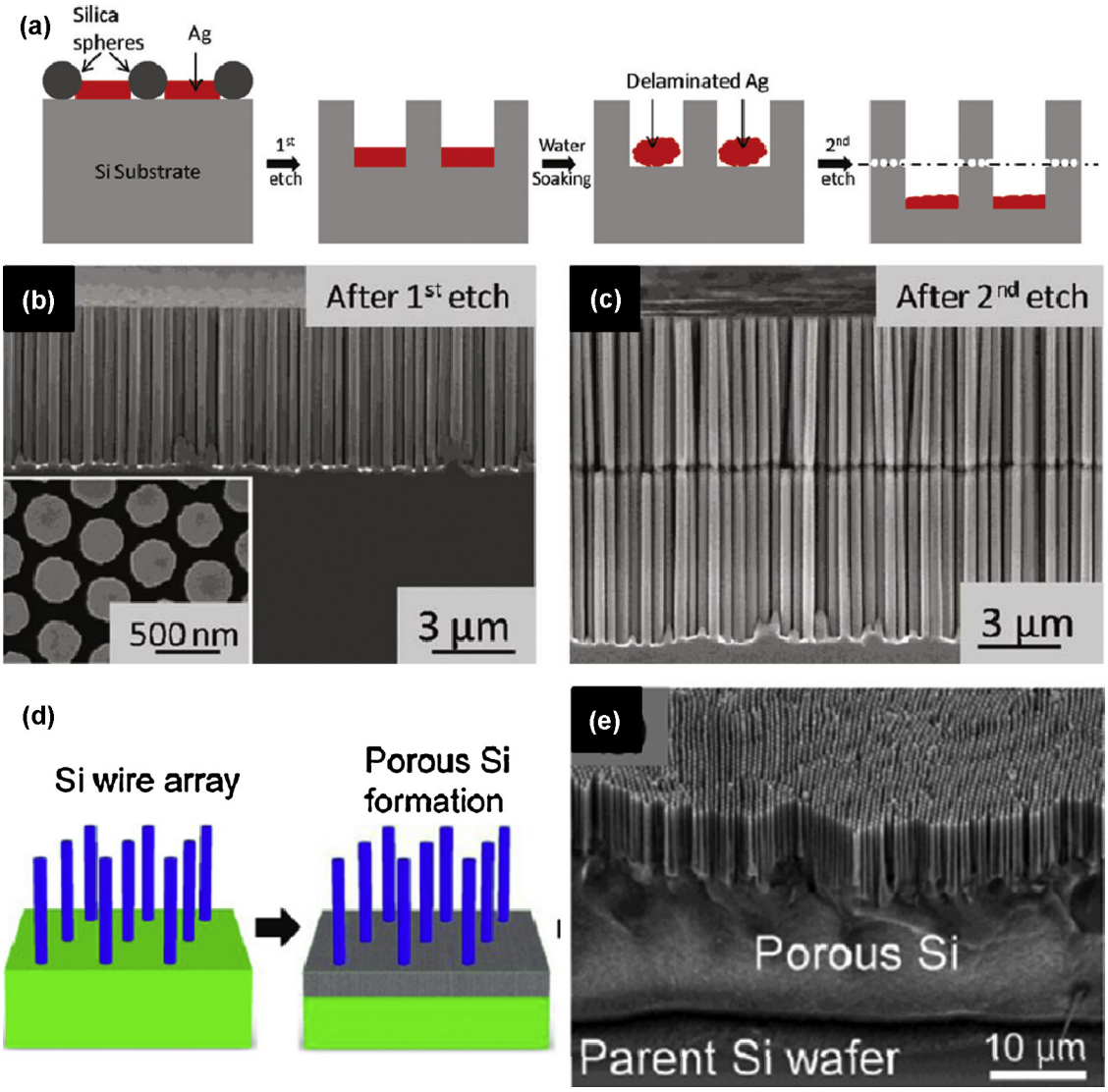

Fig. 14 (a) Schematic procedure for weakening SiNWs root by the delamination of Ag and re-etching. SEM images of SiNWs (b) prior to and (c) after root weakening. Panels a—c were reproduced with permission from Ref. [76]. Copyright 2011, The American Chemical Society. (d) Schematic procedure of weakening SiNWs root by electrochemical etching. (e) SEM image of SiNWs on porous Si layer. Panels d and e were reproduced with permission from Ref. [59]. Copyright 2013, The American Chemical Society.

Dewetting process has been employed to modulate the morphology of Ag on Si substrate [56,86—88]. In a typical process, Ag film is deposited onto Si wafer by thermal evaporation. Then Ag-loaded Si substrate is annealed at N_2 atmosphere. The temperatures in the range of 150—700 °C have been adopted for dewetting process. On the other hand, Ag inks can be spin-coated onto Si substrate and then subjected to annealing treatment, enabling the dewetting of Ag inks [89]. The final morphology of Ag correlates with its initial thickness, temperature and time of dewetting process. Isolated Ag particles and Ag film with holes can be obtained by dewetting, and the size and distribution of Ag particles or holes in Ag film can be manipulated, enabling lithography-free fabrication of SiNWs or pores with controlled size and distribution.

Besides electroless plating, thermal evaporation, and sputtering, noble metal fabricated by other methods can also be deposited onto Si substrate (e.g., spin-coating) to act as catalyst in MACE [9,23]. Ag nanowires were synthesized by a polyol method in a millifluidic reaction and deposited on Si substrate by drop casting. MACE was carried out after annealing, which can improve the physical contact between Ag nanowires [23] and Si substrate. Holes can be obtained on Si substrate, with the cross-section of hole matching that of Ag nanowires [23].

To obtain well ordered SiNWs, it is necessary to utilize noble metal meshes film with well-ordered pores as catalyst. Anodic aluminum oxide (AAO) has been used as template to grow many order nanostructures, with ordering range of pores larger than several micrometers. The utilization of AAO to define noble metal mesh in MACE was previously demonstrated [90]. In this method, the AAO membrane was transferred to the surface of Si substrate prior to the deposition of metal meshes film. In an improved approach,

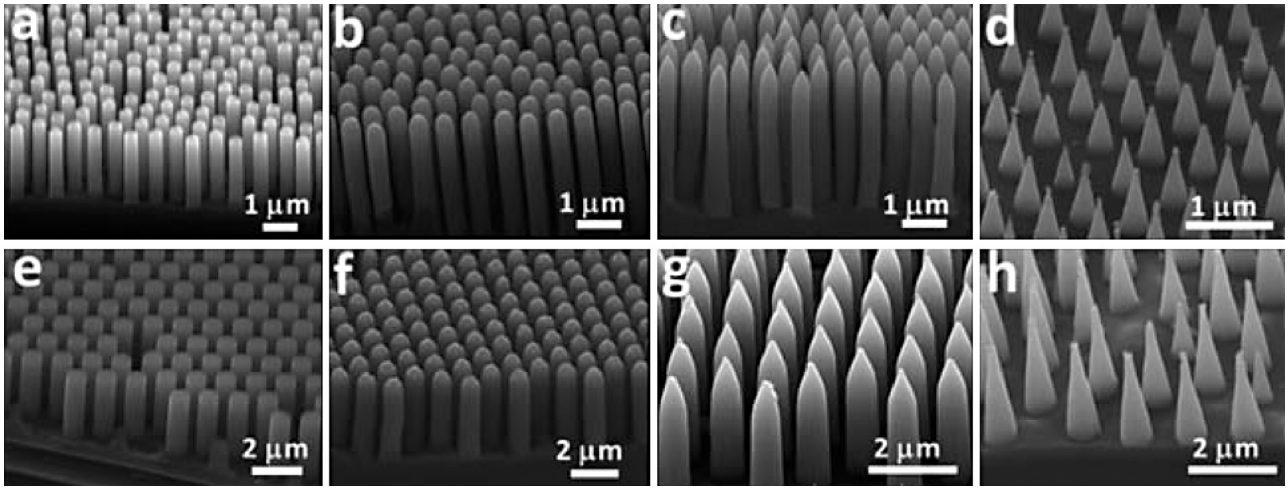

Fig. 15 SEM images of (a and e) nanopillar, (b and f) nanorod, (c and g) nanopencil, and (d and h) nanocone arrays [82]. Copyright 2013, The Royal Society of Chemistry.

on the other hand, the transfer of AAO membrane to the surface of silicon is not necessary. Noble metal film was deposited directly onto AAO substrate by sputtering, and then AAO membrane was floated onto the surface of an etching solution to release metal mesh from AAO membrane. The resulting metal mesh remained floating on the surface of the aqueous etching solution and could be easily transferred onto Si substrate (Fig. 17). Subsequently, the sample was dried and a conformal contact between the metal mesh and the underlying Si surface was established, so that the metal mesh was not separated from Si surface even if the sample was exposed to a strong stream of water or nitrogen. Afterwards, Si loaded with metal mesh was subjected to MACE and etched into well-ordered SiNWs [12,91,92]. This method has been further improved so that AAO mask can be re-used for the fabrication of noble metal mesh [93]. A thin Ag (~10 nm) was deposited onto AAO prior to the deposition of Au. Because of the low surface energy of metal layers, the Au/Ag-coated AAO membrane was floated on the surface of Ag etchant (i.e., HNO_3, 65 wt.%). The Ag layer was selectively etched away within 10 min without chemical dissolution of AAO replication master. The separated Au mesh remains floating on the surface of Ag etchant, while AAO membrane sinks into to solution. Finally, the Au membrane can be transferred onto Si surface, acting as mask in MACE for the fabrication of well-ordered SiNWs.

Metal mesh can be obtained on Si surface by combining nanosphere lithography and self-assembly of metal particles [94] or electroless plating of metal particles [95]. In self-assembly approach, Si surface loaded with array of poly(N-isopropyl-acrylamide) (polyNIPAM) microsphere was functionalized with 3-aminopropyltriethoxysilane by vapor deposition, and the sample was baked for 1 h at 80 °C. Afterwards, a gold particle solution (~15 nm diameter) was dropped onto the surface of sample and incubated for 20 minutes at 50 °C. The sample was rinsed and dried in a stream of N_2, and an Au mesh was formed on Si surface. The sample was etched in a HF/H_2O_2/ethanol (v/v/v = 1/1/1) etchant, resulting to SiNWs [94]. In electroless plating approach, Ag seeds were deposited onto Si surface patterned with polystyrene (PS) nanosphere using $AgNO_3$/HF solution, and then the sample was immersed into the solution containing $AgNO_3$, NH_4OH, CH_3COOH and NH_2NH_2 for the growth of compact silver mesh film.

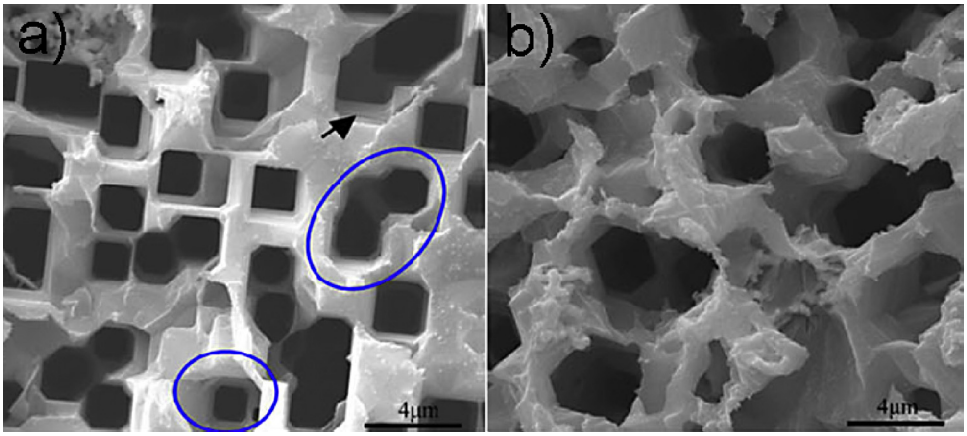

Fig. 16 Plan view SEM images of (a) Si(1 0 0) and (b) Si(1 1 1) resulted from MACE using Ag particles deposited from Ag mirror reaction. Reproduced with permission from Ref. [83]. Copyright 2011, The Minerals, Metals & Materials Society.

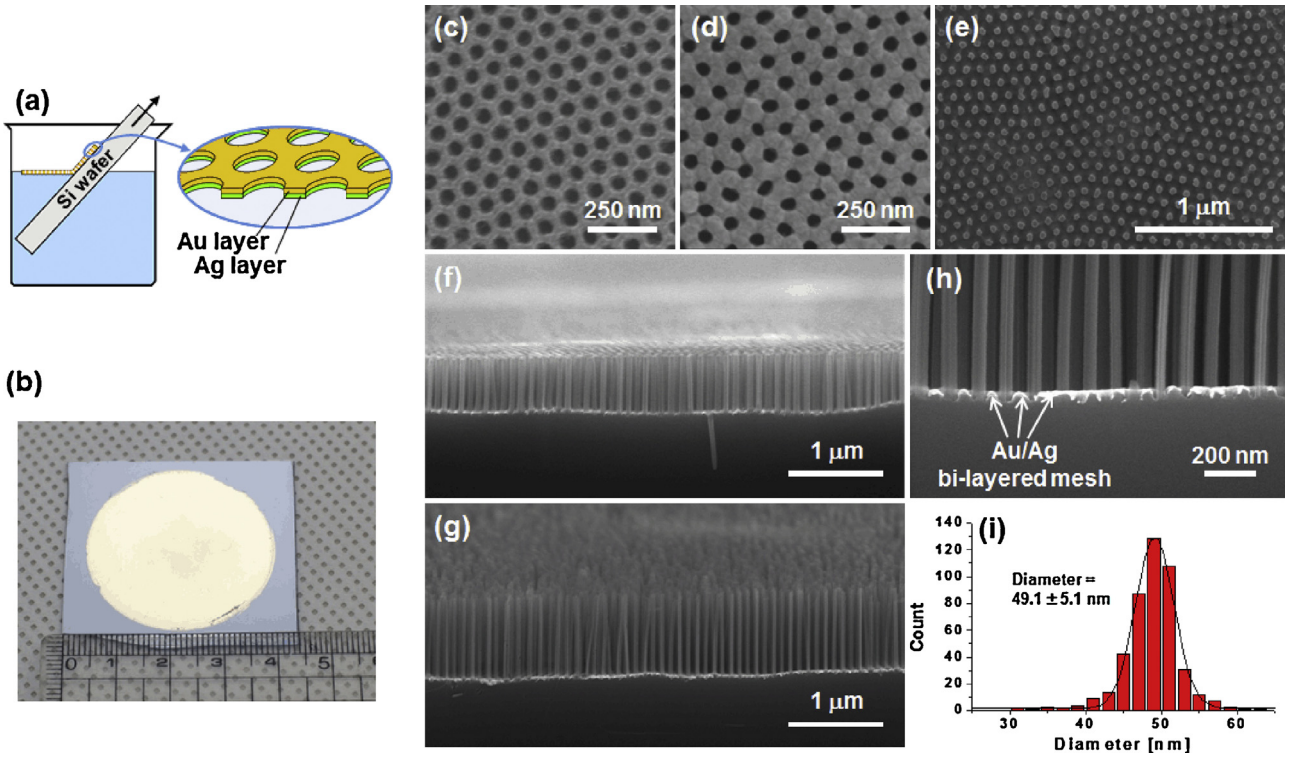

Fig. 17 (a) Schematic of transfer of floating Au/Ag bilayered metal mesh onto Si wafer. (b) A photograph of Au/Ag bilayered metal mesh on a Si(1 0 0) wafer. SEM micrographs of (c) AAO membrane and (d) Au/Ag bilayered metal mesh. (e) Typical plan-view SEM image of extended arrays of vertically aligned SiNWs obtained by MACE of Si(1 0 0) wafers by using Au/Ag bilayered metal mesh. (f and g) Cross-sectional SEM images of vertically etched Si(1 0 0) wafers, showing SiNWs with different diameters; (d) 63.9 ± 9.2 and (e) 39.5 ± 4.2 nm. (h) A magnified cross-sectional SEM image of a vertically etched Si(1 0 0) wafer taken near the etching front. (i) Histogram showing the diameter distribution of SiNWs shown in panel c, together with a Gaussian fit (solid line) of the measured statistical data. Reproduced with permission from Ref. [91]. Copyright 2011, American Chemical Society.

Afterwards, HF/H_2O_2 etchant was used to etch Si loaded with Ag mesh into SiNWs [95].

Optical properties of SiNWs formed by MACE

Bulk silicon has an indirect band gap, which is inherent obstacle for potential applications to light-emitting devices. However, since Canham has reported visible photoluminescence (PL) from mesoporous silicon wire at room temperature due to quantum size effect [96], nanostructured silicons such as porous SiNWs have extensively been investigated by many researchers. Most studies to date have devoted mainly to fundamental understanding of light emission of SiNWs, rather than to practical applications to light emitting devices. Although various mechanisms, including quantum confinement effect and surface state or defects in SiO_x, have been proposed, the origin of light emission is still under debate. Hence in this section, we mainly focus on PL properties of porous SiNWs to understand the light emission mechanism. For the preparation of SiNWs, MACE method is most widely utilized because of its facile controllability over porosity through etching conditions [11,31,32,47,97–106].

Hochbaum et al. and Qu et al. investigated separately investigate optical properties of porous SiNWs synthesized by MACE [31,32]. In both experiments, it was found that the porous SiNWs exhibited broad visible red emission centered at 680 nm and 650 nm under irradiation with 442 nm and 473 nm lasers, respectively, although they could not verify the origin of emission mechanism. Chern et al. performed detailed study on the effect of etching conditions such as etchant concentration, etching time, doping level and orientation of silicon on optical properties by combing nonlithographic patterning and MACE of silicon [11]. Light emission in the whole visible and near infrared range was observed in all samples regardless of etching conditions. However, solid vertical SiNWs (Fig. 18 a) and porous slanted SiNWs (Fig. 18b) that were prepared by different etchant concentrations exhibited stronger emission in the blue (~470 nm) and red (624 nm), respectively (Fig. 18c). SiNWs synthesized by longer etching time also showed blue emission. Further investigation on the morphology of SiNWs confirmed that porous SiNWs have milder height undulation, while solid ones exhibit nanoscale surface roughness. More interestingly, SiNWs with diameters of 1000 nm (upper panel) and 400 nm (lower panel) showed similar emission wavelength and intensity (Fig. 18d). This diameter range is well above the quantum confinement threshold (~5 nm). Thus authors claimed that the visible emission is most likely originated from surface morphology. Sivakov et al. also reported strong visible (red-orange) PL from both lightly doped and heavily doped SiNWs at room temperature [98]. The key

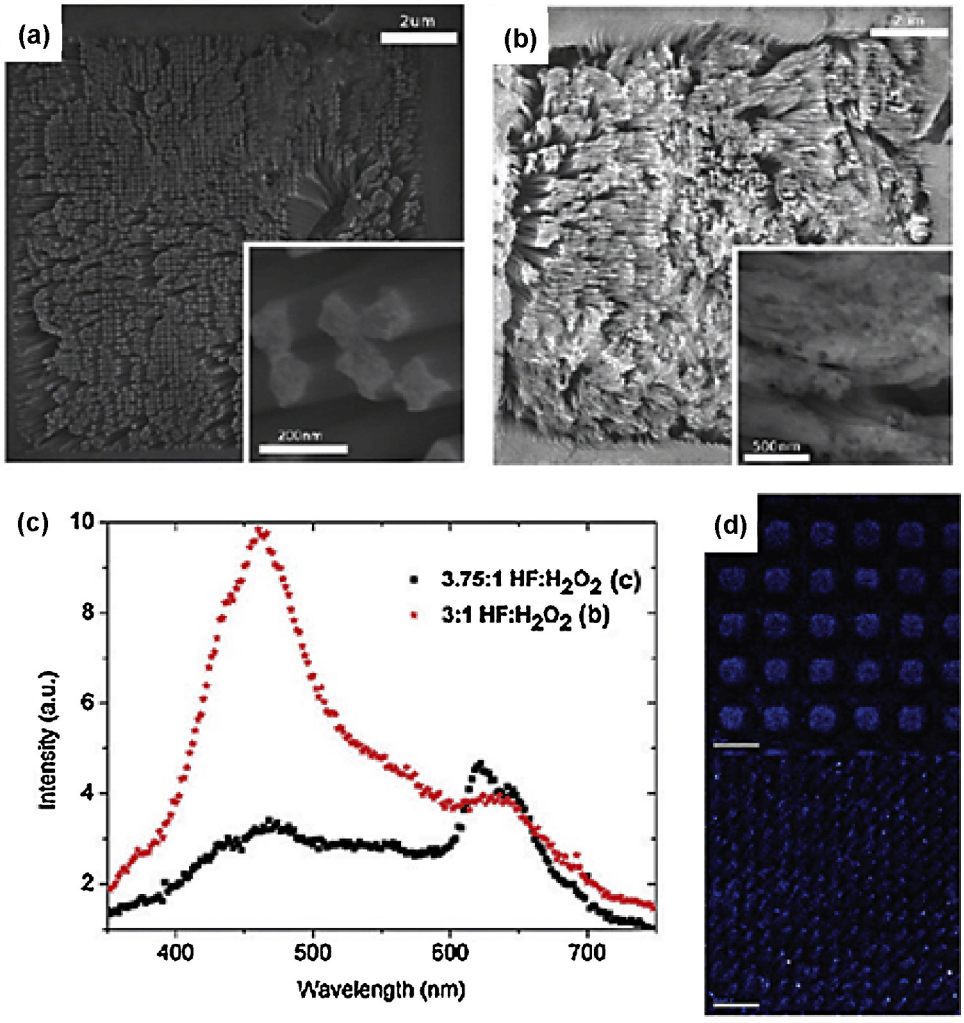

Fig. 18 Top-view SEM images of (a) solid vertical SiNWs and (b) porous slanted SiNWs with insets showing magnified images. (c) CL spectra obtained from solid vertical SiNWs (red squares) and porous slanted SiNWs (black squares). (d) Faux color CL images at a wavelength of 470 nm obtained from SiNWs with diameter of 1000 nm (upper) and 400 nm (lower), respectively. Scale bar is 2 μm. Reproduced with permission from [11]. Copyright 2010, The American Chemical Society.

experiment they conducted is comparative investigation on SiNW samples before and after HF treatment to disclose the effect of SiO_x-based interface state. According to optical characterization combined with TEM analysis, the quantum confinement effect due to periodic nanostructures at the rough sidewall appeared to be the most probable explanation of the PL rather than SiO_x-based interface states. Lin et al. also investigated the effect of morphology of SiNWs on optical property [99]. The intensity of PL peak was observed to increase and be shifted to red wavelength with increasing porosity. Moreover, the PL spectrum is decomposed into two peaks centered at 750 nm and 850 nm. From the Fourier transform infrared spectroscopy (FTIR) analysis, they confirmed that Si—O and Si—H_x bonds correspond to the PL peaks at 750 nm and 850 nm, respectively. This result indicates that two origins are involved in the light emission, i.e., the peak at 750 nm from surface-oxidized nanostructure, while the other peak at 850 nm from nanoporous structure. Similarly, Dawood et al. reported that strong PL from porous SiNWs is attributed to both quantum confinement effect in nanoparticles and oxide-related defects around the silicon nanocrystallites through the systematic investigation on optical and vibrational properties [100].

Apart from the reports above, some studies have focused on surface state [103,104]. Sun et al. investigated the effect of surface passivation on the PL property of SiNWs [103]. It is well known that dangling bonds on the surface of silicon can act as non-radiative centers, thus deteriorate the optical properties. The authors were able to passivate the silicon surface with oxygen by using aqueous HNO_3 solution and found that PL intensity is increased by 2 times compared to silver/hydrogen passivated SiNWs. Most recently, Zhang et al. reported considerable improvement of PL intensity by tuning nanostructure and surface treatment of SiNWs [106]. Increasing porosity and Si—O bonds on the surface of SiNWs resulted in increase of the light emission intensity. They found that oxidation of SiNWs causes red shift of PL peak and increase in PL intensity with decreasing temperature, which are contradictive with quantum confinement effect. Rather, they suggested that the origin of strong emission is mostly localized state associated with Si—O bonds and self-trapped excitations in the nanoporous structure.

Nanotechnology applications of SiNWs formed by MACE

During the last decade, enormous attention has been focused on the potential applications of SiNWs in the fields of energy conversion, energy storage, light emitting devices and sensors due to the peculiar electrical, optical and physicochemical properties compared to their bulk counterparts. For SiNWs-based energy conversion and storage applications, excellent review articles have recently been published [107,108]. Therefore, in this section, we limit our discussion to the SiNWs formed by MACE process and provide comprehensive discussion on their applications to solar and thermal energy conversion, Li-ion battery anode, supercapacitors, and sensors.

Solar energy conversion

Photovoltaic (PV) effect is a property of material generating electric power upon exposure to light. Silicon is most widely used PV materials in solar energy conversion industry due to the abundant reserve in earth, compatibility with industrial semiconductor technology and high stability. Current Si PV industry, however, is suffering from the requirement of expensive solar grade high-purity Si wafer due to the intrinsic limit of Si, i.e., indirect band gap and low light absorption efficiency. In order to lower the cell production cost and enhance energy conversion efficiency over traditional planar wafer-based solar cell devices, peoples are trying to utilize vertically aligned SiNWs because one dimensional (1D) geometry can provide several benefits such as broadband optical absorption by strong light trapping, large junction area, short diffusion distance of photo-generated charge carriers and defect tolerance [109—114]. Particularly, MACE of silicon has a merit of large scale preparation of SiNWs with low processing cost and temperature thus allows us to obtain further benefit in terms of practical applications of SiNWs to inexpensive solar cell device. Recently, Yuan et al. also emphasized the significance of SiNWs prepared by MACE in terms of superior solar cell performance over vapor—liquid—solid (VLS)-grown SiNWs [115]. Therefore, many researches are concentrated on solar cell based on chemically etched SiNWs. We categorized the recent reports on SiNWs based solar cell into p—n junction solar cell [57,116—126], Schottky junction solar cell [127—129], photoelectrochemical solar cell [130—134], and heterojucntion solar cell [53,72,135—142].

p—n junction SiNW solar cell

For forming p—n junction of SiNW arrays, dopant diffusion at high temperature (900 °C) or spin-on-dopant solution followed by high temperature annealing methods are typically used. First attempt to demonstrate p—n junction solar cell based on MACE-formed SiNW arrays was made by Peng et al. [116]. They found that light reflection can be considerably suppressed over wide spectral bandwidth by large surface area and subwavelength structure of dense SiNWs and porosity gradient along the axial direction of individual SiNW. Despite of the remarkable optical antireflection property of the prototype solar cell device, power conversion efficiency (PCE) was found to be 9.31%, which is not as high as expected. They attributed the poor device performance to the low current collection efficiency of grid front electrode and the increased interfacial carrier recombination. Garnett et al. also reported fabrication of radial core-shell p—n junction SiNW array based solar cell. Radial p—n junction was formed by depositing p-type amorphous Si through chemical vapor deposition (CVD) on n-type SiNWs prepared by chemical etching of n-type silicon, followed by crystallization through rapid thermal annealing. However, they obtained only 0.5% of PCE due to the high surface and interfacial recombination and high series resistance [117]. A number of defects and dangling bonds existing on the surface of SiNW synthesized by chemical etching method result in the enhanced surface carrier recombination velocity. Moreover, it is well known that porous surface of chemically etched SiNWs can lead to increased depletion region traps. Consequently, realization of good electrical contact and formation of surface and interface passivation are essential to improve the performance of SiNW-based solar cell. Fang and the co-workers fabricated a solar cell based on slantingly oriented SiNWs and achieved device performance superior to conventional nanowire-based solar cell with vertically oriented SiNWs [118]. Although the reflectance of slantingly aligned SiNW arrays was found to be higher than that of vertically aligned ones, current collection efficiency was considerably improved due to the better electrical contact originating from the compact top-surface morphology of slanting nanowires (Fig. 19a and b). PCE of the solar cell based on slantingly aligned SiNW array was 11.37% (Fig. 19c).

Most recently, effect of surface passivation on the reduction of carrier recombination has been investigated by depositing silicon oxide or silicon nitride layer on the SiNW surface [119,120]. Lin et al. have successfully demonstrated high performance SiNW-based solar cell through surface passivation by using the silicon oxide and silicon nitride (Fig. 19d) [119]. The excellent light trapping property of nanowire array was still maintained even after bilayer passivation. They measured the effective minority carrier lifetime to investigate effective surface recombination velocity upon different passivation layer. As shown in Fig. 19e, silicon oxide and nitride bilayer exhibited better passivation effect and reduction of carrier recombination velocity compared to individual layer because the hydrogen existing in silicon nitride can further passivate dislocations and dangling bonds. As a result, they were able to achieve the highest PCE of 17.11% from SiNW-based solar cell with bilayer passivation (Fig. 19f).

Another strategy for improving the performance of p—n junction solar cell is to modify alignment of nanowire arrays, for example, fabrication of well-ordered arrays of SiNWs on large area [57,121]. It was reported through theoretical studies that periodically aligned silicon nanostructure can suppress light reflection more efficiently than randomly oriented one [143]. Li et al. produced large area self-ordered arrays of SiNWs by combining polystyrene nanosphere lithography technique and MACE of silicon [57]. They found that reflection loss can be significantly reduced within wavelength range of 200—1000 nm, thus relatively high PCE can be obtained in the self-ordered arrays of SiNW-based solar cell without any further modifications such as surface

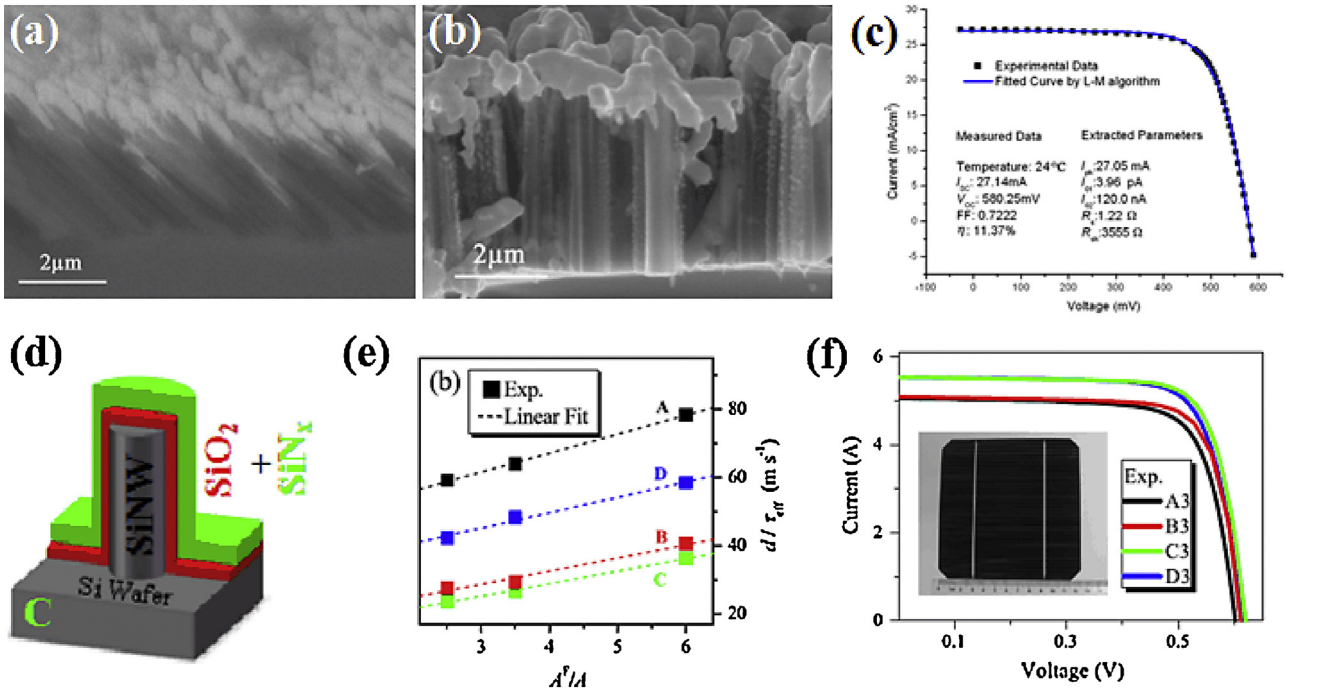

Fig. 19 SEM images of electrodes formed on (a) slanted SiNWs and (b) vertical SiNWs. (c) *I*—*V* curves of slanted SiNWs based solar cell. Reproduced with permissions from [118]. Copyright 2008, IOP Publishing Ltd. (d) Schematic illustrating SiNWs passivated with 10 nm SiO_2 and 60 nm SiN_x. (e) Measured d/τ_{eff} as a function of surface area enhancement ratio A^F/A, where d is wafer thickness, τ_{eff} is effective minority carrier lifetime, A^F is front surface area of SiNWs based wafer, and A is front surface area of textured Si wafer. A, B, C and D with different colors denote series of samples: A in black is bare SiNWs, B in red is SiNWs with SiO_2 layer, C in green is SiNWs with SiO_2 and SiN_x layers, and D in blue is SiNWs with SiN_x layer. The slope of each curve refers to local effective surface recombination velocity. (f) *I*—*V* curves of each sample with a photograph of sample C in inset. Reproduced with permission from [119]. Copyright 2013, IOP Publishing Ltd.

passivation. A new prototype SiNW-based solar cell, in which bulk p—n junction SiNWs and radial p—n junction SiMWs with tapered morphology, are co-integrated by optical pattering technique followed by MACE of silicon has been reported (Fig. 20a) [122]. Photograph in Fig. 20b shows 4-in. wafer with black color consisting of co-integrated SiNW arrays. The tapered morphology of SiNWs can reduce light reflection through multiple scattering and gradual transition of refractive index. Radial p—n junction of SiMWs also enhances effective diffusion length of carriers, resulting in the improved carrier collection efficiency. SiNW and Si microwire (SiMW) co-integrated solar cell exhibited the best device performance compared to each SiNW- and SiMW-based solar cell (Fig. 20c).

Schottky junction SiNW solar cell

Recent research on Schottky junction-based SiNWs solar cell has been focused on graphene/SiNWs array hybrid architecture due to its low-cost and simple processibility. In addition, graphene film can also provide several advantages such as high optical transmittance and good electrical conduction, thus can act not only as a flexible and transparent front electrode, but also as an active layer for photo-generated carrier separation and hole transport. Fan et al. demonstrated Schottky junction solar cell by assembling CVD grown multi-layered graphene film on vertical n-type SiNW arrays synthesized by MACE method [127]. Fig. 21a—c shows schematic and representative SEM images of SiNWs and graphene/SiNW Shottky junction, respectively. Semitransparent graphene film is conformally contacted with the underlying vertical SiNW arrays (Fig. 21c). Pristine graphene/SiNWs solar cell exhibited 1.25% of PCE, which is still higher value compared to graphene/planar silicon solar cell due to enhanced light trapping and carrier transport. With chloride doping method which led to p-type doping effect and enhanced sheet conductance of graphene film, PCE was improved to 2.86%. In analogy to the report above, Xie et al. also fabricated Schottky junction solar cell consisting of monolayer graphene and SiNW array and investigated the effect of nanowire length, doping type, and surface treatment on the cell performance [128]. Although longer nanowires are advantageous for light trapping, increased amount of surface defects caused severe carrier recombination. Thus optimization of wire length is necessary for the best device performance. N-doping on graphene film was found to increase graphene's conductivity, giving rise to effective carrier separation and transport. Through introducing graphene suspension to the interspace of SiNW arrays, it was observed that carrier separation and transport are effectively facilitated. Accordingly, by optimizing those device conditions, a maximum PCE of 2.15% was obtained.

Further, the authors conducted systematic investigation on even higher- efficiency graphene/SiNW array solar cell.

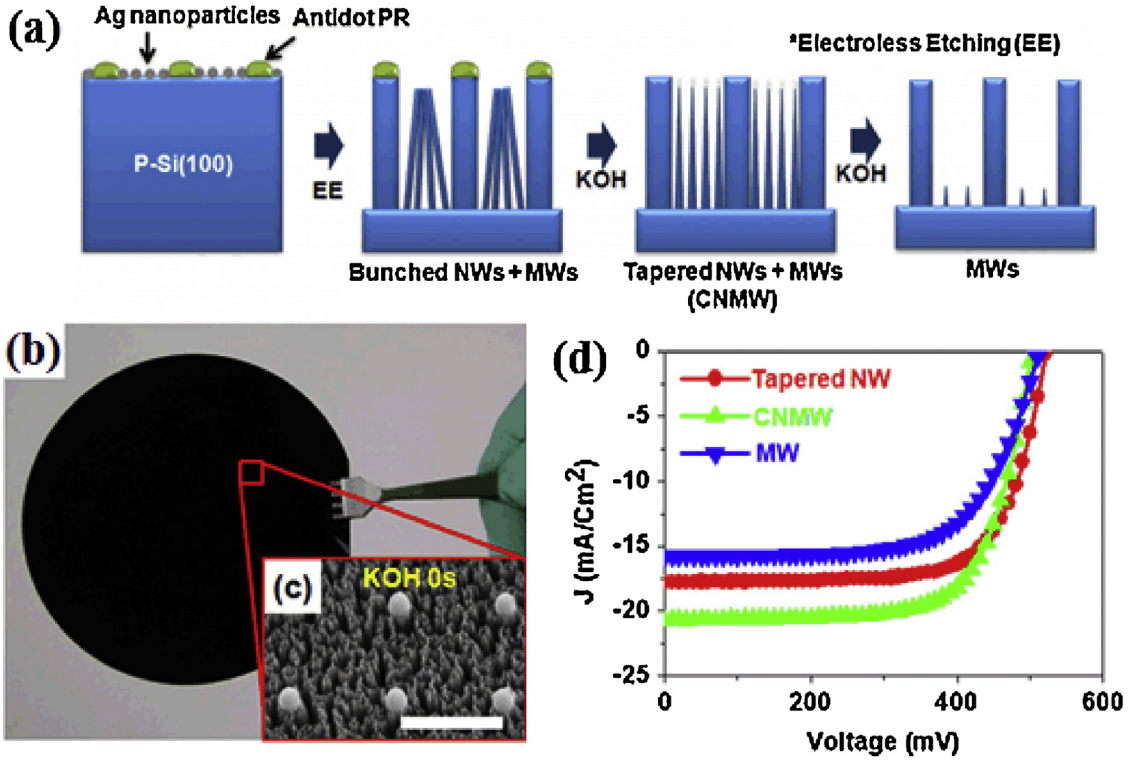

Fig. 20 (a) Scheme of fabrication procedure for tapered SiNWs and microwires (SiMWs) co-integrated structure. (b) Photograph of 4-in. wafer-scale SiNWs and SiMWs co-integrated structure and (c) corresponding SEM image. Scale bar is 50 μm. (d) *I*—*V* curves of tapered nanowire structure (red circles), co-integrated structure (green triangles), and microwire structure (blue inversed triangles). Reproduced with permission from [122]. Copyright 2010, IOP Publishing Ltd.

They found that doping level, number of graphene layer, together with proper surface modification for passivation and carrier separation can considerably improve energy conversion performance of graphene/SiNW Schottky junction solar cell [129]. Monolayer graphene has low electrical conductivity and work function (4.5—4.7 eV) which lead to low junction barrier with n-type silicon. With increasing number of graphene layer, conductivity and barrier height can be improved. They found that 4 layers of graphene exhibited the best performance because the transmittance severely reduced when number of graphene layers is higher than 5. Surface passivation by methyl group with Pt nanodots was found to cause strengthening of built-in electric field and surface energy band bending, thus effective carrier separation along radial direction of SiNW. In addition, by inserting proper electron blocking layer (in this study, P3HT conductive polymer) which contributes to prevent electrons transport from silicon to graphene, they were able to achieve maximum PCE of 8.71% (Fig. 21d and e).

Photoelectrochemical solar cell

As a viable alternative to the current high-cost solid-state junction solar cell, recently, photoelectrochemical (PEC) solar cell has emerged due to its merit of low cost liquid-state junction of semiconductor and high defect-tolerance. Liquid electrolyte contacts with SiNW surface, resulting in conformal charge-separating junction on large surface area and thus higher solar cell performance. In particular, metal-assisted chemically etched SiNW-based PEC solar cell can offer further cost-effectiveness. In 2008, Peng et al. demonstrated PEC solar cell consisting of vertical SiNW arrays, which exhibited remarkable photoactivity and photovoltaic property in redox electrolyte containing hydrobromic acid and bormine [130]. However, such PEC solar cell is still suffering not only from severe carrier recombination loss, poor carrier collection, but also from photocorrosion, and photooxidation of SiNW surface, which lead to poor device performance and degradation. Decoration of metallic-nanoparticle on sidewalls of nanowires is widely accepted method to enhance SiNW-based PEC solar cell [131—133].

Among the electrocatalytic metals, Pt is known to exhibit best solar energy conversion efficiency. In light of this, Peng et al. reported preparation of PEC solar cell based on SiNW arrays decorated with Pt nanoparticles (PtNPs) [131]. 5—10 nm-sized PtNPs were deposited on the surface of SiNWs through electroless metal deposition (EMD) (Fig. 22 a). PtNPs on the SiNWs considerably contributed to the enhancement of photoactivity and charge transfer rate from n-type silicon to metal. Thus, PCE of PtNP-decorated SiNWs was improved up to 8.1%, compared to naked SiNWs and Pt-decorated planar silicon. As shown in Fig. 22b and c, with increasing Pt-deposition time, PCE and photocurrent density increased until certain time, then gradually decreased. Large amount of Pt deposited on SiNWs tends to promote

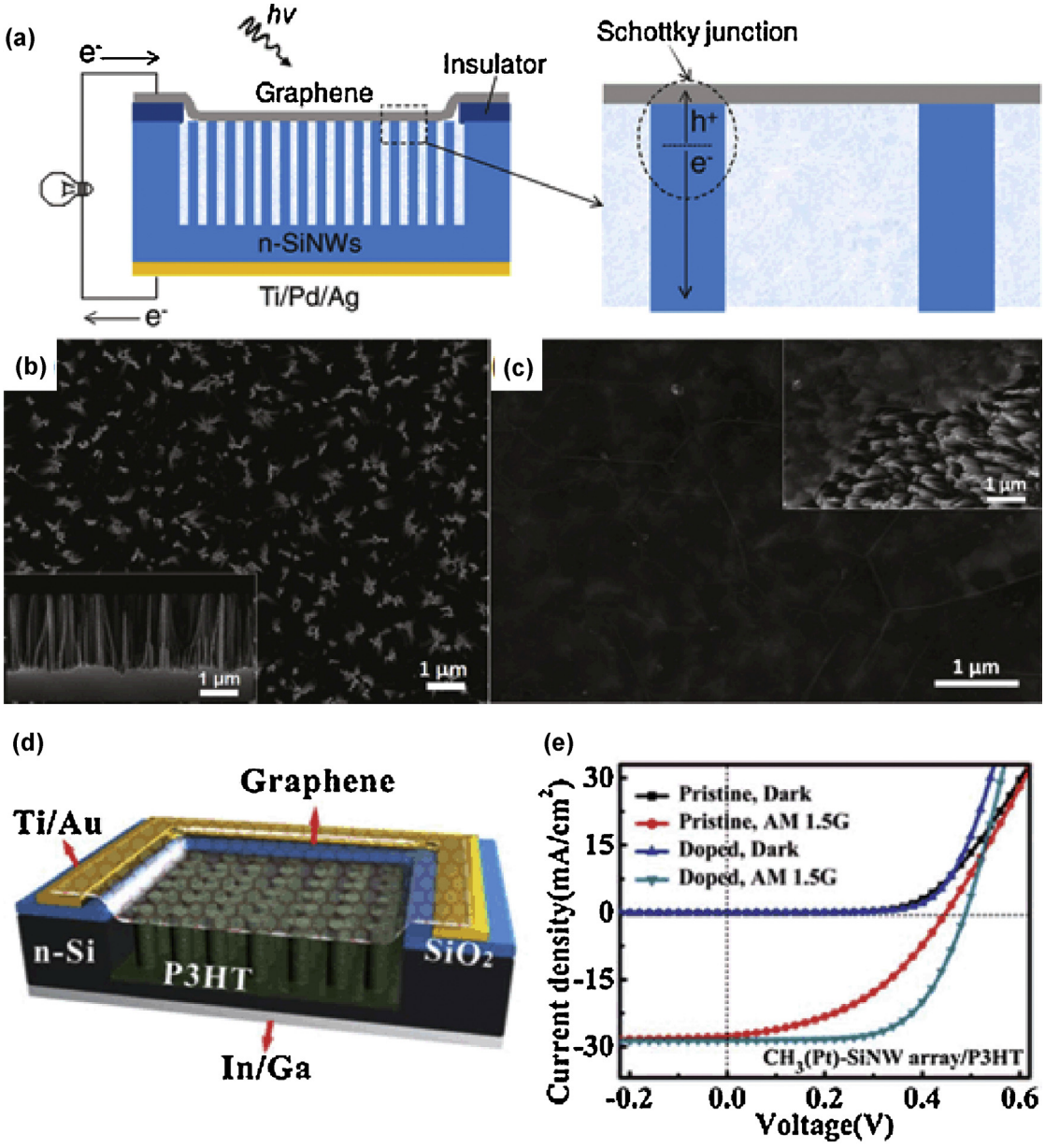

Fig. 21 (a) Schematics illustrating graphene/SiNWs Schottky solar cell with its enlarged image. (b) Top-view and cross-section view (inset) SEM images of as-prepared SiNWs. (c) Top-view SEM images of graphene/SiNWs junction. Reproduced with permissions from [127]. Copyright 2011, The American Chemical Society. (d) Schematic illustrating graphene/P3HT/SiNWs Schottky junction solar cell. (e) *I*—*V* curves of 4-layer graphene/P3HT/SiNWs before (black and red circles) and after (blue and green triangles) HNO_3 doping. Reproduced with permission from [129]. Copyright 2013, The Royal Society of Chemistry.

formation of porous silicon layer, which has a high resistance and degrades photoactivity. Long term stability of SiNWs in redox electrolyte is another important issue. Therefore, further improvement of device performance is possible by applying proper surface passivation or electrolyte to SiNW-based PEC solar cell. Shen et al. demonstrated remarkably stable methyl-terminated and Pt-decorated SiNW-based PEC solar cell utilizing ionic liquid electrolyte instead of corrosive HBr/Br_2 redox electrolyte [132]. It was found that combination of methyl group for effective passivation of dangling bonds and Pt nanoparticles for catalytic activity with ionic liquid electrolyte considerably contributed to stability and device performance of SiNW-based PEC solar cell. However, achieved PCE (6.0%) was still lower than that reported by Peng et al. [131]. Wang et al. reported a novel SiNW-based PEC composed of PtNPs/carbon/silicon core-shell nanowire arrays (PtNPs@C@SiNWs) (Fig. 22d) [133]. They claimed that PtNPs enhance interfacial charge transfer, thus give rise to high photocurrent under continuous light illumination in the heterostructured solar cell (Fig. 22e). The eco-friendly and chemically stable thin carbon layer was also able to effectively passivate the surface of SiNWs even in the corrosive HBr/Br_2 redox electrolyte. Fig. 22f shows the superior stability of PtNPs@C@SiNWs to the

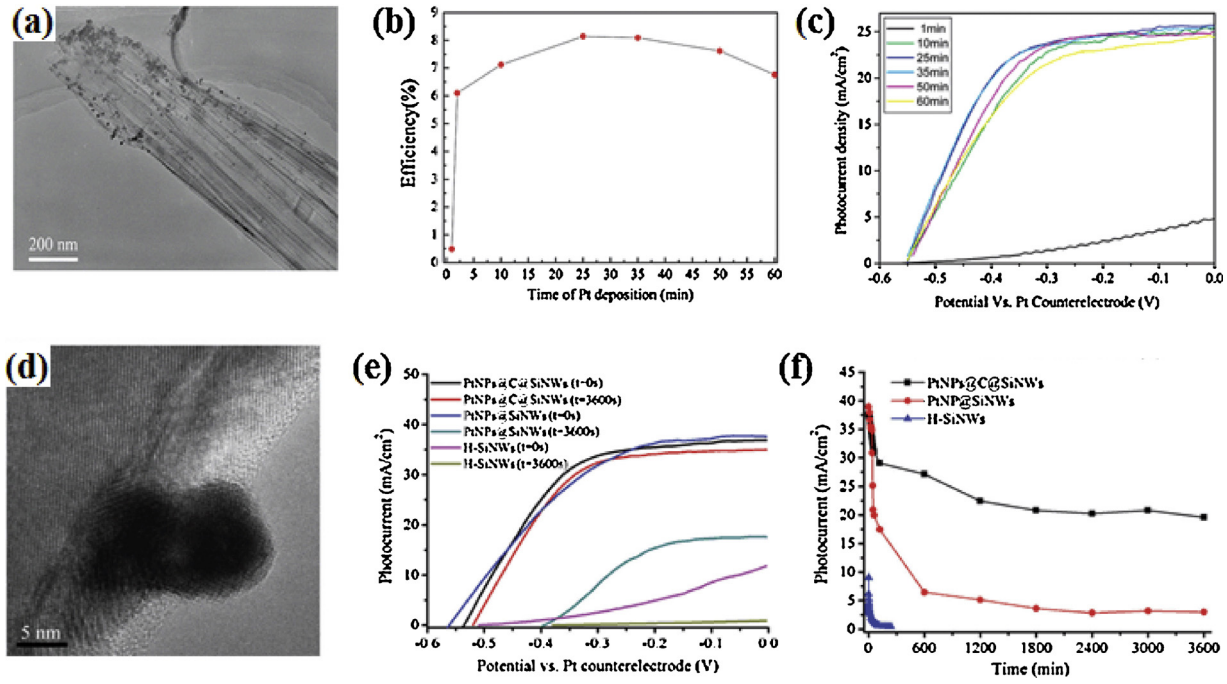

Fig. 22 (a) TEM image showing Pt nanoparticles-decorated n-SiNWs. (b) Solar energy conversion efficiency as a function of time for Pt-deposition. (c) *I*—*V* curves of PEC solar cells prepared with different deposition times of Pt nanoparticles. Reproduced with permission from [131]. Copyright 2009, The American Chemical Society. (d) HRTEM image showing Pt nanoparticles on C/SiNW. (e) *I*—*V* curves of H-SiNWs, Pt nanoparticles/SiNWs and Pt nanoparticles/C/SiNWs. (f) Photocurrent as a function of illumination time. Reproduced with permission from [133]. Copyright 2011, Wiley-VCH Verlag GmbH & Co. KGaA, Weinheim.

others. Consequently, PCE was significantly improved up to 10. 86%.

Organic—inorganic heterojunction solar cell

Organic-inorganic heterojuction can merge distinct advantages of light weight, low-temperature and low-cost process, and flexibility of organics as well as high carrier mobility and physical, mechanical stability of inorganics. High temperature treatment is known to cause degradation of silicon quality and carrier life time. This drawback can be avoided by using organics as a junction material. In particular, organic materials have a capability of conformal contact with inorganic one, providing uniform and large junction area. Consequently, much effort has been concentrated on the application of such hybrid system to photovoltaic devices with cost-effectiveness and mechanical flexibility. Cheng et al. fabricated p-type poly(9,9-diethylfluorene)/n-type SiNWs heterojunction structure and demonstrated good photovoltaic properties and sensitivities upon visible light illumination [135]. Since then, many researchers have extensively explored optimum organic-inorganic heterojunction structure in terms of efficient separation and collection of photo-generated carrier to improve solar energy conversion properties. It has also been reported that morphologies and surface passivation of nanowires are important factors for enhancing the efficiency through the increase of interfacial area, exciton separation, and improvement of stability for long operation lifetime of solar cells under atmospheric environment [138,144—148]. Uniform filling of the inter-space between densely formed nanowires with conjugated molecules becomes another critical issue. Conjugated molecules such as poly(3,4-ethylene dioxythiophene):poly-(styrenesulfonate) (PEDOT:PSS), poly(3-hexylthiophene) (P3HT) have been utilized as a conducting organic layer. Shiu et al. demonstrated polymer/SiNWs hybrid solar cell by coating hole-conducting PEDOT:PSS, whose highest occupied molecular orbital (HOMO) energy (~5.1 eV) is similar to valence band energy of silicon, resulting in good heterojunction for carrier separation and collection (see Fig. 23a and b) [148]. They found that such hybrid core-shell structures provided short carrier diffusion distance (several tens of nanometers or below), reduced series resistance and large junction area. Thus device performance was greatly improved (Fig. 23c). 2.78 μm-long SiNWs exhibited PCE of 5.09%. Further enhanced PCE was reported by Shen and coworkers [136]. In order to confirm complete coverage of nanowires with a conductive polymer thus high charge carrier extraction efficiency, the authors employed small conjugated molecule (spiro-OMeTAD) as a hole transport layer, instead of bulky polymer such as PEDOT:PSS. The thin organic layer was observed to significantly suppress charge recombination although pinhole area still exists on the surface which can cause current leakage. It was found that the presence of extra ~2 nm-thick copper and PEDOT:PSS on the SiNW/spiro-OMeTAD hybrid structure considerably enhanced carrier collection efficiency and electrode contact, resulting in PCE of 9.70%. Zhang et al. fabricated methyl-terminated SiNWs based heterojunction solar cell by using P3HT whose molecule size is relatively larger than that of spiro-OMeTAD, so it is hard to penetrate into bottom of the dense nanowire

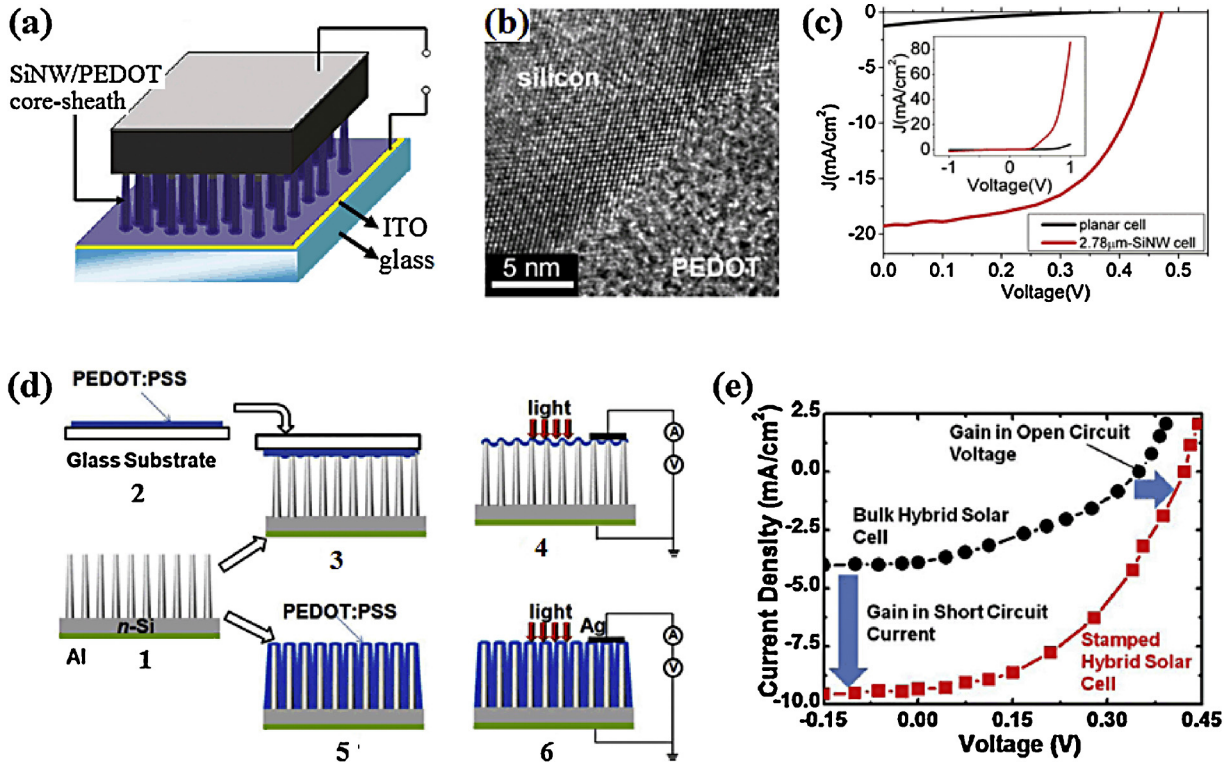

Fig. 23 (a) Schematic illustrating SiNW/PEDOT/ITO heterojunction solar cell. (b) HRTEM image of SiNW/PEDOT. (c) *I*—*V* curves of SiNW/PEDOT solar cell (red) and planar cell (black). Reproduced with permission from [148]. Copyright 2010, The American Chemical Society. (d) Scheme of fabrication procedure for PEDOT:PSS/SiNWs heterojucntion solar cell of two types: stamped (1—4) and bulk heterojunction solar cell (1—6). (e) *I*—*V* curves of stamped (red squares) and bulk (black circles) heterojunction solar cells. Reproduced with permission from [141]. Copyright 2012, IOP Publishing Ltd.

arrays [140]. The authors could reduce the density of nanowires by dipping the sample in PCl_5 solution, enabling complete coating of the nanowires. They also found that the thickness of P3HT plays a critical role for achieving the best device performance (the optimum thickness = 10 nm). By optimizing the device structures as discussed, PCE of 9.2% was obtained. Besides the core-shell type heterojuction solar cells, novel type of SiNWs/organic heterojuction device so-called stamped hybrid solar cell, where the conductive PEDOT:PSS thin film is contacting to the very top surface of nanowire arrays, was reported by Moiz et al. (Fig. 23d) [141]. The thin stamped channel can facilitate improvement of solar cell performance through several benefits such as improved carrier transport, reduced carrier recombination losses, lowered exciton decay losses as well as enhanced optical anti-reflection response. A few tens of nanometer-thick stamped channel is advantageous for efficient carrier transport and lowering bulk carrier recombination. Very small contact area between nanowire tips and thin polymer film greatly reduced probability of interfacial carrier recombination. Consequently, both open circuit voltage and short circuit current of stamped hybrid solar cell were considerably enhanced, compared to bulk junction hybrid solar cell (Fig. 23e). In 2013, 13.01% of PCE in PEDOT:PSS/SiNWs hybrid solar cell utilizing 1,1-bis[(di-4-tolylamino)phenyl]cyclohexane (TAPC) intermediate layer has been reported [149]. The authors attributed the highest PCE to the modified organic surface morphology and suppressed saturation current which improves the open-circuit voltage and fill factor. The TAPC layer was found to increase minority carrier life time and hinder oxidation reaction at the heterojunction interface.

Apart from the organic—norganic heterojuction solar cells, SiNWs/quantum dots (QDs) heterojunction solar cells are being under investigation [150,151]. QDs as a hole transport layer have advantages of tunable band gap, inherent stability and moderate charge mobility compared to typical organic semiconductors. Song et al. fabricated a radial PbS QDs/SiNWs heterojunction solar cell through solution phase technique [150]. They highlighted significance of QDs layer thickness and conformal coverage of nanowire surface for obtaining best performance. As a result of optimized radial junction, PCE of 6.53% was achieved owing to the enhanced light absorption and charge carrier extraction.

Despite of immense effort for realizing efficient SiNWs-based solar cells, achieved energy conversion efficiency to date is still much lower than theoretical value due to various origins such as the high defect density or recombination centers of photogenerated charge carriers on the surfaces of MACE-formed SiNWs. There is a specific trade-off in energy conversion efficiency in terms of nanowire dimension: longer SiNWs are advantageous for absorbing more photons, but charge traps and scattering centers may increase. Consequently, it is essential to optimize surface passivation, morphologies and dimension of nanowires for further enhancement of energy conversion efficiency.

Thermal energy conversion

Since the discovery of three reversible thermoelectric phenomena, i.e., Seebeck effect, Peltier effect, and Thomson effect, immense efforts have been devoted to utilization of those effects to thermal energy conversion devices which can particularly recover waste heat generated from various heating systems to useful energy source [152,153]. Enhancement of thermal energy conversion efficiency became one of critical issues in current energy technology [154—156]. Thermoelectric figure of merit is defined as $ZT = S^2\sigma T/\kappa$, where S, σ, and κ are Seebeck coefficient ($\Delta T/\Delta V$), electrical conductivity, and thermal conductivity, respectively. It is difficult to effectively increase ZT because such parameters of materials are interdependent. One-dimensional (1D) thermoelectric materials with nanoscale is one of most widely accepted strategies for increasing ZT because thermal conductivity is significantly reduced by enhanced phonon scattering at nanoscale interfaces, avoiding change in electrical conductivity of the material [157—159]. In this regard, SiNWs are currently attracting vast interest as a promising alternative to commercial thermoelectric materials such as bulk Bi_2Te_3. Particularly, many researchers are utilizing SiNWs prepared by MACE for realizing thermoelectric nanowire device [160—168].

Hochbaum et al. firstly demonstrated potential application of rough SiNWs synthesized by MACE method to high performance thermoelectrics (Fig. 24a) [160]. They found that surface of SiNWs prepared by MACE is much rougher than those grown by VLS method. High surface roughness of SiNWs considerably contributed to surface scattering of phonon, thus resulted in five- to eight-fold reduction of κ compared to VLS-grown SiNWs (Fig. 24b). Power factor ($S^2\sigma$) and calculated ZT were found to be highest near room temperature and decrease with temperature (Fig. 24c). Seebeck coefficient and electrical conductivity of SiNWs were almost same with bulk counterpart. However, ZT value of SiNWs (~0.6) is two orders of magnitude higher than that of bulk silicon due to the significantly reduced thermal conductivity. Therefore, they concluded that scattering of phonons not only by dopants, dimensional confinement, but also by nanoscale surface roughness can greatly reduce thermal conductivity, maintaining electrical conductivity of SiNWs. Given the significance that surface roughness decreases the thermal conductivity of materials, thorough understanding on phonon-surface roughness correlation should be preceded through quantitative analysis on surface roughness effect. By employing spectral techniques combined with high-resolution TEM imaging, Lim et al. have experimentally shown that broadband spectrum of phonons can cause frequency dependent scattering through interaction with roughened surface of SiNWs, thus resulting in the reduced thermal conductivity [162]. For generating roughened surface, VLS-grown SiNWs with smooth surface were treated in controlled manner by MACE method. The intrinsic SiNWs allowed them to eliminate impurity effect on phonon scattering. Three independent roughness parameters, root-mean-square roughness, correlation length, and power spectra were extracted from surface profile, then thermal conductivity (κ) was measured. It was found that such parameters have more significance on the thermal conductivity than nanowire dimension. Power spectra of roughness obtained from power law in the wavelength range of 1—100 nm may correlate well with thermal conductivity reduction.

Previous reports on the characterization of thermoelectric property were mostly based on single SiNW. Weisse et al. measured thermal conductivity (κ) of vertically aligned SiNW arrays by using nanosecond transient thermoreflectance (TTR), averaging out an inherent thermoelectric property variation which can be caused by difference in dimension, doping and porosity of individual SiNW within the same batch [164]. Fig. 24 d and e shows a scheme of vertical SiNW arrays with Cu top layer for thermoreflectance measurement and the corresponding SEM image. From TTR measurement of SiNW arrays with different levels of internal porosity, surface roughness, diameter and doping level, it was found that thermal conductivity (κ) can be reduced by phonon scattering only at internal pore interface when diameter of SiNW is larger than phonon mean free path, while by phonon scattering both at internal pore interface and at external rough surface when smaller than phonon mean free path (Fig. 24 f and g). Feser et al. also investigated thermal transport properties of SiNW arrays with controlled roughness by using time domain thermoreflectance (TDTR) measurement and Raman spectroscopy [166]. They claimed that reduction of thermal conductivity (κ) in SiNWs with large roughness is mainly originated from microstructural changes which have influence on both optical and acoustic phonons.

Unlike previous strategies for improving ZT i.e., thermal conductivity reduction by increasing phonon scattering at rough surface and interface, there has been an attempt to increase electrical conductivity (σ) by chemical modification of SiNWs surfaces, while maintaining thermal conductivity (κ). Li et al. demonstrated increase of electrical conductivity (σ) of n-type SiNW arrays by ammonia adsorption on the surface, leading to enhancement of ZT. On the other hand, p-type SiNW arrays exhibited decreased electrical conductivity and ZT [165]. They explained this phenomenon in terms of change in electron trap density upon ammonia exposure. It is well-known that absorbed ammonia molecules supply additional electrons, resulting in the lowered energy band bending at Si/SiO_2 interface and thus increase of the electrical current in n-type SiNWs and the opposite in p-type SiNWs. From noise measurement, they concluded that the electron traps existing in the native SiO_2 are neutralized by donated electrons from ammonia molecules.

As discussed above, most previous studies have directed mainly to characterizing basic themoelectric properties of SiNWs. However, practical application of MACE-formed SiNWs to thermoelectric devices requires further enhancement of energy conversion efficiency by optimizing size, doping level, and morphology of nanowires. At the same time, it is also required to develop reliable methods for integrating serial array of p- and n-type SiNW bundles with the top and bottom electrodes, maintaining the air-gap between vertically aligned individual SiNWs over technologically relevant scale.

Energy storage

Currently, most popular power source for wide spectrum of portable consumer electronics, implantable medical

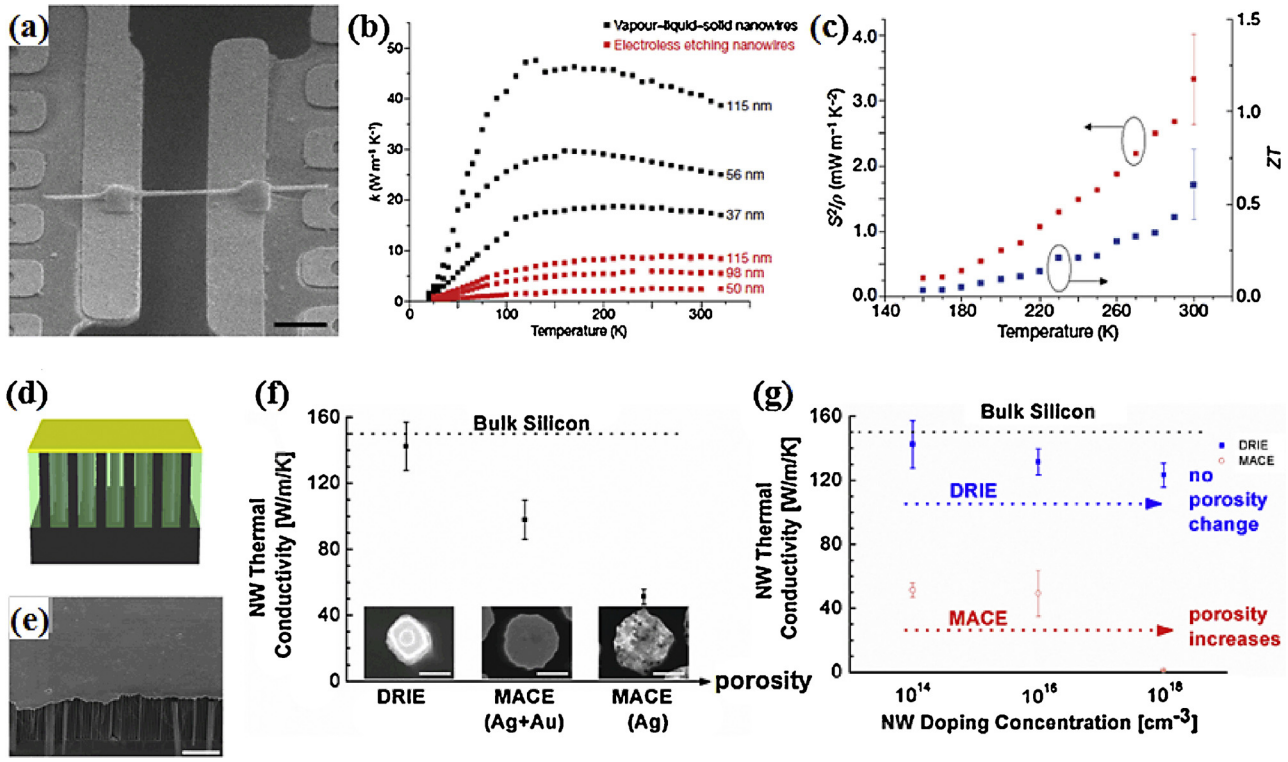

Fig. 24 (a) Tilted view SEM image showing SiNW contacting to Pt pads. Scale bar is 2 μm. (b) Temperature dependent thermal conductivities of SiNWs prepared by vapour—liquid—solid method (black squares) and metal-assisted chemical etching method (red squares) with different diameters. (c) Temperature dependence of power factor (red squares) and calculated ZT (blue squares) of single SiNW with a diameter of 52 nm. Reproduced with permission from [160]. Copyright 2007, Nature Publishing Group. (d) Schematic and (e) SEM image of metal film deposited on surface of SiNWs embedded in parylene matrix. (f) Thermal conductivities of SiNWs with different level of porosity. Insets are top-view SEM images of SiNWs prepared by DRIE, MaCE with Ag + Au and MaCE with Ag. Scale bar is 200 nm. (g) Thermal conductivities as a function of doping concentration of porous and nonporous SiNWs. Reproduced with permission from [164]. Copyright 2012, Springer.

appliances, electric vehicles and even aerospace applications is rechargeable lithium-ion batteries because of its relatively high energy storage capacity, and long life cycles. Conventional Li-ion battery is composed of carbon-based negative electrode (anode), lithium oxide-layered structure-based positive electrode (cathode) and non-aqueous liquid electrolyte. Due to the intrinsic limit of conventional Li-ion battery such as diffusivity of Li-ion in solid state or low energy density of electrodes, nanostructured materials are attracting much attention for overcoming such limits [169—172]. Particularly, as an alternative to graphite anode which has only capacity of 370 mAh/g, silicon-based anode is becoming an attractive choice due to its high gravimetric capacity of 4200 mAh/g theoretically calculated with fully lithiated $Li_{4.4}Si$ alloy and low discharge voltage (~0.4 V for delithiation) [173—175]. However, such large amount of lithium intercalated into silicon can accompany undesirable enormous volume expansion (almost 400% change upon lithiation) and phase transformation from single crystalline to amorphous phase, giving rise to significant degradation of device performance and poor reversibility [173,176]. To address this issue, silicon nanostructure-based anode has been extensively investigated because the small-sized geometry can effectively accommodate the large mechanical strain [177—180]. Among the nanostructured silicon, SiNWs can provide additional benefits such as short distance for lithium ion diffusion transport, efficient current collection, and high surface area contacting to electrolyte for lithium ion flux. Combined with MACE of silicon which enables one to obtain a rough and porous surface hence better accommodation of large volume expansion, SiNWs are being widely explored as a high performance anode [181—189].

Peng et al. first utilized SiNWs prepared by MACE as an anode material for Li-ion batteries [181]. They demonstrated larger charge capacity and longer cycling performance of such anode stemming from the good conductivity and nanoscale rough surface of SiNWs. However, the residual silicon wafer after forming SiNWs could contribute to the capacity of anode during lithium alloying and dealloying. In this regard, Huang et al. fabricated 90 μm-long SiNW-based anode by completely etching the single-crystalline silicon wafer to exclude contribution of residual wafer after chemical etching [182,184]. This geometry of anode does not require any binders or conducting additives. In addition, they coated carbon [182] and aluminum [184] films on the resulting sample by pyrolyzing carbon aerogel and thermal evaporation, followed by thermal annealing, respectively for enhancement of electronic conduction and better accommodation of volume change

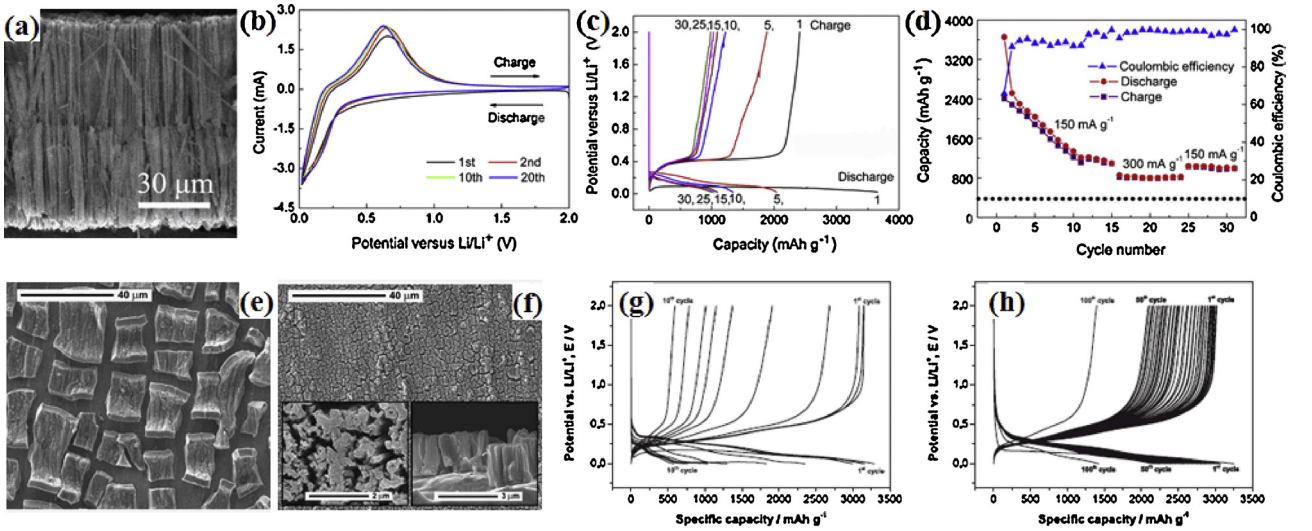

Fig. 25 Cross-section view SEM image of SiNWs electrode. (b) Cyclic voltammogram from 2.0 to 0.002 V at a scan rate of 1 mV/s, (c) galvanostatic discharge/charge curves at a current density of 150 mA/g between 1 and 0.02 V, and (d) capacity and Coulombic efficiency as a function of cycle number of the resulting SiNWs electrode. Reproduced with permission from [184]. Copyright 2010, Elsevier. SEM images showing morphologies of (e) pristine Si thin film and (f) bundle-type SiNWs after 5th cycle of charge/discharge test. Insets in (f) are magnified top- and cross-section views of the resulting SiNWs. Voltage profiles versus capacity of (g) pristine Si thin film during 10 cycles and (h) SiNWs during first 50 cycles and 100th cycle. Reproduced with permission from [188]. Copyright 2012, Elsevier.

(Fig. 25 a). Consequently, the anodes exhibited remarkable lithium storage capacity, Coulombic efficiency and cycling performance. Fig. 25b-d shows cyclic voltammogram, voltage profiles of galvanostatic charge/discharge and cycling behavior with Coulombic efficiency of Al-coated SiNWs, respectively which indicate redox reaction of silicon and lithium forming Li-Si alloy, high first discharge and charge capacities, and reversible capacity remained stable after 30 cycles. Similar to the Refs. [182,184], Qiu et al. fabricated NiO-coated SiNW array electrode and evaluated its battery performances in comparison with NiO nanostructured film [185]. In this hybrid nanostructure, NiO functions as an active material for storing and releasing lithium ions, while crystalline silicon only as an electrical conducting path as well as mechanically rigid support. Authors could eliminate the contribution of residual silicon wafer to reaction with lithium by adjusting potential ranging from 0.15 to 3.0 V which is beyond the limit of silicon-lithium reaction (~0.12 V). It is known that NiO exhibits sever degradation of capacity due to poor electronic conductivity. This drawback could be overcome in NiO/SiNWs hybrid structure. Moreover, NiO nanoparticles can decrease ion diffusion path and also increase the surface area for ion flux. Consequently, large lithium storage capacity, high Coulombic efficiency and cycling stability could be achieved. On the other hand, a novel approach to roll out Li-ion battery components from silicon chips through a continuous and repeatable etch-infiltrate-peel cycle has been reported [71]. By embedding MACE-SiNWs in the polymer matrix which acts as a gel-electrolyte and a physical separator, the authors could obtain a polymer-SiNW composite, which is readily peeled off in the form of a flexible and freestanding membrane. Porous Cu-nanoshell is conformally deposited on SiNW surfaces to form electrical interconnection, which enables not only to stabilize electrode over extended cycles, but also to provide efficient current collection. Accordingly, the SiNW-core/Cu-shell structure showed improved electrochemical performance due to high current collection efficiency and Si encapsulation.

For the preparation of direct contact between SiNWs and current collector, Nguyen et al. developed a novel method [188]. They first deposited 1.6 μm-thick silicon film on copper foil by CVD, then carried out MACE of the silicon film, resulting in the SiNW bundles on copper current collector. For the comparative investigation on the morphology effect between film and bundle, they also prepared silicon film counterpart. Compared to silicon thin film on copper, SiNW bundles showed better electrochemical performance. It was observed that silicon film was significantly damaged and delaminated from underlying copper after 5 cycles of charge/discharge test (Fig. 25e), while SiNW bundles was remained stable (Fig. 25f) due to the effective release of stress. The contact between SiNWs and copper current collector was maintained even after 100 cycles. As a result, the bundle type sample showed remarkable improvement of cycling performance compared to the film type sample (Fig. 25g and h).

Several routes for enhancing cell performance, for example, adding graphene or graphite as a conductive additive [183,186] or functionalization of SiNW surfaces [187] are still under intensive investigation. In Ref. [186], Wang et al. reported that introducing graphene nanosheet can considerably enhance charge capacity of porous SiNWs electrode compared to porous SiNWs/carbon black composite or commercial graphite, which is attributed to favorable charge transport feature of both graphene and one-dimensional nanostructure of silicon. Xu and co-workers demonstrated surface termination of silicon plays an important role in

maintaining reversibility, which is related to the solid electrolyte interphase (SEI) layer on the silicon surface during charge/discharge [187]. Most recently, Ge et al. reported experimental and theoretical studies on the effect of porosity on cycling performance of Li-ion batteries [189]. They found through simulation coupling lithium ion diffusion and strain induced by lithium intercalation that high porosity and large pore size of SiNWs would effectively facilitate stabilization of the structure during charge/discharge. For verifying the theoretical expectation, they fabricated porous SiNWs by MACE of silicon and evaluated their electrochemical performance. The capacity maintained above 2000, 1600, and 1100 mAh/g at current rates of 2, 4, and 18 A/g even after 250 cycles, which demonstrates excellent structural stability and long cycle life as an anode material due to the high porosity and electron conductivity of SiNWs (Fig. 25).

Besides the Li-ion batteries, electrochemical capacitor for energy storage has been considered another potential application of SiNWs [190—192]. Among the electrochemical capacitor electrode nanomaterials, nanostructured NiO is known to have an excellent electrochemical properties [193,194]. However, low specific surface area and poor electrical conductivity is the critical limitation. In light of this, hybrid nanostructured materials based on NiO are considered as promising alternative. Tao et al. investigated electrochemical behavior of NiO/SiNWs composite thin film for application to electrochemical capacitor electrode [190]. From the cyclic voltammetry and electrochemical impedance spectroscopy analysis, they observed that the maximum specific capacitance is as high as 681 F/g and capacity loss is only 3% even after 1000 charge/discharge cycles in the NiO/SiNWs composite electrode. This remarkable performance is attributed to high surface-to-volume ratio and surface activity. Unlike NiO/SiNWs composite form, Lu et al. fabricated vertically aligned NiO coated SiNW arrays [191]. Such geometry provides more active sites per unit area as well as good electrical conductivity, thus enables one to achieve high specific capacity (787.5 F/g), good cycle stability (4.039% of capacity loss after 500 cycles) and low internal resistance ($\sim$3.067 Ω).

In realizing SiNWs-based Li-ion battery with long life cycle, one of the most critical issues is to form a stable solid-electrolyte-interface (SEI) layer. The SEI layer should be dense, ionically conducting, but electronically insulating. Controlled formation of SEI layer on the surface of MACE-formed SiNWs is becoming an important issue, along with thorough understanding of the underlying formation mechanism. On the other hand, each SiNW should be electrically connected to the current collector to contribute to the capacity. The existing processes for the fabrication of current collector need to be further improved for the enhancement of capacity.

Sensors

Since one-dimensional geometry provides distinct advantages such as high surface-to-volume ratio and unique charge transport properties, potential application of nanowires to either chemical or biological sensing devices has attracted huge attention [195,196]. Individual nanowire can act as a charge accumulation and depletion site, inducing large change in the electrical properties by chemical or biological species. Particularly, biocompatibility and surface-tailoring capability of silicon enable one to utilize SiNWs for developing highly sensitive, selective and stable sensing devices. In this section, recent advancement of SiNWs based sensing applications is briefly reviewed by categorizing into chemical [195,197—201] and bio sensors [196,202—208]. Particularly for bio sensors, surface-enhanced Raman scattering (SERS)-based sensing is reviewed.

Although sensing performance of SiNWs has been intensively investigated with nanowires lying parallel to the underlying substrate [209—212], further enhancement can be realized by utilizing vertically aligned arrays. Peng et al. demonstrated first gas sensing properties of porous n-type SiNWs fabricated by MACE [197]. Two gold electrodes were deposited on top surface of SiNW arrays, and the resulting sample was exposed to gaseous NO_x with various concentrations ranging from 500 ppb to 100 ppm with recording the resistance change. They suggested that NO_x molecules donate electrons to n-type SiNWs, thus electrical conductivity increases upon NO_x exposure. Despite of the first demonstration of SiNWs based sensor, uniform electrical connection to top of whole nanowire arrays should be confirmed for obtaining higher sensitivity and stability. To address this, In et al. fabricated porous top electrodes deposited on top surface of vertical SiNW arrays by employing two separate nanosphere lithography steps, i.e., first step for fabricating SiNWs and second step for forming porous top electrode (Fig. 26a and b) [199]. The resulting periodically porous gold top electrode was found to well contact to the very tips of SiNWs and allowed gas molecules to access easily to surface of SiNWs, thus sensing performance considerably increased compared to the counterpart with continuous top electrode (Fig. 26c). As a novel nanostructured sensing device for detecting H_2, Noh et al. fabricated Pd-coated rough SiNWs based sensor [201]. Given Pd deposition on as-prepared SiNW arrays of which surface morphology is locally clustered and even slanted, inversely tapered shape is realized where the very top regions of SiNWs are thickly covered with Pd, thus can be locally connected each other (Fig. 26d). Upon H_2 exposure, volume expansion of Pd occurs, and local bridge for electrical current flow is formed through contact of Pd particles on tips of neighboring SiNWs. The detection limit was 5 ppm with 6% of sensitivity (Fig. 26e). The sensitivity increased with increasing H_2 concentration (Fig. 26f).

Surface-enhanced Raman Scattering (SERS) is one of most intensively utilized techniques for sensing single molecules [213]. However, it is difficult to realize such nanostructure in which nanogaps of less than 10 nm are formed on large area with current nanotechnology. In this context, peoples are trying to use SiNWs as a SERS substrate for forming SERS-active materials with nanogap in a simple and reproducible way. Typical SERS-active materials are silver or gold nanoparticles. Qiu et al. fabricated Ag-capped SiNWs for investigating SERS performance by using aqueous rhodamine 6G (R6G) [202]. They found that the length of SiNWs has an influence on the SERS intensity: higher SERS intensity for shorter SiNWs due to the rigid nature of individual nanowire. Long nanowires were observed to be likely to bend and

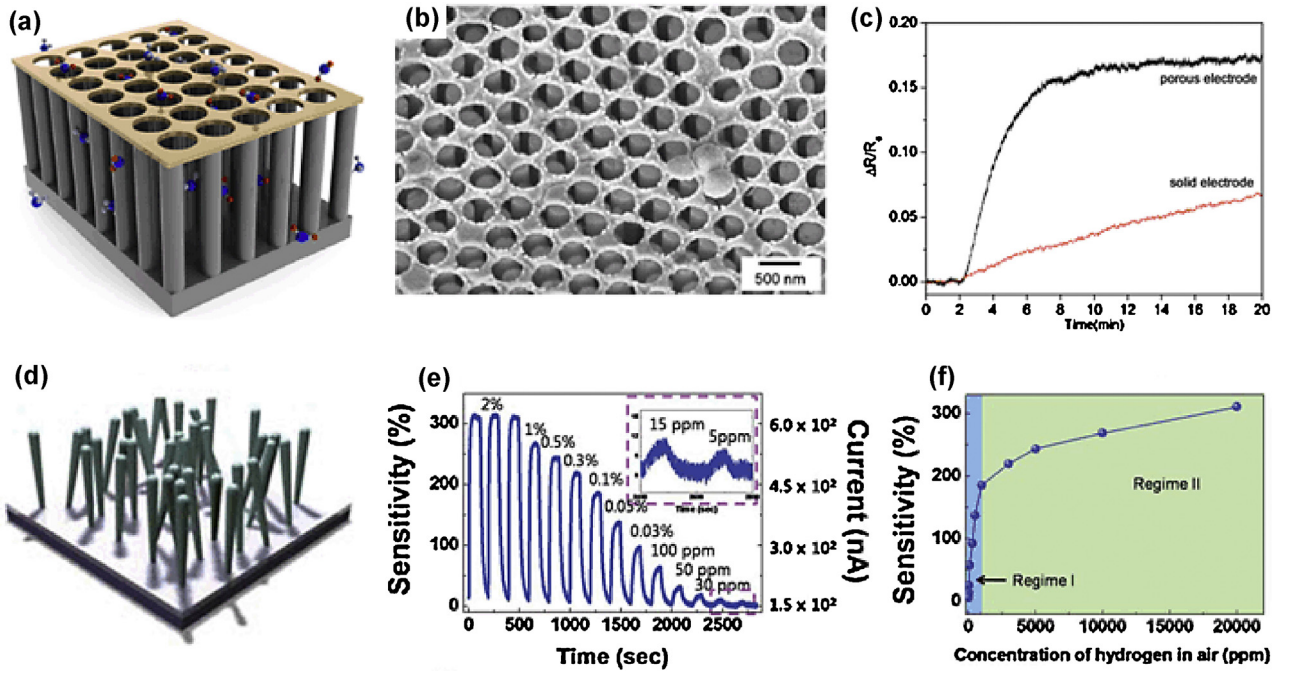

Fig. 26 (a) Schematic illustrating periodically porous top electrode formed on SiNWs and (b) SEM image of the corresponding sample. (c) Resistance profiles of SiNWs with porous top electrode (black line) and solid top electrode (red line) upon exposure to 500 ppb of NH_3. Reproduced with permission from [199]. Copyright 2011, IOP Publishing Ltd. (d) Schematic illustrating Pd thin film coated SiNWs. (e) Electrical response curve of the resulting sample upon exposure to H_2 with various concentrations. (f) A plot of sensitivity as a function of H_2 concentration. Reproduced with permission from [201]. Copyright 2011, The Royal Society of Chemistry.

agglomerate, thus lead to lower SERS intensity. They demonstrated a potential application of SiNWs to SERS-based bio sensor.

Zhang et al. demonstrated highly sensitive label-free immunoassay based on SERS by using Ag-coated SiNWs (Fig. 27a and b) [204]. The SiNWs-based SERS substrate exhibited ultrahigh detection limit for immune reactions. Immunocomplex formed with 4 ng of mouse immunoglobulin G (mIgG) and goat-anti-mouse immunoglobulin G (gamIgG) on the substrate gave distinguishable Raman bands with shifted positions and changed intensities (Fig. 27c). The authors attributed the enhancement of Raman signal to electromagnetic effect related to the dipolar resonance on metal surface and chemical effect associated with chemical reaction between molecules and metal. B. Zhang et al. reported comprehensive research on Ag-coated SiNWs for SERS based bio sensor (Fig. 27d), including optimization of experimental parameters for highly sensitive SERS-active Ag-coated SiNWs, SERS performance in terms of enhancement ability, stability and reproducibility, and finally detection of calcium dipicolinate (CaDPA) which is a molecule related to human health and safety [205]. As-prepared SiNWs were modified with 3-aminopropyltrimethoxysilane (APTMS) for depositing Au nanoparticles on the surface. After that, silver was coated on the resulting sample through plating solution (Fig. 27d). The morphology of SiNWs, controlled by etching time and temperature, and silver-plating solution were found to play key role in determining the magnitude of SERS signal enhancement and the sensitivity of detection. Ag-coated SiNWs prepared by optimized conditions exhibited 2—8 times stronger SERS intensity than Ag island film on planar silicon or ordered Ag-coated colloidal silicon film and stability for at least a 16-day period. In addition, SERS spectra collected on the randomly selected 23 places of resulting sample confirmed reproducibility. Lastly, authors demonstrated detection of 4×10^{-6} M CaDPA with a rapid data acquisition time (10 s) (Fig. 27e), revealing that the SERS based sensor prepared by Ag-coated SiNWs is suitable for detecting Bacillus anthracis spores. Most recently, Huang et al. demonstrated ultrasensitive single-molecule detection with high selectivity by utilizing nanogap-free SERS system, in which silver is coated on the surface of hexagonally packed SiNWs [214]. While SERS system with nanogap as hot spots suffers from reproducibility of biomolecule detection due to the confined electric field in small nanogap, such nanogap-free SERS system detected long double-strand DNA with 14% of relative standard deviation (RSD) for measurement more than 4000 spots over $200 \times 200\ \mu m^2$. The authors ascribed such high reproducibility to long interdistance between the nanowires (~150 nm) and continuous Ag coating on SiNW surfaces. The large interwire space allows large biomolecules to access to the surface. Surface plasmon can propagate along the continuous Ag layer, resulting in the 600 nm wide-range electric field.

Closing remarks and outlook

Recent developments in MACE of Si and applications of the resulting Si nanostructure have been summarized in this

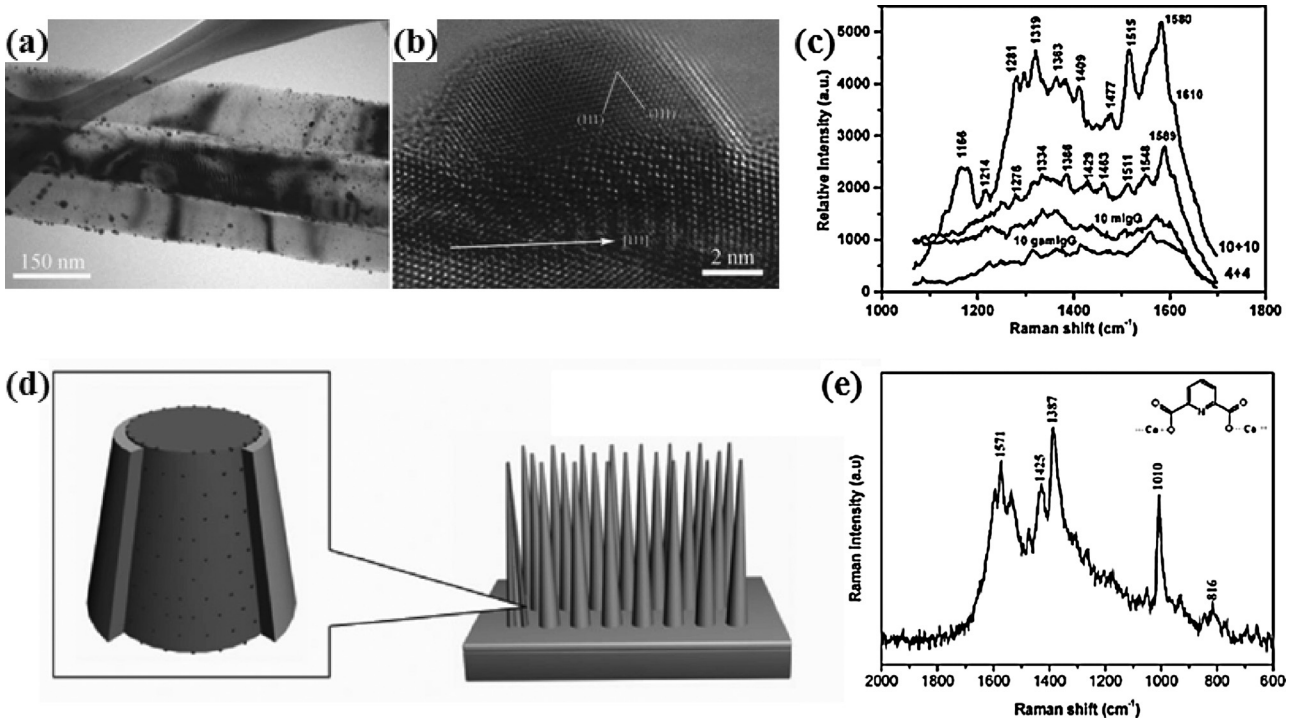

Fig. 27 (a) TEM and (b) HRTEM images showing Ag nanoparticles coated SiNW. SERS spectra of mIgG, gamIgG (denoted as 10 mIgG and 10 gamIgG) and their immunocomplex (denoted as 10 + 10 for 10 ng and 4 + 4 for 4 ng each of mIgG and gamIgG, respectively). Reproduced with permission from [204]. Copyright 2008, American Institute of Physics. (d) Schematic illustrating Ag-coated SiNWs with its enlarged image. (e) SERS spectrum of 3×10^{-5} M CaDPA obtained from optimized SERS substrate. Inset is molecular structure of CaDPA. Reproduced with permission from [205]. Copyright 2008, Wiley-VCH Verlag GmbH & Co. KGaA, Weinheim.

article. A mass transfer model has been confirmed by experiments. The etching directions of Si wafer are found to correlate with various factors including the composition of etchant, the morphological feature of metal catalyst, temperature, gas evolution, stirring condition, and so on. The transfer of excess holes or the dissolution and re-deposition of metal catalyst play important role in the porosification. Various approaches have been developed to fabricate porous SiNWs from heavily or lightly doped Si wafers. The etching behavior of amorphous Si is similar to that of crystalline Si. Dopants or impurities in amorphous Si affect the etching rate of amorphous Si. Motion feature of individual metal catalyst has been investigated using isolated metal catalyst with different morphology. Various new metal, oxidant and F source can be used in MACE. Besides straight nanowires or nanopores, various new morphologies fabricated by MACE have been demonstrated. Facile approaches have been developed to fabricate ordered SiNWs from MACE in chemical hood, without demand of expensive lithography instruments.

Abundant articles in this field help us to understand etching mechanism and etching feature. On the other hand, the conflicting preferential etching directions in different reports is yet to be explained, and the exploration of real mechanism determining etching direction remains necessary. The further control over etching direction in MACE remains challenge, though the influence of various factors on etching direction has been demonstrated. In addition, various processes participate in MACE, for example, gas evolution, heat release, and mass transfer. The detailed influence of these processes on MACE and the correlation between these processes and the final morphology of Si nanostructures are valuable to explore. The motion of isolated catalyst in MACE has been demonstrated, and the further exploration of motion behavior would be helpful to fabricate complicated 3D Si structures.

From the practical point of view, however, some drawbacks of MACE are yet to be overcome for robust control over the morphology of the resulting Si nanostructures. In two-step MACE process, for example, the morphology and size of the etched Si nanostructures are unpredictable and uncontrollable due to the random nature of catalyst metal deposition process occurring on the surface of Si wafer. On the other hand, in MACE of Si utilizing metal meshes as etching catalyst, the metal mesh film can easily be deformed due to its flexible nature, which may hinder the fabrication of Si nanostructures with high uniformity over a considerably large lateral dimension.

Recent advance on solar and thermal energy conversion, Li-ion battery anode, supercapacitor, and sensors based on SiNWs prepared by MACE of silicon is reviewed. Many researchers are quite affirmative for the use of SiNWs in such fields because the performances of SiNWs-based devices have been and are still being improved through the new findings. Recent reports have shown that precisely controlled dimension, morphology and orientation of Si nanostructures fabricated by MACE of Si can considerably improve device performance. Particularly, feasibility of controlled porosity of SiNWs is distinct benefit of MACE in terms of thermoelectric and light emitting devices, energy storage and sensor

applications. Besides such advantages, simple synthesizing procedure of MACE provides lower fabrication cost compared to conventional growth methods such as CVD. It is very likely that evolving experimental techniques for engineering crystal orientation and morphology of Si nanostructures by MACE will further expand the application field.

Acknowledgments

This research was supported by the ''Future-based technology Development Program (Nano Fields)'' through the National Research Foundation of Korea (NRF) funded by the Ministry of Science, ICT and Future Planning (Grant No. 2010-0029332), KRISS project ''Anodization Research Laboratory (KRISS-2013-13011082)'', and the Ministry of Science and Technology of China for the International Science Linkage Program (2011DFG52970), the Ministry of Education of China (IRT1064), and Jiangsu Innovation Research Team.

References

[1] K.Q. Peng, Y.J. Yan, S.P. Gao, J. Zhu, Adv. Mater. 14 (2002) 1164—1167.
[2] K.Q. Peng, Y.J. Yan, S.P. Gao, J. Zhu, Adv. Funct. Mater. 13 (2003) 127—132.
[3] K.Q. Peng, Z.P. Huang, J. Zhu, Adv. Mater. 16 (2004) 73—76.
[4] K.Q. Peng, Y. Wu, H. Fang, X.Y. Zhong, Y. Xu, J. Zhu, Angew. Chem. Int. Ed. 44 (2005) 2737—2742.
[5] K.Q. Peng, H. Fang, J.J. Hu, Y. Wu, J. Zhu, Y.J. Yan, S. Lee, Chem. Eur. J. 12 (2006) 7942—7947.
[6] K.Q. Peng, J.J. Hu, Y.J. Yan, Y. Wu, H. Fang, Y. Xu, S.T. Lee, J. Zhu, Adv. Funct. Mater. 16 (2006) 387—394.
[7] Z.P. Huang, N. Geyer, P. Werner, J. de Boor, U. Gösele, Adv. Mater. 23 (2011) 285—308.
[8] N. Geyer, B. Fuhrmann, Z. Huang, J. de Boor, H.S. Leipner, P. Werner, J. Phys. Chem. C 116 (2012) 13446—13451.
[9] G. Liu, K.L. Young, X. Liao, M.L. Personick, C.A. Mirkin, J. Am. Chem. Soc. 135 (2013) 12196—12199.
[10] L.Y. Li, Y. Liu, X.Y. Zhao, Z.Y. Lin, C.P. Wong, ACS Appl. Mater. Interfaces 6 (2014) 575—584.
[11] W. Chern, K. Hsu, I.S. Chun, B.P. de Azeredo, N. Ahmed, K.H. Kim, J.-m. Zuo, N. Fang, P. Ferreira, X. Li, Nano Lett. 10 (2010) 1582—1588.
[12] J. Kim, Y.H. Kim, S.-H. Choi, W. Lee, ACS Nano 5 (2011) 5242—5248.
[13] Z.P. Huang, T. Shimizu, S. Senz, Z. Zhang, X.X. Zhang, W. Lee, N. Geyer, U. Gösele, Nano Lett 9 (2009) 2519—2525.
[14] Z.P. Huang, T. Shimizu, S. Senz, Z. Zhang, N. Geyer, U. Gösele, J. Phys. Chem. C 114 (2010) 10683—10690.
[15] F. Bai, W.-K. To, Z. Huang, J. Phys. Chem. C 117 (2013) 2203—2209.
[16] H. Chen, H. Wang, X.-H. Zhang, C.-S. Lee, S.-T. Lee, Nano Lett. 10 (2010) 864—868.
[17] H. Morinaga, M. Suyama, T. Ohmi, J. Electrochem. Soc. 141 (1994) 2834—2841.
[18] Y. Kim, A. Tsao, D.H. Lee, R. Maboudian, J. Mater. Chem. C 1 (2013) 220—224.
[19] S.-W. Chang, V.P. Chuang, S.T. Boles, C.V. Thompson, Adv. Funct. Mater. 20 (2010) 4364—4370.
[20] R.G. Milazzo, G.D. Arrigo, C. Spinella, M.G. Grimaldi, E. Rimini, J. Electrochem. Soc. 159 (2012) D521—D525.
[21] M.L. Zhang, K.Q. Peng, X. Fan, J.S. Jie, R.Q. Zhang, S.T. Lee, N.B. Wong, J. Phys. Chem. C 112 (2008) 4444—4450.
[22] O.J. Hildreth, W. Lin, C.P. Wong, ACS Nano 3 (2009) 4033—4042.
[23] R. Gottesman, A. Tangy, I. Oussadon, D. Zitoun, N. J. Chem. 36 (2012) 2456—2459.
[24] K. Rykaczewski, O.J. Hildreth, C.P. Wong, A.G. Fedorov, J.H.J. Scott, Nano Lett. 11 (2011) 2369—2374.
[25] O.J. Hildreth, A.G. Fedorov, C.P. Wong, ACS Nano 6 (2012) 10004—10012.
[26] O.J. Hildreth, K. Rykaczewski, A.G. Fedorov, C.P. Wong, Nanoscale 5 (2013) 961—970.
[27] K.Q. Peng, A.J. Lu, R.Q. Zhang, S.T. Lee, Adv. Funct. Mater. 18 (2008) 3026—3035.
[28] V.A. Sivakov, G. Brönstrup, B. Pecz, A. Berger, G.Z. Radnoczi, M. Krause, S.H. Christiansen, J. Phys. Chem. C 114 (2010) 3798—3803.
[29] Y. Oh, C. Choi, D. Hong, S.D. Kong, S. Jin, Nano Lett. 12 (2012) 2045—2050.
[30] X. Li, P.W. Bohn, Appl. Phys. Lett. 77 (2000) 2572—2574.
[31] A.I. Hochbaum, D. Gargas, Y.J. Hwang, P. Yang, Nano Lett. 9 (2009) 3550—3554.
[32] Y. Qu, L. Liao, Y. Li, H. Zhang, Y. Huang, X. Duan, Nano Lett. 9 (2009) 4539—4543.
[33] W.-K. To, C.-H. Tsang, H.-H. Li, Z. Huang, Nano Lett. 11 (2011) 5252—5258.
[34] F. Bai, M. Li, D. Song, H. Yu, B. Jiang, Y. Li, J. Solid State Chem. 196 (2012) 596—600.
[35] C.-Y. Chen, C.-P. Wong, Chem. Commun. 49 (2013) 7295—7297.
[36] N. Geyer, B. Fuhrmann, H.S. Leipner, P. Werner, ACS Appl. Mater. Interfaces 5 (2013) 4302—4308.
[37] X. Zhong, Y. Qu, Y.-C. Lin, L. Liao, D. Xiangfeng, ACS Appl. Mater. Interfaces 3 (2011) 261—270.
[38] C. Chiappini, X. Liu, J.R. Fakhoury, M. Ferrari, Adv. Funct. Mater. 20 (2010) 2231—2239.
[39] B. Mikhael, B. Elise, M. Xavier, S. Sebastian, M. Johann, P. Laetitia, ACS Appl. Mater. Interfaces 3 (2011) 3866—3873.
[40] D. Wang, S. Schönherr, S. Du, C. Ronning, P. Schaaf, Mater. Lett. 98 (2013) 186—189.
[41] D. Wang, R. Ji, S. Du, A. Albrecht, P. Schaaf, Nanoscale Res. Lett. 8 (2013) 42.
[42] R. Douani, G. Piret, T. Hadjersi, J.-N. Chazalviel, I. Solomon, Thin Solid Films 519 (2011) 5383—5387.
[43] O.J. Hildreth, C. Alvarez, C.P. Wong, Electronic Components and Technology Conference, 2010.
[44] Z. Yue, H. Shen, Y. Jiang, W. Wang, J. Jin, Appl. Phys. A: Mater. 114 (2013) 813—817.
[45] O.J. Hildreth, K. Rykaczewski, C.P. Wong, J. Vac. Sci. Technol. B 30 (2012) 040603.
[46] L. Cui, W.W. Xia, F. Wang, L.J. Yang, Y.J. Hu, Physica B 409 (2013) 47—50.
[47] Y. Kato, S. Adachi, J. Electrochem. Soc. 158 (2011) K157—K163.
[48] Y. Kato, S. Adachi, Appl. Surf. Sci. 258 (2012) 5689—5697.
[49] H.-J. Choi, S. Baek, H.S. Jang, S.B. Kim, B.-Y. Oh, J.H. Kim, Curr. Appl. Phys. 11 (2011) s25—s29.
[50] N. Brahiti, S.-A. Bouanik, T. Hadjersi, Appl. Surf. Sci. 258 (2012) 5628—5637.
[51] S. Naama, T. Hadjersi, G. Nezzal, L. Guerbous, J. Nano Res. 21 (2013) 109—115.
[52] N.T.P. Nguyen, Y. Coffinier, V. Thomy, R. Boukherroub, Phys. Status Solidi A 210 (2013) 2178—2182.
[53] W. Wang, L. Zhao, P. Song, Y. Zhang, Appl. Mech. Mater. 217—219 (2012) 1141—1145.
[54] D.H. Lee, Y. Kim, G.S. Doerk, I. Laboriante, R. Maboudian, J. Mater. Chem. 21 (2011) 10359—10363.
[55] P. Lianto, S. Yu, J. Wu, C.V. Thompson, W.K. Choi, Nanoscale 4 (2012) 7532—7539.

[56] B.P. Azeredo, J. Sadhu, J. Ma, K. Jacobs, J. Kim, K. Lee, J.H. Eraker, X. Li, S. Sinha, N. Fang, P. Ferreira, K. Hsu, Nanotechnology 24 (2013) 225305.
[57] Z.P. Huang, N. Geyer, L.F. Liu, M.Y. Li, P. Zhong, Nanotechnology 21 (2010) 465301.
[58] J. Kim, H. Rhu, W. Lee, J. Mater. Chem. 21 (2011) 15889.
[59] J.M. Weisse, C.H. Lee, D.R. Kim, L. Cai, P.M. Rao, X. Zheng, Nano Lett. 13 (2013) 4362—4368.
[60] K. Rykaczewski, O.J. Hildreth, C.P. Wong, A.G. Fedorov, J.J.H. Scott, Adv. Mater. 23 (2011) 659—663.
[61] O.J. Hildreth, D. Brown, C.P. Wong, Adv. Funct. Mater. 21 (2011) 3119—3128.
[62] T. Nakamura, N. Hosoya, B.P. Tiwari, S. Adachi, J. Appl. Phys. 108 (2010) 104315.
[63] C.-C. Lin, Y.-C. Yen, H.-C. Wu, N.-L. Wu, J. Chin. Chem. Soc. — TAIP 59 (2012) 1226—1232.
[64] T. Nakamura, B.P. Tiwari, S. Adachi, Jpn. J. Appl. Phys. 50 (2011) 081301.
[65] A. Loni, D. Barwick, L. Batchelor, J. Tunbridge, Y. Han, Z.Y. Li, L.T. Canham, Electrochem. Solid ST 14 (2011) k25—k27.
[66] B.M. Bang, J.-I. Lee, H. Kim, J. Cho, S. Park, Adv. Energy Mater. 2 (2012) 878—883.
[67] J.-I. Lee, S. Park, Nano Energy 2 (2013) 146—152.
[68] Y. Liu, B. Chen, F. Cao, H.L.W. Chan, X. Zhao, J. Yuan, J. Mater. Chem. 21 (2011) 17083.
[69] Z.P. Huang, R.X. Wang, D. Jia, M.Y. Li, M.G. Humphrey, C. Zhang, ACS Appl. Mater. Interfaces 4 (2012) 1553—1559.
[70] S.-C. Shiu, S.-C. Hung, J.-J. Chao, C.-F. Lin, Appl. Surf. Sci. 255 (2009) 8566—8570.
[71] A. Vlad, A.L.M. Reddy, A. Ajayan, N. Singh, J.F. Cohy, S. Melinte, P.M. Ajayan, Proc. Natl. Acad. Sci. U. S. A. 109 (2012) 15168—15176.
[72] S.-C. Shiu, H.-J. Syu, S.-C. Hung, C.-F. Lin, Proceedings of IEEE Conference on Nanotechnology, 2010, pp. 474—477.
[73] T.-C. Lin, S.-C. Shiu, K.-L. Pun, H.-J. Syu, C.-F. Lin, Proceedings of IEEE Photovoltaic Specialists Conference (2011) 000346—000349.
[74] S.-C. Shiu, T.-C. Lin, K.-L. Pun, H.-J. Syu, S.-C. Hung, J.-J. Chao, C.-F. Lin, Proceedings of IEEE Conference on Nanotechnology, 2011, pp. 1703—1706.
[75] S.-C. Shiu, T.-C. Lin, K.-L. Pun, H.-J. Syu, S.-C. Hung, C.-F. Lin, Proc. SPIE 8102 (2011) 810217.
[76] J.M. Weisse, D.R. Kim, C.H. Lee, X. Zheng, Nano Lett. 11 (2011) 1300—1305.
[77] J.M. Weisse, C.H. Lee, D.R. Kim, X. Zheng, Nano Lett. 12 (2012) 3339—3343.
[78] J.-Y. Jung, Z. Guo, S.-W. Jee, H.-D. UM, K.-T. Park, J.-H. Lee, 10th IEEE International Conference, 2010.
[79] J.-Y. Jung, Z. Guo, S.-W. Jee, H.-D. Um, K.-T. Park, J.-H. Lee, Opt. Express. 18 (2010) A286—A292.
[80] F. Bai, M. Li, R. Huang, D. Song, B. Jiang, Y. Li, Nanoscale Res. Lett. 7 (2012) 557.
[81] C.-Y. Chen, W.-J. Li, H.-H. Chen, ChemPhysChem 13 (2012) 1415—1420.
[82] H. Lin, H.-Y. Cheung, F. Xiu, F. Wang, S. Yip, N. Han, T. Hung, J. Zhou, J.C. Ho, C.-Y. Wong, J. Mater. Chem. A 1 (2013) 9942—9946.
[83] X. Geng, M. Li, L. Zao, P.W. Bohn, J. Electron. Mater. 40 (2011) 2480—2485.
[84] X. Geng, Z. Qi, M. Li, B.K. Duan, L. Zhao, P.W. Bohn, Sol. Energy Mater. Sol. Cells 103 (2012) 98—107.
[85] B. Jiang, M. Li, F. Bai, H. Yu, T. Mwenya, AIP Adv. 3 (2013) 032119.
[86] R. Li, S. Chuwongin, S. Wang, W.d. Zhou, Proceedings of IEEE Photovoltaic Specialists Conference, 2011, pp. 002563—002565.
[87] B. Dou, R. Jia, H. Li, C. Chen, Y. Meng, J. Vac. Sci. Technol. B 30 (2012) 041401.
[88] R. Liu, F. Zhang, C. Con, B. Cui, B. Sun, Nanoscale Res. Lett. 8 (2013) 155.
[89] C.I. Yeo, J.B. Kim, Y.M. Song, Y.T. Lee, Nanoscale Res. Lett. 8 (2013) 159.
[90] Z.P. Huang, T. Shimizu, S. Senz, Z. Zhang, X.X. Zhang, W. Lee, N. Geyer, U. Gösele, Nano Lett. 9 (2009) 2519—2525.
[91] J. Kim, H. Han, Y.H. Kim, S.-H. Choi, J.-C. Kim, W. Lee, ACS Nano 5 (2011) 3222—3229.
[92] K. Liu, S. Qu, F. Tan, Y. Bi, S. Lu, Z. Wang, Mater. Lett. 101 (2013) 96—98.
[93] S.-J. Park, H. Han, H. Rhu, S. Baik, W. Lee, J. Mater. Chem. C 1 (2013) 5330—5335.
[94] C. Pacholski, Phys. Status Solidi C 8 (2011) 1797—1800.
[95] L. Wu, W. He, D. Teng, S. Ji, C. Ye, Langmuir 28 (2012) 7476—7483.
[96] L.T. Canham, Appl. Phys. Lett. 57 (1990) 1046—1048.
[97] N. Megouda, R. Douani, T. Hadjersi, R. Boukherroub, J. Lumine 129 (2009) 1750—1753.
[98] V.A. Sivakov, F. Voigt, A. Berger, G. Bauer, S.H. Christiansen, Phys. Rev. B 82 (2010) 125446.
[99] L. Lin, S. Guo, X. Sun, J. Feng, Y. Wang, Nanoscale Res. Lett. 5 (2010) 1822—1828.
[100] M.K. Dawood, S. Tripathy, S.B. Dolmanan, T.H. Ng, H. Tan, J. Lam, J. Appl. Phys. 112 (2012) 073509.
[101] H. He, C. Liu, L. Sun, Z. Ye, Appl. Phys. Lett. 99 (2011) 123106.
[102] L.H. Lin, X.Z. Sun, R. Tao, Z.C. Li, J.Y. Feng, Z.J. Zhang, J. Appl. Phys. 110 (2011) 073109.
[103] X. Sun, R. Tao, L. Lin, Z. Li, Z. Zhang, J. Feng, Appl. Surf. Sci. 257 (2011) 3861—3866.
[104] L. Lin, X. Sun, R. Tao, J. Feng, Z. Zhang, Nanotechnology 22 (2011) 075203.
[105] E.F. Pecora, N. Lawrence, P. Gregg, J. Trevino, P. Artoni, A. Irrera, F. Priolo, L.D. Negro, Nanoscale 4 (2012) 6 2863—2866.
[106] C. Zhang, C. Li, Z. Liu, J. Zheng, C. Xue, Y. Zuo, B. Cheng, Q. Wang, Nanoscale Res. Lett. 8 (2013) 277.
[107] K.-Q. Peng, X. Wang, L. Li, Y. Hu, S.-T. Lee, Nano Today 8 (2013) 75—97.
[108] A.I. Hochbaum, P. Yang, Chem. Rev. 110 (2010) 527—546.
[109] K.-Q. Peng, S.-T. Lee, Adv. Mater. 23 (2011) 198—215.
[110] L. Hu, G. Chen, Nano Lett. 7 (2007) 3249—3252.
[111] E. Garnett, P. Yang, Nano Lett. 10 (2010) 1082—1087.
[112] J. Li, H. Yu, Y. Li, Nanoscale 3 (2011) 4888—4900.
[113] E.C. Garnett, M.L. Brongersma, Y. Cui, M.D. McGehee, Annu. Rev. Mater. Res. 41 (2011) 269—295.
[114] M. Yu, Y.-Z. Long, B. Sun, Z. Fan, Nanoscale 4 (2012) 2783—2796.
[115] G. Yuan, K. Aruda, S. Zhou, A. Levine, J. Xie, D. Wang, Angew. Chem. Int. Ed. 50 (2011) 2334—2338.
[116] K. Peng, Y. Xu, Y. Wu, Y.J. Yan, S.T. Lee, J. Zhu, Small 1 (2005) 1062—1067.
[117] E.C. Garnett, P. Yang, J. Am. Chem. Soc. 130 (2008) 9224—9225.
[118] H. Fang, X. Li, S. Song, Y. Xu, J. Zhu, Nanotechnology 19 (2008) 255703.
[119] X.X. Lin, X. Hua, Z.G. Huang, W.Z. Shen, Nanotechnology 24 (2013) 235402.
[120] E.S.M. Ashour, M.Y. Sulaiman, N. Amin, Z. Ibrahim, J. Phys.: Conf. Ser. 431 (2013) 012021.
[121] X. Wang, K.L. Pey, C.H. Yip, E.A. Fitzgerald, D.A. Antoniadis, J. Appl. Phys. 108 (2010) 124303.
[122] J.-Y. Jung, Z. Guo, S.-W. Jee, H.-D. Um, K.-T. Park, M.S. Hyun, J.M. Yang, J.-H. Lee, Nanotechnology 21 (2010) 445303.
[123] C. Chen, R. Jia, H. Yue, H. Li, X. Liu, D. Wu, W. Ding, T. Ye, S. Kasai, H. Tamotsu, J. Chu, S. Wang, J. Appl. Phys. 108 (2010) 094318.
[124] H.-D. Um, J.-Y. Jung, H.-S. Seo, K.-T. Park, S.-W. Jee, S.A. Moiz, J.-H. Lee, Jpn. J. Appl. Phys. 49 (2010) 04DN02.

[125] V. Sivakov, G. Andra, A. Gawlik, A. Berger, J. Plentz, F. Falk, S.H. Christiansen, Nano Lett. 9 (2009) 1549—1554.
[126] B.-R. Huang, Y.-K. Yang, T.-C. Lin, W.-L. Yang, Sol. Energy Mater. Sol. Cells 98 (2012) 357—362.
[127] G. Fan, H. Zhu, K. Wang, J. Wei, X. Li, Q. Shu, N. Guo, D. Wu, ACS Appl. Mater. Interfaces 3 (2011) 721—725.
[128] C. Xie, P. Lv, B. Nie, J. Jie, X. Zhang, Z. Wang, P. Jiang, Z. Hu, L. Luo, Z. Zhu, L. Wang, C. Wu, Appl. Phys. Lett. 99 (2011) 133113.
[129] X. Zhang, C. Xie, J. Jie, X. Zhang, Y. Wu, W. Zhang, J. Mater. Chem. A 1 (2013) 6593—6601.
[130] K. Peng, X. Wang, S.-T. Lee, Appl. Phys. Lett. 92 (2008) 163103.
[131] K.-Q. Peng, X. Wang, X.-L. Wu, S.-T. Lee, Nano Lett. 9 (2009) 3704—3709.
[132] X. Shen, B. Sun, F. Yan, J. Zhao, F. Zhang, S. Wang, X. Zhu, S. Lee, ACS Nano 4 (2010) 5869—5876.
[133] X. Wang, K.-Q. Peng, X.-J. Pan, X. Chen, Y. Yang, L. Li, X.-M. Meng, W.-J. Zhang, S.-T. Lee, Angew. Chem. Int. Ed. 50 (2011) 9861—9865.
[134] E.A. Dalchiele, F. Martín, D. Leinen, R.E. Marotti, J.R. Ramos-Barrado, Thin Solid Films 518 (2010) 1804—1808.
[135] Y. Cheng, G. Fang, C. Li, L. Yuan, L. Ai, B. Chen, X. Zhao, Z. Chen, W. Bai, C. Zhan, J. Appl. Phys. 102 (2007) 083516.
[136] X. Shen, B. Sun, D. Liu, S.-T. Lee, J. Am. Chem. Soc. 133 (2011) 19408—19415.
[137] G. Kalita, S. Adhikari, H.R. Aryal, R. Afre, T. Soga, M. Sharon, W. Koichi, M. Umeno, J. Phys. D: Appl. Phys. 42 (2009) 115104.
[138] W. Lu, C. Wang, W. Yue, L. Chen, Nanoscale 3 (2011) 3631—3634.
[139] H.-J. Syu, S.-C. Shiu, C.-F. Lin, Sol. Energy Mater. Sol. Cells 98 (2012) 267—272.
[140] F. Zhang, X. Han, S.-t. Lee, B. Sun, J. Mater. Chem. 22 (2012) 5362—5368.
[141] S.A. Moiz, A.M. Nahhas, H.-D. Um, S.-W. Jee, H.K. Cho, S.-W. Kim, J.-H. Lee, Nanotechnology 23 (2012) 145401.
[142] J.-S. Huang, C.-Y. Hsiao, S.-J. Syu, J.-J. Chao, C.-F. Lin, Sol. Energy Mater. Sol. Cells 93 (2009) 621—624.
[143] R.A. Street, P. Qi, R. Lujan, W.S. Wong, Appl. Phys. Lett. 93 (2008) 163109.
[144] S.-H. Tsai, H.-C. Chang, H.-H. Wang, S.-Y. Chen, C.-A. Lin, S.-A. Chen, Y.-L. Chueh, J.-H. He, ACS Nano 5 (2011) 9501—9510.
[145] M.M. Adachi, M.P. Anantram, K.S. Karim, Sci. Rep. 3 (2012) 1546.
[146] W.W. He, K.J. Wu, K. Wang, T.F. Shi, L. Wu, S.X. Li, D.Y. Teng, C.H. Ye, Sci. Rep. 4 (2013) 3715.
[147] M. Jørgensen, K. Norrman, S.A. Gevorgyan, T. Tromholt, B. Andreasen, F.C. Krebs, Adv. Mater. 24 (2012) 580—612.
[148] S.-C. Shiu, J.-J. Chao, S.-C. Hung, C.-L. Yeh, C.-F. Lin, Chem. Mater. 22 (2010) 3108—3113.
[149] P. Yu, C.-Y. Tsai, J.-K. Chang, C.-C. Lai, P.-H. Chen, Y.-C. Lai, P.-T. Tsai, M.-C. Li, H.-T. Pan, Y.-Y. Huang, C.-I. Wu, Y.-L. Chueh, S.-W. Chen, C.-H. Du, S.-F. Horng, H.-F. Meng, ACS Nano 7 (2013) 10780—10787.
[150] T. Song, F. Zhang, X. Lei, Y. Xu, S. Lee, B. Sun, Nanoscale 4 (2012) 1336—1343.
[151] J.-Y. Jung, K. Zhou, J.H. Bang, J.-H. Lee, J. Phys. Chem. C 116 (2012) 12409—12414.
[152] F.J. DiSalvo, Science 285 (1999) 703—706.
[153] L.E. Bell, Science 321 (2008) 1457—1461.
[154] M.S. Dresselhaus, G. Chen, M.Y. Tang, R. Yang, H. Lee, D. Wang, Z. Ren, J.-P. Fleurial, P. Gogna, Adv. Mater. 19 (2007) 1043—1053.
[155] D.G. Cahill, W.K. Ford, K.E. Goodson, G.D. Mahan, A. Majumdar, H.J. Maris, R. Merlin, S.R. Phillpot, J. Appl. Phys. 93 (2003) 793—818.
[156] J.R. Sootsman, D.Y. Chung, M.G. Kanatzidis, Angew. Chem. Int. Ed. 48 (2009) 8616—8639.
[157] K. Nielsch, J. Bachmann, J. Kimling, H. Böttner, Adv. Energy Mater. 1 (2011) 713—731.
[158] W. Kim, Mater. Res. Innov. 15 (2011) 375—385.
[159] L.D. Hicks, M.S. Dresselhaus, Phys. Rev. B 47 (1993) 16631.
[160] A.I. Hochbaum, R. Chen, R.D. Delgado, W. Liang, E.C. Garnett, M. Najarian, A. Majumdar, P. Yang, Nature 451 (2008) 163—167.
[161] C.-Y. Chen, D.H. Phan, C.-C. Wong, T.-J. Yen, J. Electrochem. Soc. 158 (2011) D302—D306.
[162] J. Lim, K. Hippalgaonkar, S.C. Andrews, A. Majumdar, P. Yang, Nano Lett. 12 (2012) 2475—2482.
[163] G. Yuan, R. Mitdank, A. Mogilatenko, S.F. Fischer, J. Phys. Chem. C 116 (2012) 13767—13773.
[164] J.M. Weisse, A.M. Marconnet, D.R. Kim, P.M. Rao, M.A. Panzer, K.E. Goodson, X. Zheng, Nanoscale Res. Lett. 7 (2012) 554.
[165] C. Li, E. Krali, K. Fobelets, B. Cheng, Q. Wang, Appl. Phys. Lett. 101 (2012) 222101.
[166] J.P. Feser, J.S. Sadhu, B.P. Azeredo, K.H. Hsu, J. Ma, J. Kim, M. Seong, N.X. Fang, X. Li, P.M. Ferreira, S. Sinha, D.G. Cahill, J. Appl. Phys. 112 (2012) 114306.
[167] M.G. Ghossoub, K.V. Valavala, M. Seong, B. Azeredo, K. Hsu, J.S. Sadhu, P.K. Singh, S. Sinha, Nano Lett. 13 (2013) 1564—1571.
[168] E. Krali, Z.A.K. Durrani, Appl. Phys. Lett. 102 (2013) 143102.
[169] H. Wu, Y. Cui, Nano Today 7 (2012) 414—429.
[170] A.S. Aricò, P. Bruce, B. Scrosati, J.-M. Tarascon, W.v. Schalkwijk, Nat. Mater. 4 (2005) 366—377.
[171] P.G. Bruce, B. Scrosati, J.-M. Tarascon, Angew. Chem. Int. Ed. 47 (2008) 2930—2946.
[172] J.R. Szczech, S. Jin, Energy Environ. Sci. 4 (2011) 56—72.
[173] B.A. Boukamp, G.C. Lesh, R.A. Huggins, J. Electrochem. Soc. 128 (1981) 725—729.
[174] H. Jung, M. Park, Y.-G. Yoon, G.-B. Kim, S.-K. Joo, J. Power Sources 115 (2003) 346—351.
[175] S. Ohara, J. Suzuki, K. Sekine, T. Takamura, J. Power Sources 136 (2004) 303—306.
[176] S.-C. Lai, J. Electrochem. Soc. 123 (1976) 1196—1197.
[177] C.K. Chan, H.P.G. Liu, K. McIlwrath, X.F. Zhang, R.A. Huggins, Y. Cui, Nat. Nanotechnol. 3 (2008) 31—35.
[178] L. Hu, H. Wu, S.S. Hong, L. Cui, J.R. McDonough, S. Bohy, Y. Cui, Chem. Commun. 47 (2010) 367—369.
[179] A. Magasinski, P. Dixon, B. Hertzberg, A. Kvit, J. Ayala, G. Yushin, Nat. Mater. 9 (2010) 353—358.
[180] S.-H. Ng, J. Wang, D. Wexler, K. Konstantinov, Z.-P. Guo, H.-K. Liu, Angew. Chem. Int. Ed. 45 (2006) 6896—6899.
[181] K. Peng, J. Jie, W. Zhang, S.-T. Lee, Appl. Phys. Lett. 93 (2008) 033105.
[182] R. Huang, X. Fan, W. Shen, J. Zhu, Appl. Phys. Lett. 95 (2009) 133119.
[183] W. Xu, J.C. Flake, J. Electrochem. Soc. 157 (2010) A41—A45.
[184] R. Huang, J. Zhu, Mater. Chem. Phys. 121 (2010) 519—522.
[185] M.C. Qiu, L.W. Yang, X. Qi, J. Li, J.X. Zhong, ACS Appl. Mater. Interfaces 2 (2010) 3614—3618.
[186] X.-L. Wang, W.-Q. Han, ACS Appl. Mater. Interfaces 2 (2010) 3709—3713.
[187] W. Xu, S.S.S. Vegunta, J.C. Flake, J. Power Sources 196 (2011) 8583—8589.
[188] S.H. Nguyen, J.C. Lim, J.K. Lee, Electrochim. Acta 74 (2012) 53—58.
[189] M. Ge, J. Rong, X. Fang, C. Zhou, Nano Lett. 12 (2012) 2318—2323.
[190] B. Tao, J. Zhang, F. Miao, S. Hui, L. Wan, Electrochim. Acta 55 (2010) 5258—5262.
[191] F. Lu, M. Qiu, X. Qi, L. Yang, J. Yin, G. Hao, X. Feng, J. Li, J. Zhong, Appl. Phys. A: Mater. 104 (2011) 545—550.
[192] S.-W. Chang, J. Oh, S.T. Boles, C.V. Thompson, Appl. Phys. Lett. 96 (2010) 153108.

[193] G. Boschloo, A. Hagfeldt, J. Phys. Chem. B 105 (2001) 3039—3044.
[194] U.M. Patil, R.R. Salunkhe, K.V. Gurav, C.D. Lokhande, Appl. Surf. Sci. 255 (2008) 2603—2607.
[195] X.-J. Huang, Y.-K. Choi, Sensor Actuat. B: Chem. 122 (2007) 659—671.
[196] A.K. Wanekaya, W. Chen, N.V. Myung, A. Mulchandani, Electroanalysis 18 (2006) 533—550.
[197] K.-Q. Peng, X. Wang, S.-T. Lee, Appl. Phys. Lett. 95 (2009) 243112.
[198] J. Yin, X. Qi, L. Yang, G. Hao, J. Li, J. Zhong, Electrochim. Acta 56 (2011) 3884—3889.
[199] H.J. In, C.R. Field, P.E. Pehrsson, Nanotechnology 22 (2011) 355501.
[200] H. Han, J. Kim, H.S. Shin, J.Y. Song, W. Lee, Adv. Mater. 24 (2012) 2284—2288.
[201] J.-S. Noh, H. Kim, B.S. Kim, E. Lee, H.H. Cho, W. Lee, J. Mater. Chem. 21 (2011) 15935—15939.
[202] T. Qiu, X.L. Wu, J.C. Shen, P.C.T. Ha, P.K. Chu, Nanotechnology 17 (2006) 5769—5772.
[203] X. Sun, L. Lin, Z. Li, Z. Zhang, J. Feng, Appl. Surf. Sci. 256 (2009) 916—920.
[204] M.-L. Zhang, C.-Q. Yi, X. Fan, K.-Q. Peng, N.-B. Wong, M.-S. Yang, R.-Q. Zhang, S.-T. Lee, Appl. Phys. Lett. 92 (2008) 043116.
[205] B. Zhang, H. Wang, L. Lu, K. Ai, G. Zhang, X. Cheng, Adv. Funct. Mater. 18 (2008) 2348—2355.
[206] X.T. Wang, W.S. Shi, G.W. She, L.X. Mu, S.T. Lee, Appl. Phys. Lett. 96 (2010) 053104.
[207] C. Yi, C.-W. Li, H. Fu, M. Zhang, S. Qi, N.-B. Wong, S.-T. Lee, M. Yang, Anal. Bioanal. Chem. 397 (2010) 3143—3150.
[208] S. Hui, J. Zhang, X. Chen, H. Xu, D. Ma, Y. Liu, B. Tao, Sens. Actuator B: Chem. 155 (2011) 592—597.
[209] Y. Cui, Q. Wei, H. Park, C.M. Lieber, Science 293 (2001) 1289—1292.
[210] I. Park, Z. Li, A.P. Pisano, R. StanleyWilliams, Nanotechnology 21 (2010) 015501.
[211] A.A. Talin, L.L. Hunter, F. Léonard, B. Rokad, Appl. Phys. Lett. 89 (2006) 153102.
[212] M.C. McAlpine, H. Ahmad, D. Wang, J.R. Heath, Nat. Mater. 6 (2007) 379—384.
[213] S. Nie, S.R. Emory, Science 275 (1997) 1102—1106.
[214] J.-A. Huang, Y.-Q. Zhao, X.-J. Zhang, L.-F. He, T.-L. Wong, Y.-S. Chui, W.-J. Zhang, S.-T. Lee, Nano Lett. 13 (2013) 5039—5045.

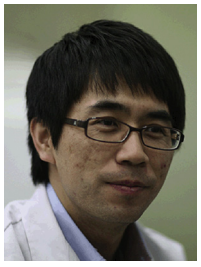

Hee Han is a post-doctoral researcher at Korea Research Institute of Standards and Science (KRISS). He did his graduate work in Materials Science & Engineering at the Pohang University of Science and Technology (POSTECH), where he received M.S. and Ph.D. degrees in 2006 and 2010, respectively. His current research interests focus on the structure—property relations of arrays of ferroelectric nanocapacitors fabricated by ultra-thin porous AAO as deposition mask and also on energy-harvesting applications of silicon nanowires formed by metal-assisted chemical etching of silicon wafer.

Zhipeng Huang received a B.S. and a Ph.D. in Materials Science and Engineering from Tsinghua University, PR China in 2002 and 2007, respectively. He did postdoctoral research at the Max-Planck-Institut für Mikrostrukturphysik in Halle, Germany from 2007 to 2009. He is currently professor at the Functional Molecular Materials Centre, Scientific Research Academy, Jiangsu University, PR China. His main research interest is the controllable fabrication of Si nanostructures and their applications.

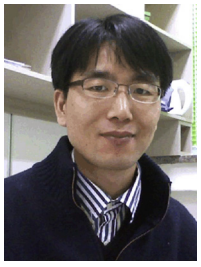

Woo Lee is a principal researcher at Korea Research Institute of Standards and Science (KRISS) and a professor of the Department of Nano Science, University of Science and Technology (UST), Korea. He received his Ph.D. from Seoul National University (2003). He worked with the late Prof. Ulrich Gösele as a postdoctoral research fellow and later a group leader at Max-Planck-Institut für Mikrostrukturphysik in Halle, Germany, until he joined KRISS in 2008. He brought a renewed attention to the academic research on pulsed anodization as well as hard anodization of aluminum by establishing new self-ordering regimes and also by implementing them for the structural engineering of porous AAO. His research interests focus on the anodization of aluminum and template-based synthesis of low-dimensional functional nanostructures for memory and energy harvesting applications.